Copyright Undertaking

This thesis is protected by copyright, with all rights reserved.

By reading and using the thesis, the reader understands and agrees to the following terms:

1. The reader will abide by the rules and legal ordinances governing copyright regarding the use of the thesis.
2. The reader will use the thesis for the purpose of research or private study only and not for distribution or further reproduction or any other purpose.
3. The reader agrees to indemnify and hold the University harmless from and against any loss, damage, cost, liability or expenses arising from copyright infringement or unauthorized usage.

IMPORTANT

If you have reasons to believe that any materials in this thesis are deemed not suitable to be distributed in this form, or a copyright owner having difficulty with the material being included in our database, please contact lbsys@polyu.edu.hk providing details. The Library will look into your claim and consider taking remedial action upon receipt of the written requests.

Pao Yue-kong Library, The Hong Kong Polytechnic University, Hung Hom, Kowloon, Hong Kong

http://www.lib.polyu.edu.hk

CONTROLLABLE GROWTH AND HEAT-TRANSPORTING PROPERTIES OF TWO-DIMENSIONAL MATERIALS

LIN Ziyuan

M.Phil

The Hong Kong Polytechnic University

2017

The Hong Kong Polytechnic University
Department of Applied Physics

Controllable Growth and Heat-transporting Properties of Two-dimensional Materials

LIN Ziyuan

A thesis submitted in partial fulfillment of the requirements for the degree of Master of Philosophy

July 2016

CERTIFICATE OF ORIGINALITY

I hereby declare that this thesis is my own work and that, to the best of my knowledge and belief, it reproduces no material previously published or written, nor material that has been accepted for the award of any other degree or diploma, except where due acknowledgement has been made in the text.

____(Signed)

___________________LIN Ziyuan___________________ (Name of student)

Abstracts

In this study, we first fabricate monolayer MoS_2 by chemical vapor deposition. The morphology evolution from triangular flakes to continuous thin films by changing the distance between source and growth substrates is observed. The effects of the nuclei density on the domain size and surface coverage are then systematically investigated. By optimizing the growth conditions, we successfully grow single-crystalline MoS_2 flake with the size larger than 300 μm. We also develop a transfer process assisted with a Cu thin film, which allows us to transfer MoS_2 onto arbitrary substrates. The characterizations on transferred MoS_2 confirm observable residues and wrinkles are absent on the surface and that the MoS_2 maintains the properties as the as-grown one.

To develop a deeper understanding of MoS_2 growth, we further observe the dynamic growth of MoS_2 in TEM by heating the solid precursor. The evolution process of *in-situ* MoS_2 growth is identified including the initial formation of vertically aligned layers, then a grain rotation towards a horizontally layered structure, precipitation and growth of nanocrystals, and formation of hexagonal MoS_2 nanoflakes by facet development. We also investigate the *in-situ* growth of Mo_xC.

By adjusting the carbon concentration in the precursor, we attain MoC and Mo_2C in different phases and the growth pathways are also different. The developed understanding of MoS_2 and MXene formation using in-situ TEM technique provides fundamental knowledge in synthesis of the emerging 2D materials.

Lastly, taking advantages of thermal conducting and electrical insulating h-BN, we develop the local thermal management for high electron mobility transistors, utilizing few-layer h-BN as heat spreaders and thick counterpart as heat sinks. Few-layer h-BN fully covers the transistors and rapidly dissipates the heat from the hotspot, while thick h-BN stores the intensive heat flux from few-layer h-BN and withdraws to the ambient without affecting the devices. With the developed thermal management, the performance of the transistor is enhanced. The simulations indicates ~40 °C temperature reduction when the transistor is operated at 4 W/mm on sapphire substrates after the application of the thermal management. The developed heat dissipation is highly potentially applicable in thermal management of power devices and integrated circuits because of the characteristics of thermal-conducting and electrical-insulating of h-BN.

List of Publications

Journal

1. **Ziyuan Lin**, Yuda Zhao, Changjian Zhou, Ren Zhong, Xinsheng Wang, Yuen Hong Tsang and Yang Chai, Controllable growth of large-size crystalline MoS_2 and resist-free transfer assisted with a Cu thin film, *Scientific Reports*, **2015**, 5, 18596.

2. **Ziyuan Lin**, Chunru Liu and Yang Chai, High Thermally conductive and electrically insulating 2D boron nitride nanosheet for efficient heat dissipation of high-power transistors, *2D Materials*, **2016**, 3(4), 041009.

3. Huajing Fang, **Ziyuan Lin**, Xinsheng Wang, Chun Yin Tang, Yan Chen, Fan Zhang, Yang Chai, Qiang Li, Qingfeng Yan, H.L.W.Chan and Jiyan Dai, Infrared light gated MoS_2 field effect transistor, *Optics Express*, **2015**, 23(25), 31908.

4. Ling Zhang, Yuda Zhao, **Ziyuan Lin**, Fangyuan Gu, Shu Ping Lau, Li Li and Yang Chai, Kinetically controlled synthesis of large-scale morphology-tailored silver nanostructures at low temperature, *Nanoscale*, **2015**, 7(32), 13420.

5. Changjian Zhou, Xinsheng Wang, Salahuddin Raju, **Ziyuan Lin**, Daniel Villaroman, Baoling Huang, Helen Lai-Wa Chan, Mansun

Chan, and Yang Chai, Low voltage and high ON/OFF ratio field-effect transistors based on CVD MoS_2 and ultrahigh-k gate dielectric PZT, *Nanoscale*, **2015**, 7(19), 8695.

6. Yuda Zhao, Jingsi Qiao, Peng Yu, Zhixin Hu, **Ziyuan Lin**, Shu Ping Lau, Zheng Liu, Wei Ji and Yang Chai, Extraordinarily strong interlayer interaction in 2D layered PtS_2, *Advanced Materials*, **2016**, 28, 2399.

7. Changjian Zhou, Yuda Zhao, Salahuddin Raju, Yi Wang, **Ziyuan Lin**, Mansun Chan, and Yang Chai, Carrier type control of WSe_2 field−effect transistors by thickness modulation and MoO_3 layer doping, *Advanced Functional Materials*, **2016**, 26, 4223.

8. Linfeng Fei, Shuijin Lei, Weibing Zhang, Wei Lu, **Ziyuan Lin**, Yang Chai and Yu Wang, Direct TEM observations on growth mechanisms of two-dimensional MoS_2 flakes, *Nature Communications*, **2016**, 7, 12206.

Conference

1. **Ziyuan Lin**, Xinsheng Wang, Yuda Zhao and Yang Chai, Resist-free and wrinkle-free transfer of two-dimensional layered materials, The IEEE Student Symposium on Electron Devices and

Solid-State Circuits, 5 December 2014, Hong Kong, China.

2. **Ziyuan Lin**, Chunru Liu, and Yang Chai, Improved performance of HEMTs with BN as heat dissipation, The 7th IEEE International Nanoelectronics Conference, 9-11 May 2016, Chengdu. China.

Acknowledgements

Firstly, I would like to express my sincere gratitude to my supervisor, Dr. Yang Chai, for his valuable suggestions and strong support during my M.Phil. study. His profound knowledge and enormous experience in the scientific research inspire me with confidence and guide me through the difficult time. With his unselfish assistance, I smoothly accomplish my M.Phil. study.

I also appreciate the kindly help from my co-supervisor, Dr. Feng Yan and professors from my department, Prof. Philip Wong, Prof. Jiyan Dai, and Dr. Peter Tsang. It is my honor to get advice and help from them, which is of great benefit to my M.Phil. study.

I would further express my appreciation to the technicians, Dr. Wei Lu, Dr. Hardy Lui, Dr. Terence Wong and Dr. Vincent Chan. They provided me detailed guidance in the facility and supported me in my M.Phil. study.

I am very happy and grateful to work with my group members, Dr. Xinsheng Wang, Dr. Changjian Zhou, Dr. Yizhu Xie, Dr. Ling Zhang, Dr. Yao Guo, Dr. Fang Yuan, Dr. Mengye Wang, Dr. Yuda Zhao, Ms. Feichi Zhou, Mr. Kang Xu, Mr. Xinpeng Shen, Mr. Feng Pan, Mr. Yi Wang and Mr, Liting Shen. Their support and advice are

of great help during my research. I am also grateful to work with my colleagues, Dr. Gongxun Bai, Dr. Shenghuang Lin, Mr. Yanyong Li and Mr. Peng You. I would like to express special thanks to Dr. Xinsheng Wang and Mr. Yuda Zhao. They gave their selfless help when I began my research. Mr. Yuda Zhao also continuing sharing his research experience during my two-year study.

Finally, I would like to express my deep love to my parents and my girlfriend, who unconditionally support me. Thanks very much for their companion and encouragement.

Table of Contents

Abstract I

List of Publications III

Acknowledges VI

Table of Contents VIII

List of Figures XI

Chapter 1 Introduction 1

1.1 Background 1

1.2 Molybdenum Disulfide 3

1.2.1 Introduction to MoS_2 3

1.2.2 Vapor deposition of MoS_2 5

1.2.3 Transfer of MoS_2 11

1.3 Hexagonal Boron Nitride 15

1.3.1 Introduction to h-BN 15

1.3.2 Two-dimensional materials for thermal management 18

1.4 MXenes 22

1.5 Research Objectives 24

1.5.1 Controllable Growth and Resist-free Transfer of Monolayer MoS_2 24

1.5.2 Understanding on Growth Mechanism of MoS_2 and MXene 25

1.5.3 Insulating BN as Heat dissipation 25

1.6 Structure of Thesis 26

Chapter 2 Controllable Growth and Resist-Free Transfer of Large Size MoS_2 29

2.1 Introduction 29

2.2 Methods 31

2.2.1 MoO_3-coated substrate preparation 31

2.2.2 CVD method 32

2.2.3 Thermal release tape transfer 33

2.2.4 Field-effect transistor fabrication 33

2.3 Results and discussion 34

2.3.1 Controllable growth of monolayer MoS_2 34

2.3.2 Resist-free transfer of MoS_2 44

2.4 Summary 52

Chapter 3 *in-situ* Observation on Growth Dynamics of Two-dimensional MoS_2 and MXene Flakes 54

3.1 Introduction 54

3.2 Methods 55

3.2.1 Sample preparation 55

3.2.2 TEM observation 55

3.2.3 Theoretical calculations 56

3.3 Results and discussion 58

3.3.1 Growth dynamic of MoS_2 58

3.3.1.1 Selected-area electron diffraction evolution 58

3.3.1.2 Growth process of MoS_2 61

3.3.1.3 Discussion 69

3.3.2 Growth dynamic of MXene 73

3.4 Summary 79

Chapter 4 Two-dimensional Boron Nitride Nanosheet for Efficient Heat Dissipation of High Electron Mobility Transistors 80

4.1 Introduction 80

4.2 Methods 83

4.2.1 Few-layer h-BN transfer. 83

4.2.2 Characterizations methods. 83

4.2.3 Finite element simulation. 84

4.3 Results and discussion 85

4.3.1Thermal conductivity measurement 85

4.3.2 Device performances 90

4.3.3 Finite element simulation 95

4.4 Summary 98

Chapter 5 Conclusions and Outlooks 100

5.1 Conclusions 100

5.2 Outlooks 102

References 104

List of Figures

Figure 1.1 Illustration of different kinds of typical ultrathin 2D nanomaterials.[3] 3

Figure 1.2 (A) The layer structure of MoS_2.[19] (B) Band structure of bulk, quadrilayer, bilayer and monolayer MoS_2.[38] 4

Figure 1.3 Schematic of (A) vapor sulfurization, (B) vapor reaction and (C) vapor transport method.[52] 6

Figure 1.4 Growth process of MoS_2 by the reaction between the MoO_3 and S.[60] 10

Figure 1.5 Procedures of the PMMA-assisted transfer method for 2D MoS_2.[54] 12

Figure 1.6 (A) Crystal structure of 2D h-BN.[36] (B) CVD setup for h-BN preparation.[81] 17

Figure 2.1 Schematic illustration of (A) the CVD system for growing MoS_2 and (B) the quartz boat loaded in the furnace. (C) Schematic plot of the relationship between the gaseous MoS_2 concentration and the distance *d* between MoO_3 source and growth substrate. 37

Figure 2.2 (A) to (E) Optical images of the MoS_2 product at different places of the growth substrate. (F) Optical image of a crystalline MoS_2 flake with the size of 308 μm. 39

Figure 2.3 (A) Surface coverage and average domain size and (B) Nuclei density of the MoS_2 as a function of the source/substrate distance. 41

Figure 2.4 (A) to (D) Optical images of crystalline MoS_2 flakes with size lager than 200 μm. 42

Figure 2.5 Optical images of the MoS_2 (A) thin film and (B) flake. (C) Raman spectra of the MoS_2 film, flake and boundary pointed in (A and B). (D) AFM images of MoS_2 domain boundary. (E) Height profiles taken across the dash line in (D). 43

Figure 2.6 (A and B) AFM images of MoS_2 triangle flake and thin film. (C and D) Height profiles taken across the dash line in (A and B). 44

Figure 2.7 Illustration of the transfer process assisted with a Cu thin film. Photographs of the transfer processes: (A) as-grown MoS_2 on SiO_2/Si substrate; (B) coating the MoS_2 with a Cu thin film; (C) sticking TRT; (D) peeling off TRT together with MoS_2; (E) heating the target substrate to peel off TRT; (F) the MoS_2 and Cu thin film on the target substrate; (G) the transferred MoS_2 after Cu etching. 46

Figure 2.8 (A and B) Optical images of the MoS_2 before and after PMMA transfer. (C and D) Optical images of MoS_2 before and after TRT transfer. (E and F) SEM images of MoS_2 transferred by PMMA method and TRT method. (G to J) Schematic of wrinkle generation during PMMA transfer process and corresponding photographs. 49

Figure 2.9 EDX spectra of the MoS_2 transferred by thermal release tape method with the element quantification results. 50

Figure 2.10 (A and B) AFM images of MoS_2 transferred by thermal release tape method and PMMA method. 50

Figure 2.11 (A and B) Raman and Photoluminescence (PL) spectra of as-grown, TRT-transferred and PMMA-transferred MoS_2. (C and D) Transfer and output characteristic for the back-gate FET based on the TRT-transferred MoS_2. 52

Figure 3.1 Schematic illustration of the experimental setup. (A) The preparation of heating E-chip with precursor, and the image of mounted Protochips Aduro heating stage (inset). (B) side-view of the as-prepared E-Chip. 58

Figure 3.2 The evolution of SAED patterns across a wide temperature range. The scale bar in (A) also applies to (B - G). 60

Figure 3.3 EDS spectra obtained at room temperature and 400 °C, respectively. 61

Figure 3.4 The growth dynamics of 2D MoS_2 thin-film during heating to 780 °C.

(A - E) Image sequences showing the evolution from initial “(002)-exposed” structure to the later stage of “(100)-exposed” structure. The insets in (A), (C) and (E) are the corresponding FFT patterns, respectively. The red arrows in (D) denote the remaining clusters at 700 °C. The scale bar in (A) also applies to (B - E). (F) Statistics of the clusters’ counts in frames (A - E). 63

Figure 3.5 Time-resolved *in-situ* TEM micrograph series showing the layer growth trajectory at 400 °C. 4L, 5L, and 6L stand for four-layer, five-layer, and six-layer MoS_2 structures, respectively. Colored sketches are included to identify the MoS_2 slabs. The scale bar in (A) also applies to (B - D). Time listed in all figures is relative to the beginning. 64

Figure 3.6 Precipitation and formation of 2D MoS_2 hexagonal nanoflakes during further heating beyond 800 °C. (A - D) Typical image frames showing MoS_2 particle development versus rising temperature, in both size growth and reshape. The scale bar in (A) also applies to (B - D). (E) Statistics of the nanoparticle diameter as a function of heating temperature from (A - D). 67

Figure 3.7 Sequential HRTEM images showing the structural transformation from irregular particles to faceted hexagonal nanoflakes. The inset in (C) is the corresponding FFT patterns. The scale bar in (A) also applies to (B - C). 68

Figure 3.8 The details of the particle attachment process happened at 840 °C (A - D) Sequences of in-situ TEM images indicating particle I and particle II merge into particle III. The red arrows denote [103] direction for the nearby particles. The scale bar in (A) also applies to (B - D). Time listed in all figures is relative to the first frame. 68

Figure 3.9 Schematic illustration of the structural evolution process during heating. “S” and “T” on orange discs stand for side-view and top-view, respectively. 69

Figure 3.10 The competition of total system energy between (002)-exposed structure and (100)-exposed structure as a function of particle size during

crystallization. (A) The energy density of particles along two orientations as a function of their volumes. The length, width and height of particles with minimal energy for (B) (002)-exposed and (C) (100)-exposed orientations. Note that the length is equal to width in the case of (100)-exposed orientations. (D) and (E) illustrate the shape and atomic arrangements for the particles along (002)-exposed and (100)-exposed orientations, respectively. 71

Figure 3.11 (A to D) The evolution of SAED patterns of high-concentration precursor across a wide temperature range. The scale bar in (A) also applies to (B - D). (E) Typical image showing the final product of Mo_2C flakes. (F) HRTEM showing one Mo_2C flake and the inserted is the FFT pattern. (G and H) The images showing the beginning and the ending of the Mo_2C attachment. 76

Figure 3.12 (A to D) The evolution of SAED patterns of low-concentration precursor across a wide temperature range. The scale bar in (A) also applies to (B - D). (E) Typical image showing the final product of MoC flakes. (F) HRTEM showing one MoC flake and the inserted is the FFT pattern. (G and H) The images showing the beginning and the ending of the MoC attachment. 78

Figure 4.1 (A) Raman spectra of FLBN at different temperatures. (B) Relationship between Raman frequency of FLBN and the temperature. (C) Schematic of thermal conductivity measurement. (D) Relationship between Raman frequency of FLBN and the laser power. 89

Figure 4.2 (A) Raman spectrum of FLBN at room temperature. (B) Absorption of FLBN at 400 nm to 800 nm wavelength. 89

Figure 4.3 (A) and (B) AFM image of FLBN and corresponding height profile. 90

Figure 4.4 (A) Optical image of the HEMT on commercial chips. (B) Schematic of the developed thermal management. 91

Figure 4.5 (A) Transfer characteristics of HEMTs with and without thermal management. (B) and (C) Output characteristics and detailed curve of HEMTs

with (solid line) and without (dash line) thermal management. (D) Saturation current improvement of HEMTs with thermal management. 93

Figure 4.6 (A) and (B) Smith charts of HEMTs without and with thermal management. 94

Figure 4.7 (A) and (B) Short circuit current gain and maximum available gain of HEMTs with and without thermal management. 95

Figure 4.8 (A) Temperature distribution of HEMTs without the thermal management at the dissipated power 4 W/mm. (B) and (C) Temperature distribution of HEMTs with the thermal management (with different thick BN locations) at the dissipated power 4 W/mm. (D) Temperature reduction of HEMTs operated at different dissipated power. 98

Chapter 1 Introduction

1.1 Background

Two dimensional(2D) materials have attracted much research interest since the discovery of graphene in 2004.[1] Graphene is a single layer of carbon atoms packed in a honeycomb crystal lattice with long-range π-conjugation.[2-3] This new-emerging material exhibits exceptional electrical, thermal and mechanical properties including high carrier mobility, excellent thermal conductivity and high Young's modulus, which leads to an explosion of research interest on applications based on graphene.[1, 4-5] Single layer of mechanical exfoliated graphene was found to possess a carrier mobility of more than 200,000 $cm^2V^{-1}s^{-1}$, because the high-quality 2D graphene lattice has low density of defects which serve as the scattering centers and impede charge transport.[6-7] With such high carrier mobility and ballistic charge transport, graphene is of great potential for the next generation semiconductor industry.[8] Another outstanding feature of graphene is the massless Dirac Fermions which is attributed to its unique electronic band structure.[9-10] The carriers can be tuned from holes to electrons and the doping levels can be entirely controlled by electrical gating or chemical gating, which facilitates the applications

of graphene in sensors or detectors.[10-11]

Mechanical exfoliation is the first reported method to produce graphene, which enables fundamental investigation on graphene.[1] However, the output is low and hinders the following device fabrication and study. To fulfill the potential of graphene, it is highly desirable to synthesize large-area and high-quality graphene. Chemical vapor deposition (CVD) assisted with metal catalyst (nickel or copper) has been reported to synthesize wafer-scale graphene with high uniformity and low defects.[12-13] The effects of various factors including catalyst properties (the carbon solubility, lattice parameter, crystal structure, etc.) and process parameters (temperature, pressure, source gas flow, etc.) on the final product have received substantial research efforts, which allows the controllable growth of large-area and high-quality graphene and promotes the development of applications based on graphene.[14-15]

The unprecedented properties of graphene inspire researchers to expand the 2D materials family. Various 2D materials with similar layered structure but versatile properties are explored in recent years. Hexagonal boron nitride (h-BN),[16] transition metal chalcogenides (TMDs),[17-20] metal-organic frameworks (MOFs),[21] covalent-organic frameworks (COFs),[22] MXene,[23] layered double hydroxides (LDHs),[24]

transition metal oxides,[25] layered metals[26] and black phosphorus (BP)[27] have greatly enriched the 2D materials family. Due to the extraordinary properties, these 2D materials are promising for various applications, such as electronics, sensors, energy storage, etc.[28-32]

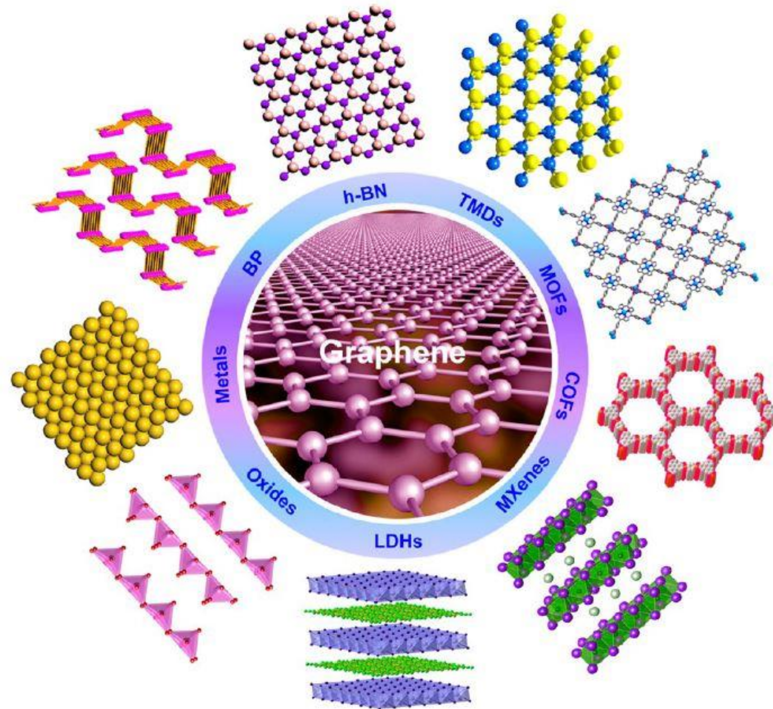

Figure 1.1 Illustration of different kinds of typical ultrathin 2D nanomaterials.[3]

1.2 Molybdenum Disulfide

1.2.1 Introduction to MoS_2

In the TMD family, monolayer MoS_2 has received the most intensive research efforts.[17, 19, 33-34] Each MoS_2 crystal layer consists of a plane of molybdenum atoms Mo sandwiched by two planes of

chalcogenide atoms S, which is shown in Figure 1.2A.[29] These atom planes within the layer are bound by covalent bonds while the interaction between layers are van der Waals forces. Two-dimensional MoS_2 shows different properties compared to bulk counterpart. As presented in Figure 1.2B, when the thickness of MoS_2 is reduced to monolayer, the indirect bandgap of ~1.3 eV in the bulk MoS_2 can change to a direct bandgap of ~ 1.8 eV.[35] Monolayer MoS_2 also have theoretical mobility of 200 to 400 $cm^2V^{-1}s^{-1}$ and high on/off ratios up to 10^{10}, making itself a promising material for future electronic device.[36-37] In addition, monolayer MoS_2 possesses excellent mechanical strength and high Young's modulus, which facilitates its application in flexible electronics.[38-39]

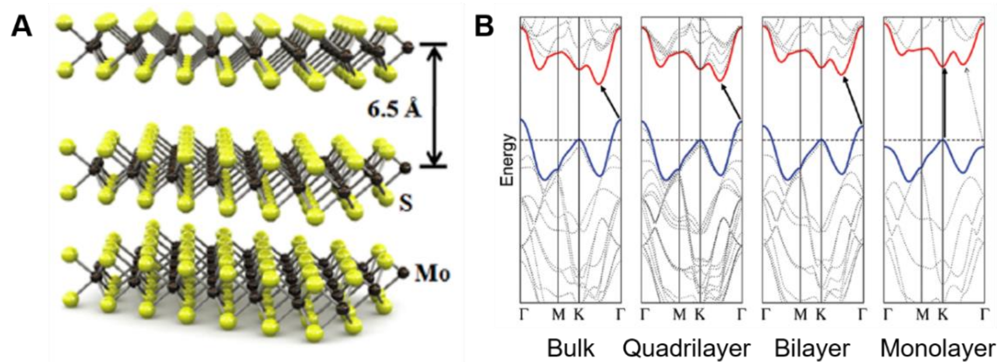

Figure 1.2 (A) The layer structure of MoS_2.[19] (B) Band structure of bulk, quadrilayer, bilayer and monolayer MoS_2.[35]

It has been suggested to utilize monolayer MoS_2 in field-effect transistors (FETs),[36] phototransistors,[40] nonvolatile memory,[41]

heterostructure devices,[42] biosensor,[43] solar cells,[44] etc. Novoselov *et al*. fabricated the very first FETs with few-layer MoS_2 as the channel material and SiO_2 as the gate dielectric layer.[7] The achieved mobility was only 3 $cm^2V^{-1}s^{-1}$, which is much lower than the theoretical value. Multiple following studies have significantly improved the transistor performance by various methods including the application of high-k gate dielectric or dual-gated configuration, promoting the application of monolayer MoS_2 on FET.[28, 45] Monolayer MoS_2 is also a competitive candidate in optoelectronic applications for its direct transition optical gap.[35] The first MoS_2 optoelectronic device was fabricated by Yin *et al*.[46] The phototransistor exhibited substantial photocurrent, short switching times and high photosensitivity. Taking advantaging of the extraordinary properties of monolayer MoS_2, various applications based on MoS_2 is still receiving intensive research efforts.[35]

1.2.2 Vapor deposition of MoS_2

For the exploration of the applications based on monolayer MoS_2, the reliable and facile preparation of monolayer MoS_2 is of great importance. Monolayer MoS_2 can be prepared by mechanical exfoliation.[47-48] Although the exfoliated MoS_2 flakes possess perfect lattice and are the beat for the pristine properties study, the output is

extremely low. The obtained MoS_2 flakes with a size ranging from few micrometers to tens of micrometers, cannot fit the industry requirements. Recently, vapor deposition methods have been significantly advanced in producing large-area and high-quality monolayer MoS_2. There are three main kinds of vapor deposition methods to produce MoS_2 film: vapor sulfurization, vapor reaction and vapor transport (shown in Figure 1.3).[49]

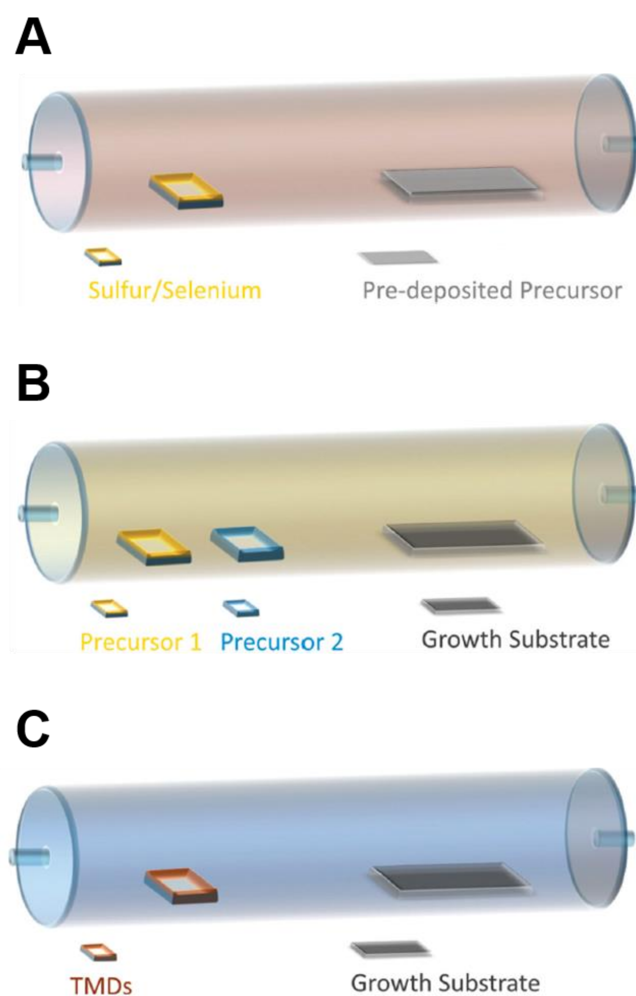

Figure 1.3 Schematic of (A) vapor sulfurization, (B) vapor reaction and (C) vapor transport method.[49]

Vapor sulfurization produce MoS_2 films by simply sulfurizing the metal or metal oxide films. Zhan *et al.* reported MoS_2 vapor deposition by sulfurization of molybdenum (Mo) film.[50] The metal Mo film was first deposited on silicon substrates followed by annealing in the sulfur vapor. The MoS_2 was grown by the direct chemical reaction between the metal and the sulfur. The size and the layer number of MoS_2 film was determined by the size and the thickness of the pre-deposited Mo films. Although the prepared MoS_2 film can be wafer-scale, the MoS_2 may exhibit metallic properties with a low on/off ratio because of the incomplete sulfurization of the metal impurities. An alternative Mo source is the molybdenum trioxide (MoO_3) films.[51] In this method, the MoO_3 layers coated on growth substrates were first reduced to MoO_2 in a hydrogen/argon atmosphere at 500 ℃. The substrates were then annealed in the sulfur environment at 1000 ℃. The reaction between the MoO_2 and sulfur can lead to the formation of MoS_2 thin films. The vapor sulfurization provides a rapid and simple process to prepare wafer-scale MoS_2 thin films. However, it has several limitations: it is difficult to control the uniformity of the pre-deposited Mo or MoO_3 layers, which will degrade the uniformity of the prepared MoS_2 films. The thickness of pre-deposited layers also needs to delicate control to grow MoS_2 films with desired layer number. Additionally, the

prepared MoS_2 films are mostly polycrystalline with small and uncontrollable grain size.

In vapor sulfurization methods, only sulfur is evaporated into vapor phase. Vapor reaction methods requires both Mo source and sulfur source react in the vapor phase. Lee *et al.* adopted vapor deposition with similar setup in Figure 1.3B.[52] They successfully synthesized MoS_2 thin films on SiO_2/Si substrates using MoO_3 and sulfur powders as precursors. Although the monolayer, bilayer and few-layer MoS_2 coexisted, the prepared MoS_2 films were highly crystalline with a size up to millimeters. They asserted the importance of the substrate treatment before the growth. The adopted graphene-like molecules, such as reduced graphene oxide, for the substrate treatment severed as nuclei and facilitated the layer growth of MoS_2. Similar vapor deposition was conducted by Najmaei *et al*.[53] They replaced MoO_3 powder with MoO_3 nanoribbons to grow MoS_2. They found the MoS_2 flakes preferred to form at step edges because the nucleation energy at step edges is lower than that at flat substrates. By patterning the substrates, they were able to control the nucleation of MoS_2 flakes. Zande *et al.* further developed the vapor deposition method.[54] Without small molecules or step edges as nucleation sites, they grew highly crystalline monolayer MoS_2 triangular flakes with a

lateral size of 120 μm. Except MoO_3 as precursor, molybdenum chloride ($MoCl_5$) was also reported as a Mo source by Cao's group.[55] They grew centimeters scale monolayer MoS_2 films with excellent uniformity and controllability.

MoO_3 and sulfur have been the most common used precursors for the MoS_2 CVD growth. Two possible growth process for the monolayer MoS_2 growth is proposed and shown in Figure 1.4.[56] The MoO_3 is partially reduced to MoO_x by sulfur vapor when the MoO_3 vapor is conveyed to the growth zone. The MoO_x may adsorb on the substrate followed by the reaction with sulfur to form MoS_2, or directly react with sulfur in the vapor phase and then the resulting MoS_2 precipitate on the substrates. In both understandings, the adsorption of MoO_x or MoS_2 cluster is essential which determines the nucleation density and grow rate and subsequently the final domain size of the MoS_2.

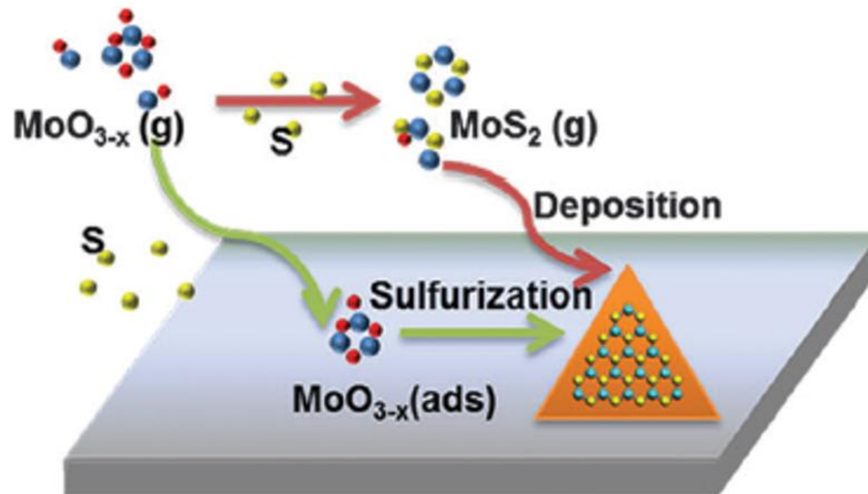

Figure 1.4 Growth process of MoS_2 by the reaction between the MoO_3 and S.[56]

Vapor transport is quite different from the vapor sulfurization and vapor reaction as no chemical reactions take place in the furnace. This method involves the evaporation and recrystallization of the TMDs. Wu *et al.* developed the vapor transport to synthesize high-quality MoS_2 monolayer.[57] The MoS_2 powder was first evaporated at the up-steam region of the furnace. The vapor phase of MoS_2 was transported to the down-steam where the growth substrate was heated at a lower temperature than that at the up-steam. The vapor phase of MoS_2 precipitated and formed monolayer MoS_2 on the growth substrate. Although the prepared monolayer MoS_2 has excellent optical quality and high crystallinity, it is more frequent to find thicker layers.

Vapor deposition is demonstrated as an efficient method to

produce large-area and high-quality monolayer MoS_2. To fabricate electronic device based on monolayer MoS_2, it is favorable to grow continuous MoS_2 thin films with large domain size and high surface coverage. To attain the favorable MoS_2, it is essential to investigate the effect of grow parameters and control the morphology of monolayer MoS_2 by adjusting the growth conditions.

1.2.3 Transfer of MoS_2

Vapor deposition methods for MoS_2 preparation typically require high temperature (up to ~800 ℃), which cannot meet the requirements of integrated circuit technology, and restricts the substrate selection. To fulfill the potential of the MoS_2, it is important to transfer MoS_2 from the growth substrate to another without compromising the quality of MoS_2. Conventionally, the as-grown MoS_2 on the growth substrates like SiO_2/Si or sapphire substrates is transferred with PMMA as the carrier material shown in Figure 1.5.[51] The transfer process for 2D materials can be roughly divided into two steps: to lift off 2D materials from the growth substrates and to remove the carrier materials after 2D materials are attached to the target substrates. This PMMA-assisted transfer method for MoS_2 is translated from the PMMA transfer method for graphene.[58] As graphene emerged in an earlier time, the transfer methods for graphene have been extensively studied.[58-59] It is

reasonable to adapt the process of graphene transfer.

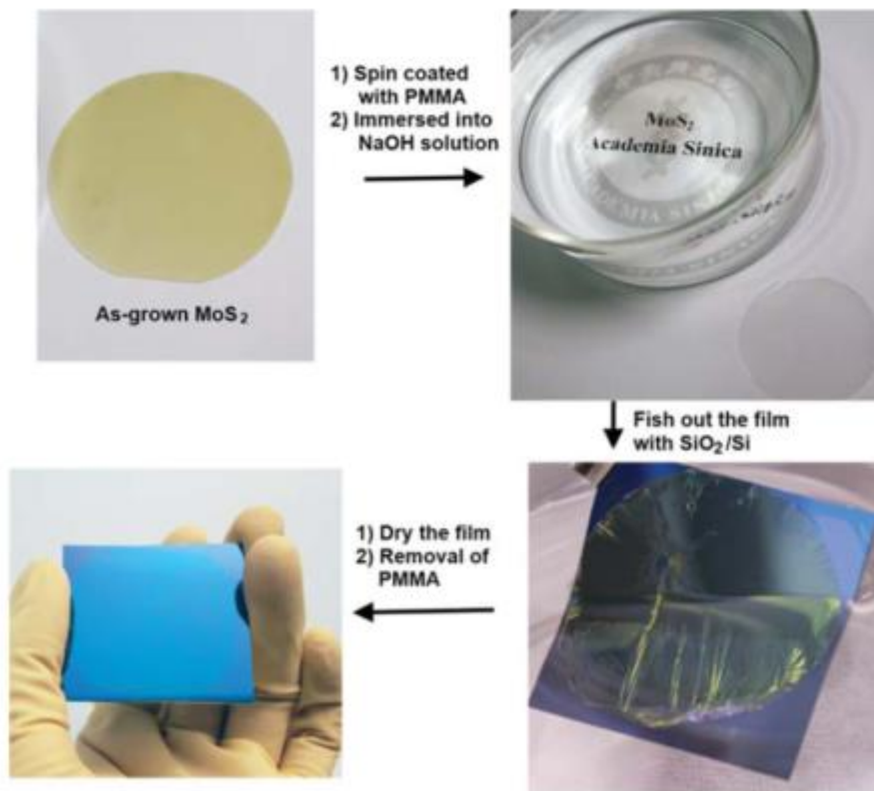

Figure 1.5 Procedures of the PMMA-assisted transfer method for 2D MoS_2.[51]

However, there are many problems when we simply apply graphene transfer processes in MoS_2 transfer due to their different growth mechanism. For graphene, to lift graphene off the growth substrates (Ni or Cu) can be easily achieved by etching the substrate. In contrast, the growth substrate for MoS_2 films is normally SiO_2/Si substrate or sapphire which cannot be simply etched. Although the SiO_2/Si substrate can be etched by hot base solution, bubbles are easily generated in the etching process and can be trapped by the PMMA thin film, which will induce capillary force and give rise to wrinkles or

even cracks in the 2D MoS_2. Additionally, the complete removal of polymer residues still remains a challenge even in graphene transfer.[58-62] These problem significantly degrade the properties of MoS_2 and the performance of the devices based on MoS_2.

Gurarslan *et al.* demonstrated a surface-energy-assisted transfer method which allows one to lift off the centimeter-scale MoS_2 films without etching the growth substrates.[63] Polystyrene (PS) replaced the PMMA as the carrier materials. They found the growth substrate, sapphire, is hydrophilic, while the prepared MoS_2 film is hydrophobic. When a droplet of water was placed on the PS layer, due to the different surface energy of MoS_2 and the growth substrates, the water droplet penetrated between the MoS_2 film and the growth substrates and mildly peeled the PS with MoS_2 off the substrates. Because of the gentle lift off by water penetration, this method reduces the mechanical force induced by bubble and the impurities from chemical etchants, which are difficult to be avoided when hot base solution is etching the growth substrates of MoS_2. Li *et al.* also developed similar transfer method for nanostructures.[64] They coated the nanostructures with the hydrophobic polymer layer. The water droplet penetrated between the polymer and the SiO_2 substrates can peeled off the polymer layer with the nanostructures.

However, these developed methods continue to use polymer as carrier materials, which are the resource of residuals on the surface of 2D materials. It is reported that the residuals are still observed on the surface of transferred graphene even after several-hour treatment with acetone.[65-66] During the PMMA cleaning process, long and heavy molecular fragments can attach to the formed free radical site and interact with the adjacent polymer chain, making the residuals difficult to remove.[61] These residuals significantly degrade the electrical properties of graphene.[65-66] Several techniques are developed to remove polymer contaminations, such as, toluene or chloroform treatments, plasma exposure and annealing under the mixed gases (hydrogen and argon) or high vacuum conditions.[65, 67-70] Although these techniques exhibited some degrees of success in graphene transfer, they involve complicated process flows or specific chemicals. These techniques require a harsh environment to completely remove polymer residuals.[58] Unfortunately, the harsh environment has uncertain influence on monolayer MoS_2, which is still subject to further investigation.[64] Therefore, it remains a challenge to develop a resist-free and wrinkle-free transfer method for 2D MoS_2.

1.3 Hexagonal Boron Nitride

1.3.1 Introduction to h-BN

Two-dimensional h-BN, also known as white graphene, consists of a similar crystal structure with graphene, but the carbon atoms are replaced with boron and nitrogen atoms.[71] Although the structure is similar to that of graphene, 2D h-BN exhibits some different properties. The pristine h-BN is a typical 2D insulator with a wide band gap of ~ 5.9 eV.[72] It is stated that the insulating 2D h-BN can be utilized as dielectric layers in graphene transistors and significantly improve the performance of devices.[73] Two dimensional h-BN has comparable dielectric property and breakdown field with SiO_2 and an atomically smooth surface without dangling bonds and charge traps, which making itself a competitive candidate as gate dielectric layer in transistors based on 2D materials.[74] In addition, 2D h-BN has an excellent thermal conductivity (200 ~ 400 $Wm^{-1}K^{-1}$),[75] which is almost two orders of magnitude higher than SiO_2 and is another advantage for heat spreading in devices.

There are three common used methods to prepare 2D h-BN: mechanical exfoliation, liquid exfoliation and CVD. The mechanical exfoliated h-BN has a perfect crystalline structure and fewer defects

than those prepared by other methods, which is the most suitable for the exploration of the intrinsic properties of 2D h-BN.[76] However, the mechanical exfoliation has an extremely low yield and limits the applications of 2D h-BN. Liquid-phase exfoliation uses several surfactant solutions assisted with sonication to break the van der Waals interaction between layers and produce 2D h-BN.[77] Although it can produce large quantities of 2D h-BN, the layer number and the grain size are difficult to be controlled using this method. The CVD method is the most promising methods to synthesize 2D h-BN with control over layer number and crystalline structures, which can meet the requirement for the industrial process.[78-79]

The CVD method for h-BN growth has been extensively studied. Precursors including BF_3/NH_3, B_2H_6/NH_3 and BCl_3/NH_3 can be used to grow h-BN nanosheets.[71] In such system containing two precursors, controlling the ratio of boron source and nitrogen source (NH_3) is crucial to attain stoichiometric h-BN films. The synthesis via the pyrolysis of the single precursor can be simplified because the utilized precursors, such as ammonia borane, have a 1:1 B/N stoichiometry in the precursor.[78] Large-area monolayer h-BN has been reported to be grown on nickel (Ni) and copper (Cu) substrates using single precursor.[78-79] Ni and Cu substrates serve as a catalyst in

the h-BN growth and determine the morphology and properties of the final product.[74] In the CVD growth, the borazine gas introduced into the chamber was decomposed on the metal substrates and formed the monolayer h-BN. It is reported that the pre-growth treatment to Cu substrates like thermal annealing and chemical polishing can reduce the impurity particles and produce pure h-BN films with an atomically smooth surface and improved crystallinity.[80] The precursor pressure and the hydrogen partial pressure are also key factors for the growth of 2D h-BN and was investigated by Sutter *et al.*[81] The research shows that low partial pressure precursor can lower the density of individual h-BN domains and help these domains grow to a size of tens of micrometers. The increased hydrogen partial pressure is also found to reduce the nucleation density and growth rate as the atomic H will etch the h-BN edges.

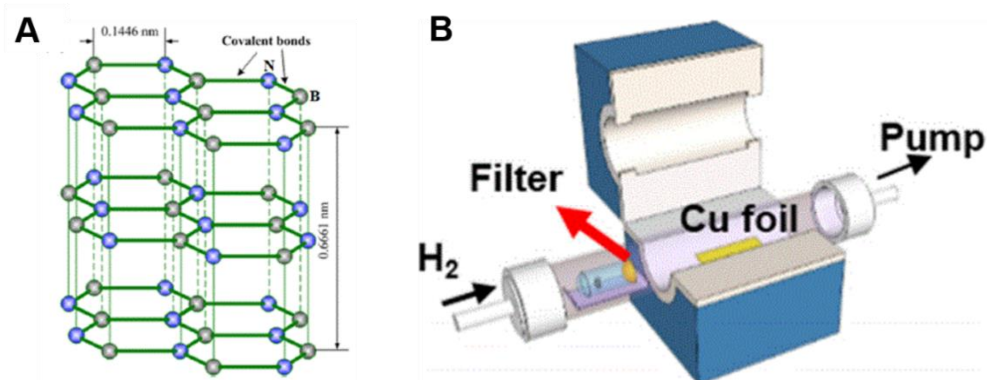

Figure 1.6 (A) Crystal structure of 2D h-BN.[71] (B) CVD setup for h-BN preparation.[78]

1.3.2 Two-dimensional materials for thermal management

The rapid development of modern electronics has enhanced the performance of power circuits including microprocessor and power amplifiers.[82] However, the increasing power density in these electronic devices creates thermal challenges that may limit the reliability and feasibility of the devices. In some processors modules, the power for excellent computing performance can reach higher than 250 W, leading to at least 1 kW heat flux in a four-socket computing system.[82] High electron mobility transistors (HEMTs) based on AlGaN/GaN heterojuction have been widely used for high-frequency and high-power communication applications, of which the power can reach an extremely high density (approximately 19 W/mm).[83-84] The increasing power dissipation generates massive heat flux in the devices or chips and elevates the average temperature of the whole system.[85-86] While the high value of power has certain influence on the devices or chips, the spatial distribution of the power is also of concern. The power dissipation in the devices or chips can be highly non-uniform. The local functional areas can reach a power density of one order magnitude higher than the average.[87] These regions are regarded as hotspots where the local temperature is much higher than

the average temperature. In HEMTs, for example, most of applied bias drop in the channel takes place at the gate electrode edge near the drain side, where the electric field is strongest.[88-89] Most quantities of heat are generated from this location, which serves as the heat source and has the maximum temperature for the whole device.

The thermal management is of great importance for the electronic devices operated at high power, because the elevated temperature induced by inefficient power dissipation will degrade the performance and reliability of the devices. It is stated that the increased temperature in the HEMTs can decrease the electron mobility, reduce the maximum drain current, degrade the RF performances, and adversely affect the reliability.[90] The effective thermal management should provide sufficient cooling rate to keep the temperature of the whole chips including the hotspots under the standard working temperature. To withdraw the massive heat flux from the chips, efforts to decrease the thermal resistance between the chips and the ambient have been attempted, which help to spread the heat to the ambient and reduce the temperature of the chips.[91] In commercial HEMTs, silicon carbide (SiC) and diamond substrates with higher thermal conductivity (K= ~350 $Wm^{-1}K^{-1}$ and ~1200 $Wm^{-1}K^{-1}$, respectively) have replaced the conventional sapphire substrates (K= ~30 $Wm^{-1}K^{-1}$).[91]

Except dealing with the massive heat flux in the whole chip at the chip-level or package-level, there is a great desire to have efficient heat dissipation at the local functional area. The chip-level or package-level thermal management fails to address the hotspots at micro/nanoscale. The development of 2D materials provides new solution to microscale heat dissipation. Yan *et al.* reported exfoliated few-layer graphene was utilized as lateral heat spreaders on top of HEMTs and the developed thermal management successfully reduced the temperature at hotspots of the devices.[92] The graphene was transferred onto the drain electrode with exceptionally delicate control and connected the electrode with heat sinks. The heat sinks used in this work is graphite, which can be replaced with other metallic sink. The superior in-plane thermal conductivity of graphene allows itself to effectively remove large heat flux from the hotspots. The heat flux is then transported to the heat sink and can be withdrawn to the ambient without affecting the transistors. The simulations also show the maximum temperature is decreased by more than 20 ℃ on the devices operated at ~ 13 W/mm with developed thermal management. When the substrate for devices was changed from SiC to sapphire, the temperature reduction becomes more significant, indicating the importance of thermal management in power devices. It is worth

noticing that the anisotropic cross-plane thermal conductivity of graphene enables spreaders dissipate the heat in the lateral direction instead of in the vicinity of the devices. Gao *et al.* further investigated the effectiveness of graphene as heat spreaders.[93] They utilized the graphene with controlled layer number and evaluated the thermal performance by Platinum thermal evaluation chips. The hotspot with a heat flux of 430 Wcm^{-2} was covered by graphene with different layer number. With higher thermal conductivity, monolayer graphene heat spreaders decreased the temperature at the hotspot by ~ 13 ºC while only ~ 8 ºC temperature reduction was observed at the hotspot with multilayer graphene as heat spreaders.

Although graphene has a superior thermal conductivity and is applicable to reduce the temperature at hotspots in the power devices, graphene is also electrical conducting,[94] which may forbid itself directly contacting the hotspots located at functional regions. The excellent electrical conductivity of graphene can give rise to short circuit, and cause the malfunction of the whole circuits. This feature requires additional photolithography step to pattern graphene and complicates the processing for thermal management in the industry process. Therefore, the ideal material for thermal management will be highly thermal conducting and electrical insulating. Two-dimensional

h-BN, as an intrinsic insulating, is also a highly thermal conducting materials. While the thermal conductivity of bulk h-BN is around 400 $Wm^{-1}K^{-1}$, the theoretical calculation reveals that the room temperature thermal conductivity of the single layer h-BN can reach 600 $Wm^{-1}K^{-1}$.[95] This higher thermal conductivity results from the decrease of phonon-phonon scattering in the monolayer h-BN. Although large area few-layer h-BN can be grown by CVD now, limited studies show the application of h-BN for thermal management of power devices at micro-scale level.

1.4 MXenes

MXenes, also regarded as transition metal carbides (TMCs), are a large 2D materials family with many intriguing properties including high hardness, high melting point, high stability, low chemical reactivity and excellent electrical conductivity.[96] Several MXenes like molybdenum carbide (Mo_2C or MoC) and tungsten carbide (W_2C or WC) even possess superconductivity.[97] MXenes have a crystal structure of stacking planes of transition metal atoms and carbon atoms.[98] With different stacking sequences of planes with transition metal atoms and carbon atoms, the MXenes may exhibit different properties. For instance, MoC in WC phase is calculated to have a

higher superconducting transition temperature than that in NaCl phase.[99]

MXenes can be prepared by selectively etching the layered bulk compounds MAX phases, where M denotes transition metal, X is carbon and A is mainly an element from group IIIA or IVA.[23] The plane of A atoms in MAX phase connect two adjacent MXene layers by forming the metallic bond with the metal atom plane.[100] The interaction is so strong, which is different from the weak van der Waals interaction in graphite or bulk TMDs. The MXene can be liquid exfoliated by selectively etching the A atom layers using hydrofluoric acid (HF) instead of mechanical exfoliation.[23] Recently, Ren's group reported the very first CVD growth of ultrathin crystal Mo_2C sheet.[97] They utilized methane as the carbon source and a Mo foil covered by a Cu foil. At a high temperature of ~ 1085 ºC, the Cu foil was melted and a Cu-Mo alloy formed at the interface, which allowed the Mo atoms to diffuse to the Cu surface and to react with carbon atom decomposed from methane. The prepared ultrathin Mo_2C has a thickness of few nanometers with a lateral size of 100 μm. The development of CVD growth of MXenes triggers the investigation of facile growth of MXenes.

1.5 Research Objectives

1.5.1 Controllable Growth and Resist-free Transfer of Monolayer MoS_2

Various applications based on monolayer MoS_2 has been developed.[28-29, 36] The reliable and facile preparation of monolayer MoS_2 is of great importance for the exploration of the applications. Chemical vapor deposition (CVD) has been demonstrated as an efficient method to produce large-area and high-quality monolayer MoS_2.[52-53, 101] To fabricate electronic device based on monolayer MoS_2, it is favorable to grow continuous MoS_2 thin films with large domain size and high surface coverage. The first aim of this study is to investigate the effect of grow parameters on the morphology of final product and to control the morphology of monolayer MoS_2 by adjusting the growth conditions.

The vapor deposition of monolayer MoS_2 require high growth temperature (up to ~800 ºC), which highly restricts the substrate selection. To fulfill the potential of the monolayer MoS_2, it is important to transfer monolayer MoS_2 from the growth substrate to another without compromising the quality. However, the conventional PMMA-mediated transfer technique has several drawbacks, which

will significantly degrade the properties of transferred MoS_2.[63-64] It is crucial to develop a facile transfer method allowing the transferred MoS_2 to maintain the properties, which is the second aim of this study.

1.5.2 Understanding on Growth Mechanism of MoS_2 and MXene

Large-area and high-quality ultrathin MoS_2 and MXene both can be grown by CVD method.[52-53, 97, 101] However, it still remains a challenge how to control the grain size and orientation of ultrathin MoS_2 and MXene due to the lack of direct and insightful observations. A microscopic understanding on growth pathways of 2D materials is of great importance for controllable synthesis and rational design of functional nanostructures. Technical advances in transmission electron microscopy (TEM) with high spatial and temporal resolution allow us to monitor the real-time growth processes at atomic scale and understand the growth mechanism for low-dimensional materials. The third aim of this study is to understanding the dynamic growth 2D materials with direct TEM observations.

1.5.3 Insulating h-BN as Heat dissipation

The thermal management is important in power devices as the

operation power can reach extremely high value.[83, 102] Without efficient heat dissipation, the elevated temperature in the devices will degrade the performance and reliability of the devices.[90] The ideal material for thermal management are desired to be highly thermal-conducting but electrical-insulating. Two-dimensional h-BN has high resistivity and high in-plane thermal conductivity (200 ~ 400 $Wm^{-1}K^{-1}$),[75] which is of great potential in the thermal management. Although large area 2D h-BN can be grown by CVD now,[78-79] limited study shows the application of h-BN in thermal management. The effectiveness of 2D h-BN in heat dissipation requires to be further investigated. The last aim of this study is to explore the application of 2D h-BN in thermal management of power devices and integrated circuit.

1.6 Structure of Thesis

The chapters of this thesis are organized as follows:

Chapter 1: Introduction. In this chapter, the structures preparation and properties of 2D materials including graphene, MoS_2, h-BN and MXenes are introduced. This chapter also systematically review the vapor deposition of monolayer MoS_2 and the facile transfer methods for nanomaterials. The applications of thermal management utilizing

unique thermal-transporting properties of 2D materials is shown.

Chapter 2: Controllable Growth and Resist-Free Transfer of Large Size MoS_2. This chapter will investigate the controllable CVD growth of monolayer MoS_2. The effects of the nuclei density on the MoS_2 domain size and surface coverage will be systematically studied. Afterwards, this chapter will demonstrate a facile process of transferring the monolayer MoS_2 assisted with a copper thin film. This transfer process will be compared with the conventional PMMA-assisted method.

Chapter 3: Direct *in-situ* TEM Observations on Growth Mechanisms of Two-Dimensional MoS_2 and MXene Flakes. This chapter will present the dynamic growth process of 2D materials, MoS_2 and MXene, as the evolution of growth temperature. The understanding on growth mechanism of 2D material will be also developed and discussed in this chapter.

Chapter 4: Two-dimensional Boron Nitride Nanosheet for Efficient Heat Dissipation of High Electron Mobility Transistors. In this chapter, a method for local thermal management utilizing thermal-conducting but electrical insulating h-BN will be presented. The effectiveness of the developed heat dissipation will be studied.

Chapter 5: Conclusions and outlooks. In this chapter, the thesis will be summarized and some personal perspective for the future of 2D materials will be proposed.

Chapter 2 Controllable Growth and Resist-Free Transfer of Large Size MoS_2

2.1 Introduction

Two dimensional (2D) layered materials have attracted much attention due to their unique properties.[17, 19, 29] The existence of a semiconductor bandgap in transitional metal dichalcogenides (TMDs), including MoS_2, WS_2, $MoSe_2$ and WSe_2, makes them promising for future logic devices and circuits beyond graphene. Chemical vapor deposition (CVD) has been demonstrated as a deterministic method in producing large-area and high-quality monolayer 2D layered TMD materials.[50-51, 103] According to the method of placing the source materials in the furnace, the CVD growth can be divided into vapor sulfurization and vapor reaction. In the vapor sulfurization, the source materials, e.g., Mo, MoO_3 or $(NH_4)_2MoS_4$, are coated on a substrate, which is followed by sulfurization in a sulfur vapor environment at high temperature.[50-55, 103] The TMDs grown by sulfurization method usually have large area and good uniformity but poor crystalline quality, small domain size, and uncontrollable layer number. In contrast, the source materials, e.g., MoO_3 or $MoCl_5$, are evaporated in

the vapor deposition method.[52-55] The TMDs grown on a substrate usually have relative large domain size but poor surface coverage. These two kinds of CVD methods both require high growth temperature (up to ~800 ºC), which cannot meet the requirements of the back-end processing of integrated circuit technology and restricts the substrate selection, e.g., the plastic substrate for flexible electronics applications.

To fulfill the potential of the 2D layered TMD materials, it is important to grow large domain-size and high surface-coverage TMDs and transfer TMDs from the growth substrate to another without compromising the quality of the TMDs. The conventional PMMA-mediated transfer technique suffers from the failure of completely removing polymeric residues and the formation of the wrinkles in the TMDs. These drawbacks significantly degrade the performance of the TMD-based devices. Recently, Gurarslan *et al.* and Li *et al.* reported that monolayer MoS_2 can be peeled off from the growth substrates based on different surface properties between the polymers and the growth substrates.[63-64] These methods, compared to conventional PMMA transfer, prevent the crack of the monolayer MoS_2 during substrate etching process, but fail to avoid the use of polymer carriers, which is the main reason for residues and wrinkles. It

is highly desirable to develop a resist-free and wrinkle-free transfer method.

In this chapter, we first controllably grow monolayer MoS_2 from triangular islands to continuous thin film using vapor deposition method. By tuning the distance between the source and the growth substrates, we demonstrate the growth of monolayer MoS_2 thin film with large domain size and high surface coverage. To avoid the polymeric residue and wrinkles generated in the PMMA-mediated transfer method, we present a facile transfer process using thermal release tape (TRT) assisted with a Cu thin film, preventing the MoS_2 from directly contacted to the glue and giving rise to the resist-free MoS_2 surface. The tape and Cu thin film also provide mechanically robust supports for the monolayer MoS_2, reducing the wrinkles generated during the transfer process. Our method allows us to transfer MoS_2 from the growth substrate onto arbitrary substrates without observable polymeric residues or wrinkles.

2.2 Methods

2.2.1 MoO_3-coated substrate preparation

MoO_3 was first prepared by conventional hydrothermal synthesis

and fully spread in ethanol.[104] The mixture was then dropped onto a Si substrate with 300-nm-thick SiO_2 and the substrate was heated to approximately 110 ℃ on a hot plate to evaporate ethanol. The procedure was repeated until the remaining MoO_3 completely covered the substrate.

2.2.2 CVD method

MoS_2 was grown on a Si substrate with 300-nm-thick SiO_2 by CVD method. The growth substrate faced downwardly above a quartz boat. Directly below the growth substrate, a 5 mm × 5 mm MoO_3-coated substrate was placed as the Mo precursor. The mass of MoO_3 on the substrate is 10 ~ 30 mg. The quartz boat was then loaded into a 1-inch-diameter quartz tube and centered in the furnace. A porcelain boat with sulfur was located in the upstream region outside the furnace, approximately 25 cm away from the middle. Before the MoS_2 growth, the system was flushed with 200 sccm of argon (Ar) gas for 10 min. Afterwards, the MoO_3 was heated from room temperature to ~ 800 ºC at a rate of 20 ºC/min and then maintained at 800 ºC for 10 min. Meanwhile, the sulfur was sublimated at 160 ºC and carried by Ar gas flow to the growth zone. The Ar gas flow was initially 150 sccm, and later reduced to 60 sccm for stabilizing the MoS_2 growth when the growth region reaches 700 ºC. The growth ended with natural cooling

of the system.

2.2.3 Thermal release tape transfer

The substrate with as-grown MoS_2 sample was first coated with a ~60-nm-thick Cu thin film by thermal evaporation. A thermal release tape was then pressed onto the SiO_2/Si substrate and was gently peeled off. As a result, the Cu/MoS_2 stack was separated from the SiO_2/Si substrate and attached to the tape. Secondly, the tape carrying Cu/MoS_2 was pressed onto a targeted substrate. The whole stack was heated to approximately 120 ℃. The adhesiveness between thermal release tape and Cu was weaken. The tape could be easily peeled off, leaving the Cu/MoS_2 on the target substrate. Finally, the Cu thin film was etched using the mix of 15% ammonium persulphate and deionization water.

2.2.4 Field-effect transistor fabrication

The FET device was fabricated based on the TRT-transferred MoS_2 on the 300 nm SiO_2/Si substrates. The pattern of the electrodes was defined by standard photolithography. A 100-nm thick Au thin film was evaporated by thermal evaporation as metal electrodes and followed lift-off. The channel length and width of the obtained FET were identified by optical microscopy.

2.3 Results and discussion

2.3.1 Controllable growth of monolayer MoS_2

We developed a CVD setup at atmospheric pressure similar to that reported in ref[105] (Figure 2.1A). The temperatures of the locations for placing MoO_3 and S precursors were controlled by the furnace and the heating belt, respectively. The sulfur gas was carried into the growth zone by Ar gas flow. Excessive amount of S was used to ensure MoO_3 precursor react completely. In the previous works,[106-107] the MoO_3 powder and the growth substrate were placed in the middle and downstream of the furnace, respectively. In our study, we replaced commonly-used MoO_3 powder with a MoO_3-coated substrate as the precursor to quantitatively control the amount of MoO_3 by the size of the MoO_3-coated substrates. The growth substrate was placed on top of the quartz boat, facing downwardly towards the MoO_3 precursor substrate, as schematically illustrated in Figure 2.1B.

The MoS_2 grown by vapor reaction methods are usually triangular flakes with low surface coverage, in agreement with those reported in existing literatures.[52, 106] For the fabrication of electronic device, it is highly desired to grow continuous and large domain size MoS_2 thin films up to wafer scale. The growth of the continuous MoS_2

thin film is presumed to include five major steps:[55, 107-108] (1) the sublimation of the precursor (MoO_3 and S) and the mass transport of the precursor to the region close to growth substrate, (2) the reaction of MoO_3 and S to form gaseous MoS_2, (3) the precipitation of supersaturated MoS_2 vapor onto the substrate to produce solid-phase MoS_2 nuclei, (4) the MoS_2 growth on the substrate controlled by kinetic factors, and (5) the coalescence of the adjacent MoS_2 domains to merge into continuous thin films.

In general, the nuclei density is closely related to the average domain size of MoS_2. The increase of the nuclei density can improve surface coverage but decrease the average domain size. In contrast, the suppression of nuclei density helps to grow large-size MoS_2 domain,[109] though the product from low-density nuclei usually has poor surface coverage. Therefore, it is quite important to optimize the nuclei density to fabricate continuous MoS_2 thin films with large domain size as well as surface coverage. The concentration of gaseous MoS_2 (C_g) has been shown with an important thermodynamics and kinetics factor for the precipitation reaction $C_g \rightarrow C_s$, where C_s is the concentration of the active species at the substrate surface. In our CVD setup, the excessive S precursor outside the furnace is carried by Ar gas. The S concentration almost keeps constant in the middle of the

furnace tube, and has a negligible influence on the nuclei density. On the other hand, the MoO_3 precursor is thermally evaporated from the bottom of the quartz boat, reacts with S to form gaseous MoS_2, and diffuses towards the growth substrate. The distance between the MoO_3 precursor substrate and the MoS_2 growth position is defined as d. The relationship between the concentration of gaseous MoS_2 (C_g) and the distance d can be described according to equation (2.1):[110]

$$Cg(d,t) = Cg(0,t)\exp\left(-\frac{d^2}{4Dt}\right) \qquad (2.1)$$

Where $C_g(d,t)$ and $C_g(0,t)$ are the gaseous MoS_2 concentration at given distance d and the source substrate, t is the time, and D is the diffusion constant. The equation is roughly plotted in Figure 2.1C. The changes of d create a gaseous MoS_2 concentration gradient which significantly affects the final product of MoS_2.

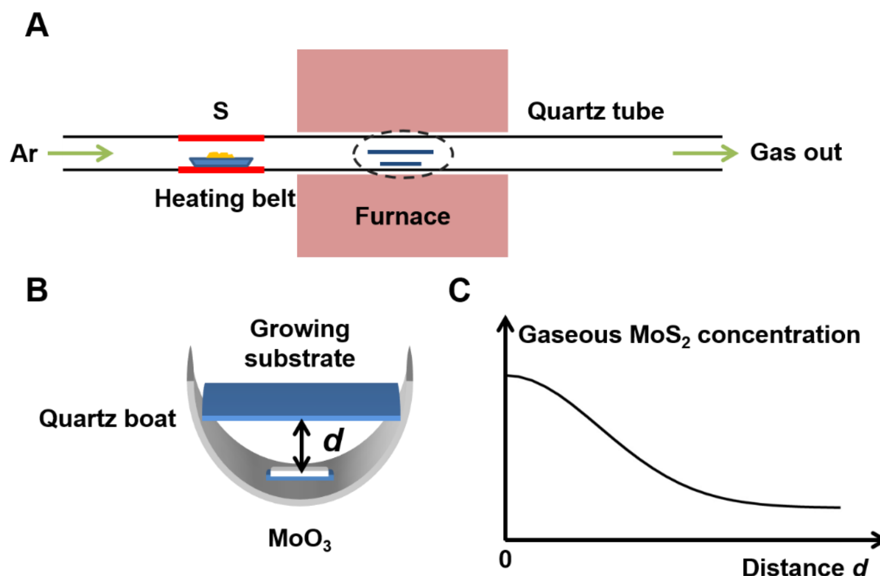

Figure 2.1 Schematic illustration of (A) the CVD system for growing MoS_2 and (B) the quartz boat loaded in the furnace. (C) Schematic plot of the relationship between the gaseous MoS_2 concentration and the distance *d* between MoO_3 source and growth substrate.

Figure 2.2A to E show optical images of the typical as-grown MoS_2 at different source/substrate distance. In our setup, when the distance is kept around 5 mm, the concentration of gaseous MoS_2 C_g is high. Figure 2.2A shows that the substrate surface was 100% covered by MoS_2 thin film. The domain boundaries of the thin film can be easily observed by optical microscopy because the boundaries provide extra step for MoS_2 growth and the thickness near the boundaries reaches several layers which contrast with the monolayer films. The mean domain size was approximately 20 μm and the shape of the MoS_2 domain deviated from triangle or rhomboidal. With the highest

C_g at short distance, a lot of sites at the substrate surface can satisfy the thermodynamic conditions, resulting in high nuclei density. When the distance increased to 6.5 mm, the MoS_2 thin film 100% covered the growth substrate, as shown in Figure 2.2B. The nuclei density slightly decreases with lower C_g, which allocates larger space for each nucleus to grow before coalescence. As a result, the average domain size was increased around 40 μm. High nuclei density helps to improve the surface coverage but limits the domain size. Figure 2.2C shows the optical image of the edge of MoS_2 thin film, where the distance d is around 7 mm. Triangular flakes were distributed at the edge of MoS_2 thin films. Some overlapping flakes illustrate the initial process of the formation of the thin film. As the nuclei density is low in the outer place, enough space is spared for MoS_2 domain to grow independently. Therefore, the mean domain size increased to 75 μm. However, the overall surface coverage decreased to 85%. It is highlighted that at this distance we have ever grown the MoS_2 flake with the size of 308 μm shown in Figure 2.2F. This large domain size is attributed to the prefect nuclei density and supply transport. With the C_g continuously declines with the larger distance (7.5 mm), the dominant products were triangular MoS_2 (Figure 2.2D) because the nuclei density is suppressed by the low gaseous MoS_2 concentration. The surface

coverage and the mean domain size both dropped to 70% and 60 μm, respectively. Low-density nuclei guarantee that most flakes can be grown independently without overlapping with adjacent flakes until the end of growth. When the *d* is further increased to 9 mm, the products were triangular flakes with the mean size of ~ 25 μm and the surface coverage was only ~ 30%, as shown in Figure 2.2E. The reduced C_g fails to supply sufficient source and the growth of nuclei is consequently limited, resulting in the decrease of mean domain size.

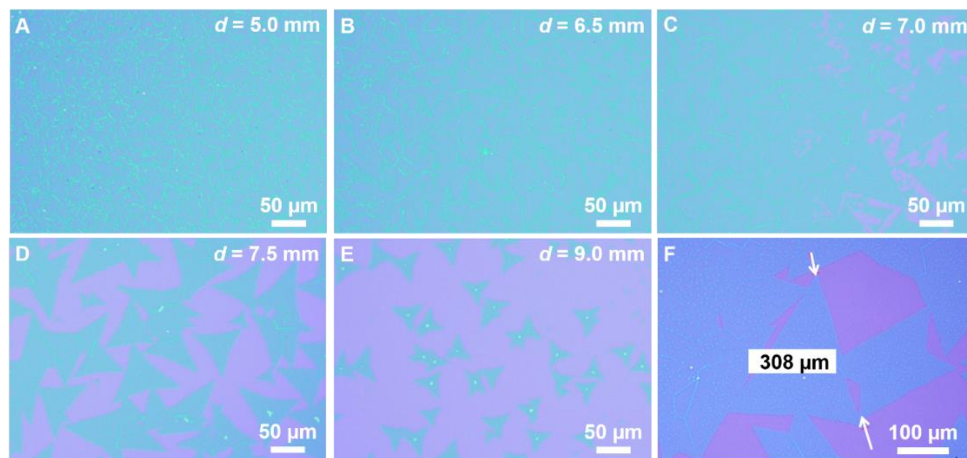

Figure 2.2 (A) to (E) Optical images of the MoS_2 product at different places of the growth substrate. (F) Optical image of a crystalline MoS_2 flake with the size of 308 μm.

The surface coverage and the average domain size as a function of the source/growth distance are roughly summarized in Figure 2.3A. The nuclei density is calculated and plotted in Figure 2.3B. It exhibits two distinct trends in the both two plots with the distance of 7 mm as

the boundary point. In the region where the growth substrate is close to the precursor substrate (less than 7 mm), the continuous MoS_2 thin films are dominant products. The shape of the MoS_2 domain exhibits irregular, deviating from triangle or rhomboidal. The surface coverage remains 100% and slightly decreases near the edge of MoS_2 thin films. Meanwhile, the average domain size increases from 20 μm to 75 μm. This is because that the high C_g gives rise to both high-density nuclei and sufficient source supply. Sufficient gaseous MoS_2 supply guarantees that the high-density nuclei can keep growing until the domains merge into continuous thin films. With the distance of 7 mm, the large domain size and high surface coverage MoS_2 thin films are grown. The average domain size of the crystalline MoS_2 is around 75 μm in the middle part and larger than 300 μm in the edge part. The low-density nuclei help to grow large domain size without comprising the surface coverage, which is attributed to the coincident match between the nuclei density and the source supply. Large-size MoS_2 flakes over 200 μm were reproducibly grown under this condition, as shown in Figure 2.4A to D.

In the range of relatively long distance (more than 7 mm), the surface coverage and average domain size both decrease with the increase of the distance. The low C_g results in low-density nuclei and

insufficient source supply for the surface precipitation. Without sufficient gaseous MoS_2 supply, the nuclei can grow independently during the growth procedure but fail to fully cover the surface. The insufficient MoS_2 supply leads to smaller size of domain. Interestingly, the nuclei density is expected to decline with the increase of the distance. However, a slight increase is presented in Figure 2.3B. After the abrupt decrease of nuclei density, the increased spare space for each nuclei growth prevent some nuclei from being absorbed by adjacent domains and allow them to grow to observable size, which gives rise to the increase of the nuclei density.

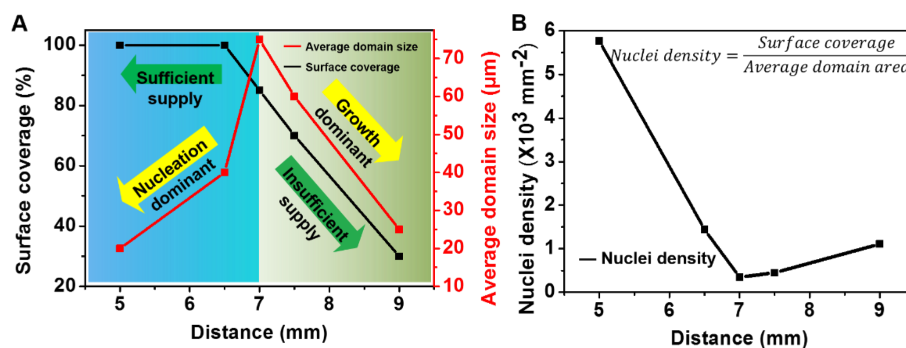

Figure 2.3 (A) Surface coverage and average domain size and (B) Nuclei density of the MoS_2 as a function of the source/substrate distance.

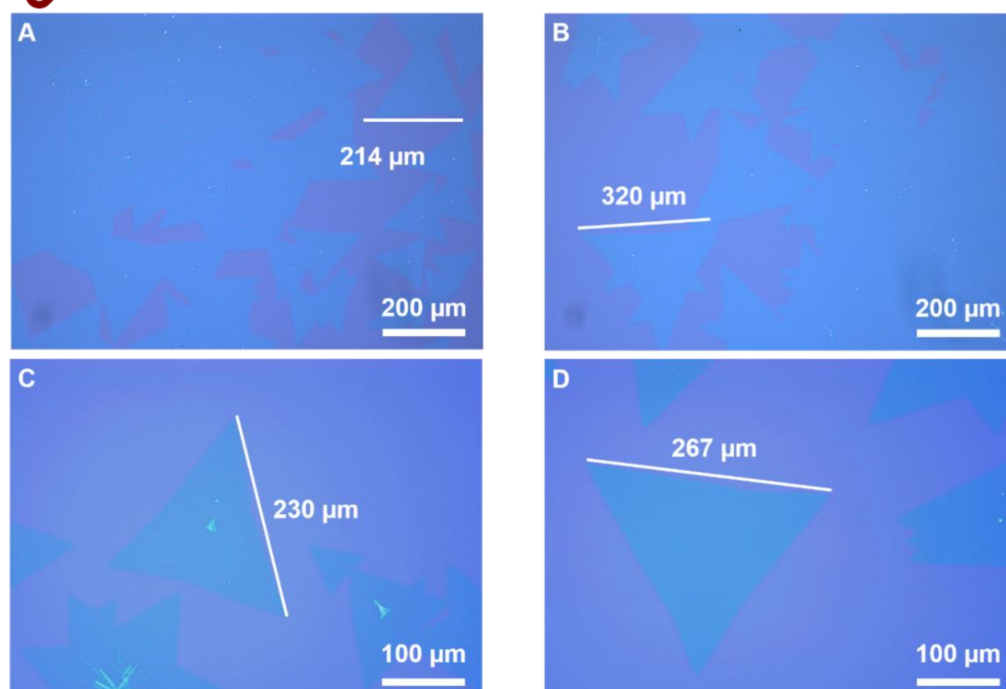

Figure 2.4 (A) to (D) Optical images of crystalline MoS_2 flakes with size lager than 200 μm.

We measured the thickness of MoS_2 films and flakes with Raman spectroscopy and atomic force microscope (AFM). Figure 2.5C shows the Raman spectra collected from the film and the flake in Figure 2.5A and B. The frequencies difference between the in-plane mode E^1_{2g} and the out-of-plane mode A_{1g} peaks was 20 cm^{-1} at P1 and P2 which represent MoS_2 films and flakes, respectively. This designates films and flakes are both monolayer.[111] The AFM images in Figure 2.6A and B further confirm that the thickness of the MoS_2 flake and film were ~ 0.8 nm and ~ 0.9 nm, which indicates monolayer MoS_2 and is consistent with previous reports.[35, 53] The domain boundaries of MoS_2 film (P3 in Figure 2.5A) are also investigated. The E^1_{2g} peak showed a

red shift while the A_{1g} peak presented a blue shift compared to the spectra of center of the film. The MoS_2 fails to remain monolayer near the boundaries region as the frequencies difference increased to 23 cm^{-1}. The AFM image in Figure 2.5D shows the boundary of two domains. A second layer of MoS_2 has been grown in the boundary region and part of MoS_2 was 3~4 layers, which is illustrated in the corresponding height profile in Figure 2.5E. The boundaries where two domains overlap offer extra nucleation point for MoS_2 growth. Rather than the flat MoS_2 films, it is easier to absorb atoms on the steps of the boundaries and begin to grow second layer MoS_2.

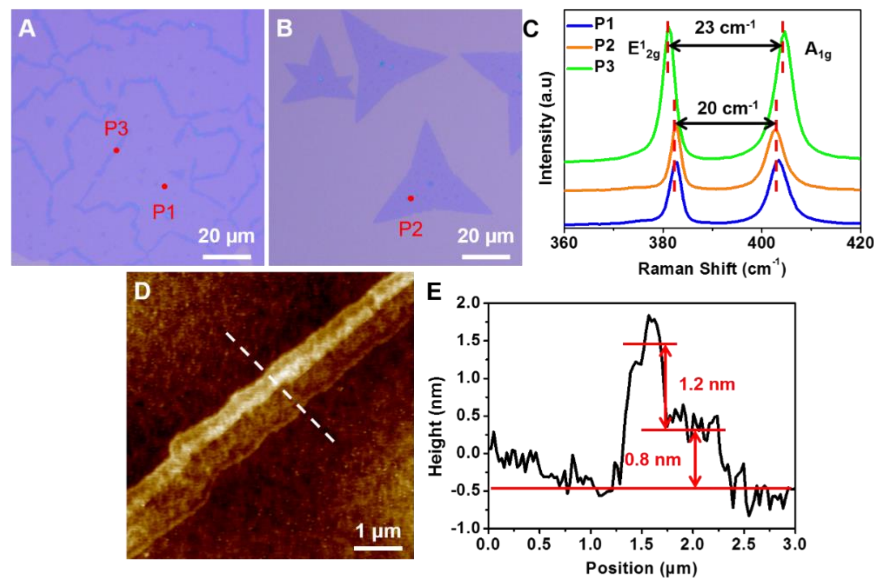

Figure 2.5 Optical images of the MoS_2 (A) thin film and (B) flake. (C) Raman spectra of the MoS_2 film, flake and boundary pointed in (A and B). (D) AFM images of MoS_2 domain boundary. (E) Height profiles taken across the dash line in (D).

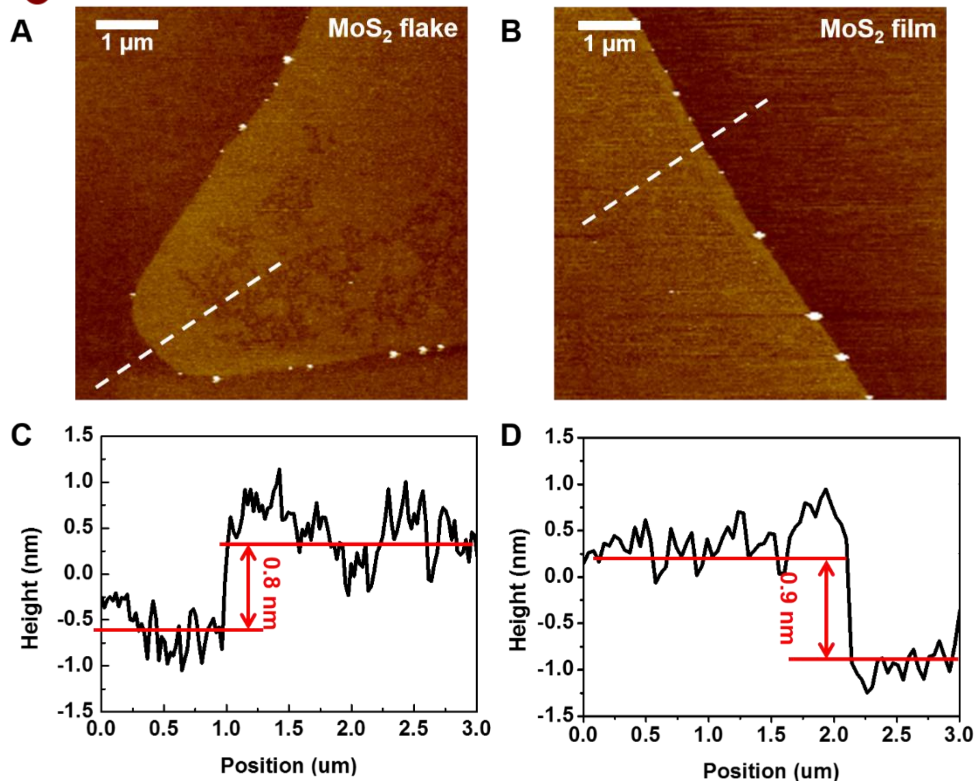

Figure 2.6 (A and B) AFM images of MoS_2 triangle flake and thin film. (C and D) Height profiles taken across the dash line in (A and B).

2.3.2 Resist-free transfer of MoS_2

To avoid the high-temperature growth process, we transfer crystalline MoS_2 flakes and thin films in this work. Figure 2.7 illustrates the schematics of the transfer process using thermal release tape (TRT). To prevent the direct contact between the MoS_2 surface and the glue, MoS_2 was first coated with a Cu thin film (~ 60 nm thickness) by thermal evaporation (Figure 2.7B). The TRT has a strong adhesion with the Cu thin film at room temperature, which helped to completely peel MoS_2 off from the growth substrate. The photograph in Figure 2.7D clearly shows that this transfer method is applicable to

centimeter-scale sample transfer. After the tape was pressed onto a target substrate, the substrate with the MoS_2/Cu/TRT was heated from room temperature to 120 ºC. The tape lost the adhesion and automatically peeled off (Figure 2.7E), leaving the MoS_2 and Cu thin film onto the target substrate (Figure 2.7F). The MoS_2 on the growth substrate (Figure 2.7A, 2 cm × 2 cm) was transferred onto a 3 cm × 3 cm SiO_2/Si substrate without notable changes (Figure 2.7G). We also transferred as-grown MoS_2 to SiO_2/Si substrates by conventional PMMA mediated method as control samples.

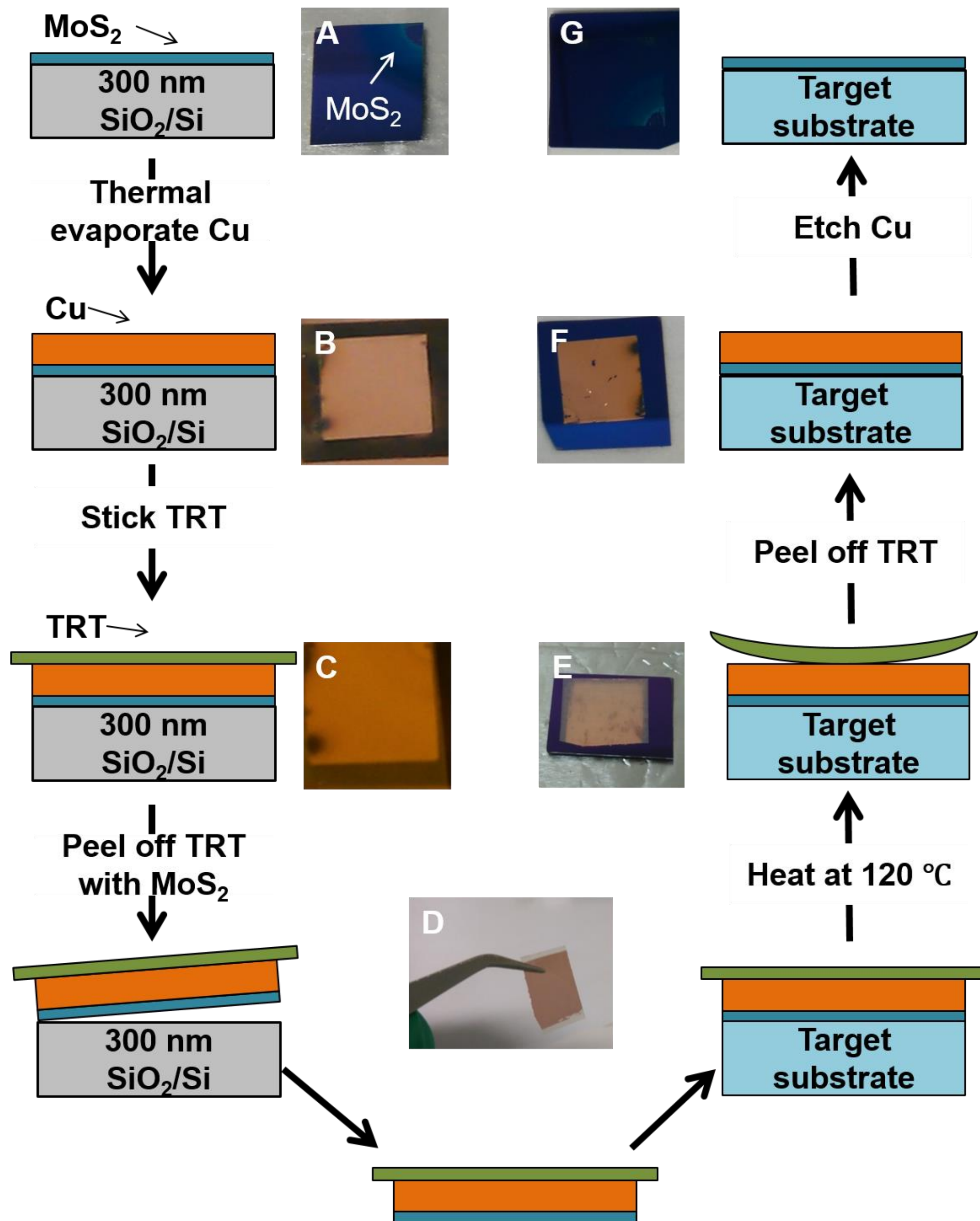

Figure 2.7 Illustration of the transfer process assisted with a Cu thin film. Photographs of the transfer processes: (A) as-grown MoS_2 on SiO_2/Si substrate; (B) coating the MoS_2 with a Cu thin film; (C) sticking TRT; (D) peeling off TRT together with MoS_2; (E) heating the target substrate to peel off TRT; (F) the MoS_2 and Cu thin film on the target substrate; (G) the transferred MoS_2 after Cu etching.

Figure 2.8A and B show the MoS_2 flakes before and after PMMA

transfer. Compared to the as-grown MoS_2, the PMMA-transferred MoS_2 presents remarkable resist residues although the sample has been cleaned with acetone for long time. It still remains a challenge to completely remove PMMA by acetone without additional cleaning process.[63] These resist residuals will degrade the performance of the electronic and optical devices based on MoS_2. In contrast, Figure 2.8C and D present the typical optical images of the as-grown and TRT transferred MoS_2 flakes, respectively. There is no significant difference between the as-grown and the TRT transferred samples. The surfaces of the samples were clean, indicating the absence of observable resist residues. It is further confirmed by the EDX result in Figure 2.9. The Cu thin film introduced between MoS_2 and TRT prevents the MoS_2 from directly exposing to the glue. Compared to polymer, Cu thin film is relatively easier to be etched, which has been widely adopted in industry.[59]

The SEM image in Figure 2.8E presents the evidence of generated wrinkles and resulting residuals on MoS_2 surface after the PMMA transfer. Figure 2.8F shows the SEM image of the TRT-transferred continuous MoS_2 thin film. The flat and uniform characteristics of the transferred thin film suggest that no wrinkles were generated during our transfer process. The Cu thin film with

comparable Young's modulus provides mechanically robust support for MoS_2 and reduces wrinkle generation during the transfer process. It also diminishes the strain induced when the TRT was peeled off during the temperature ramp process. On the contrary, PMMA has a low Young's modulus about 22 MPa,[112] far below that of monolayer MoS_2. This indicates that PMMA cannot provide sufficiently robust support for the MoS_2 during the transfer process. During the PMMA transfer process, the underlying SiO_2 layer was etched by KOH solution. Bubbles are generated in the etching process and can be trapped by the PMMA thin film, which will induce capillary force and give rise to wrinkles or even cracks (Figure 2.8I). Additionally, it is difficult to avoid the PMMA folding when we fish it out of the etching solution with target substrates. Compared with as-grown MoS_2 coated with PMMA (Figure 2.8H), there were observable wrinkles on the PMMA/MoS_2 film after transfer, shown in Figure 2.8J. However, in our technique, the Cu thin film and the TRT with robust support guarantee the flatness and integrality of MoS_2 during the transfer. AFM images in Figure 2.10 further confirm that our TRT-transferred technique allows us to transfer large-area monolayer MoS_2 residual-free and wrinkle-free.

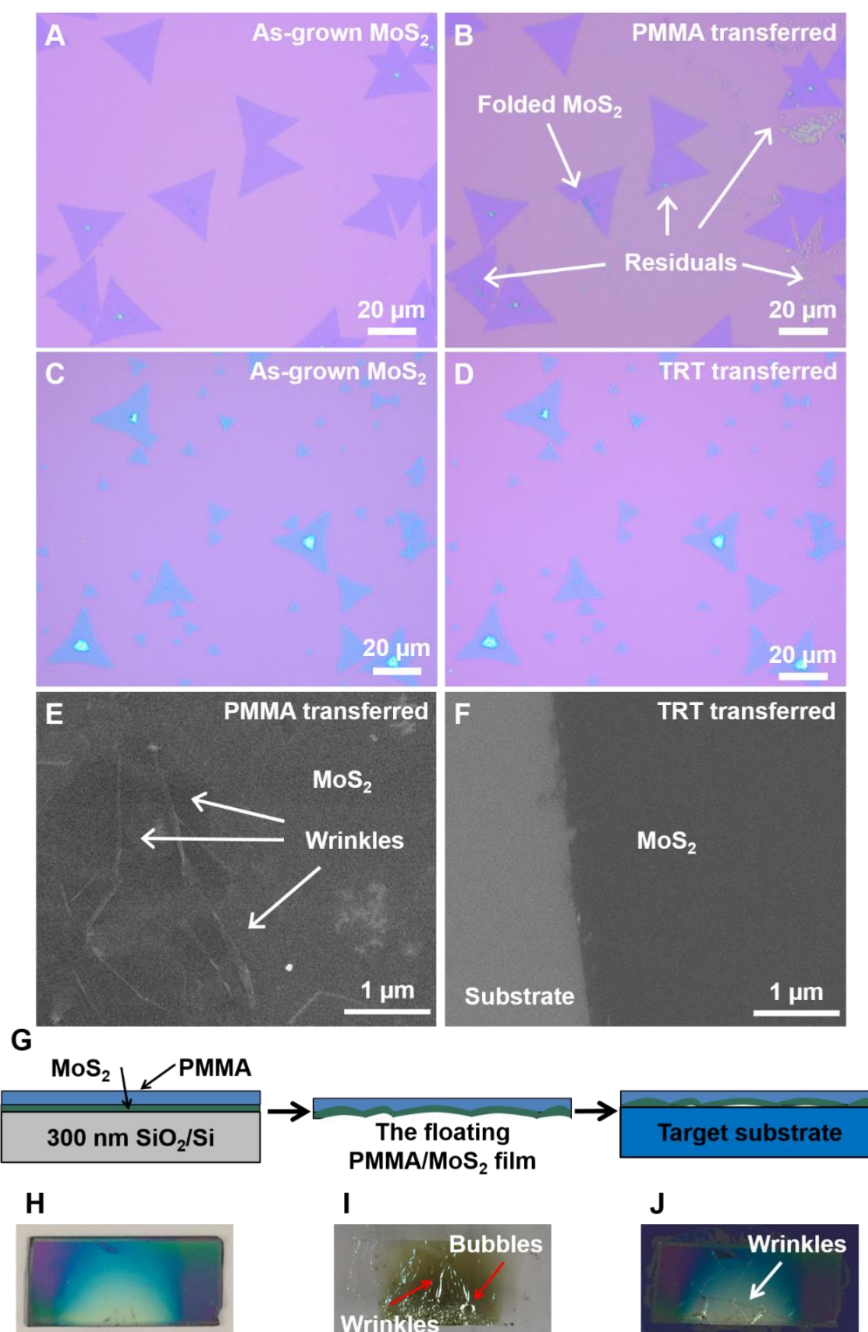

Figure 2.8 (A and B) Optical images of the MoS_2 before and after PMMA transfer. (C and D) Optical images of MoS_2 before and after TRT transfer. (E and F) SEM images of MoS_2 transferred by PMMA method and TRT method. (G to J) Schematic of wrinkle generation during PMMA transfer process and corresponding photographs.

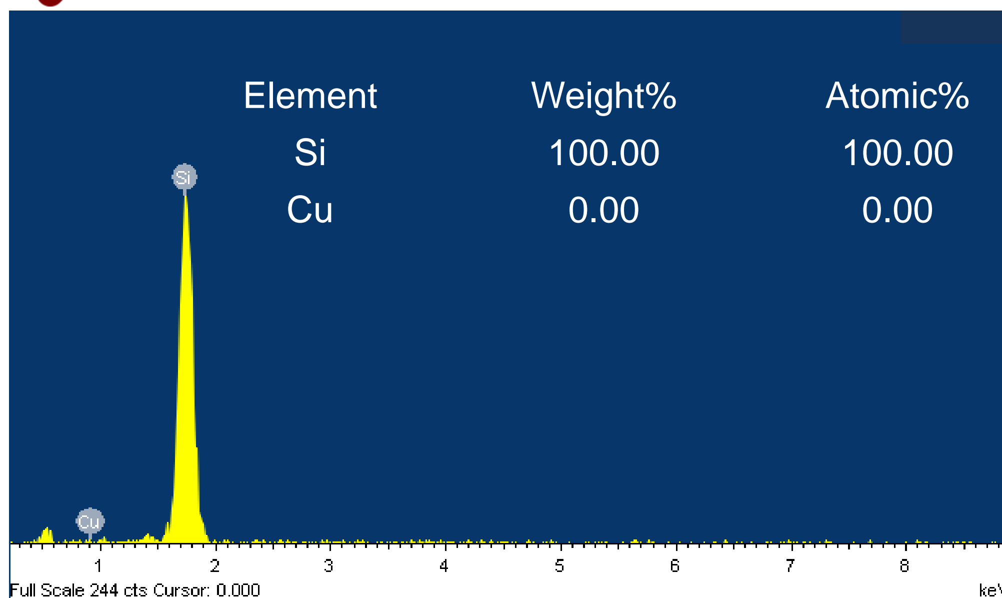

Figure 2.9 EDX spectra of the MoS_2 transferred by thermal release tape method with the element quantification results.

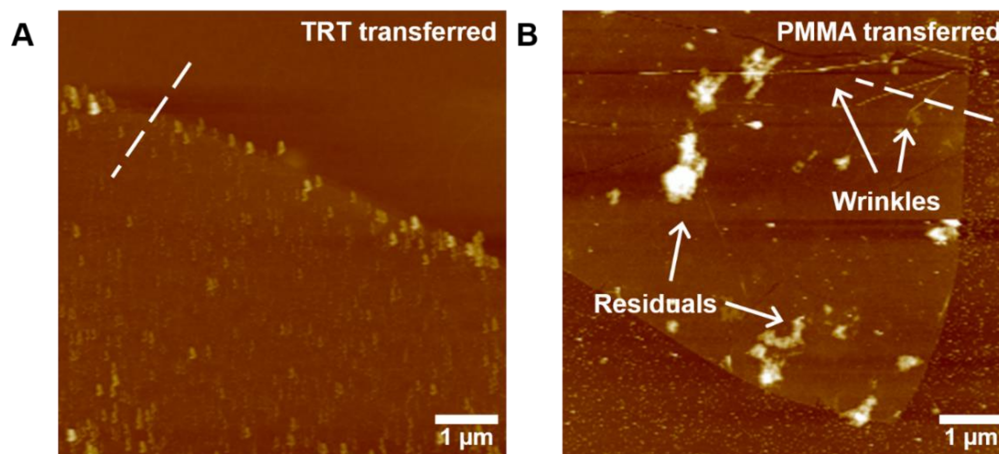

Figure 2.10 (A and B) AFM images of MoS_2 transferred by thermal release tape method and PMMA method.

Figure 2.11A shows the Raman spectra of the as-grown and transferred MoS_2. The frequencies difference between the in-plane mode E^1_{2g} and the out-of-plane mode A_{1g} peaks remained around 19~20 cm^{-1} after the transfer by PMMA and TRT methods, indicating that the layer number remains monolayer.[111] The peak position of the

in-plane mode E^1_{2g} in Raman spectra is sensitive to the strain and can be used as an indicator of the strain.[113] The peak position remains unchanged before and after the TRT transfer. However, this peak redly shifted about 2 cm^{-1} after the transfer by PMMA, which is induced by the wrinkle generated during the transfer.[114] This is also in agreement with our morphology characterization. The peak position of the out-plane mode A_{1g} is less affected by the strain.[113] Figure 2.11B shows the photoluminescence (PL) spectra of the MoS_2 samples. It can be seen that the principal PL peak showed no shift after our process but a redshift after the PMMA transfer, which can be explained by the influence of wrinkles, on top of which the strain accumulates.[114] This strain is introduced by the gap between Young's modulus of the thin film MoS_2 and the support (PMMA), which causes wrinkles lastly.[115]

The back-gate field-effect transistor (FET) based on the TRT-transferred MoS_2 was also fabricated. The transfer and output characteristic are shown in Figure 2.11C and D, respectively. The I_{ds}-V_{ds} curve shows the good contacts between the transferred MoS_2 and the electrodes, which also indicates the resist-free surface of TRT-transferred MoS_2.

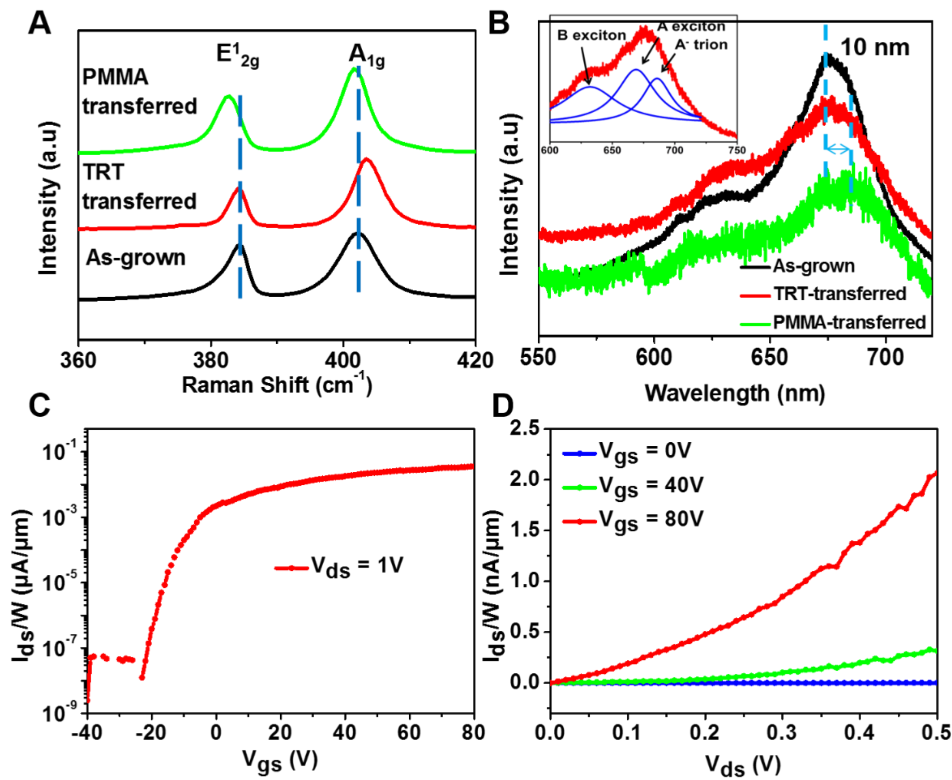

Figure 2.11 (A and B) Raman and Photoluminescence (PL) spectra of as-grown, TRT-transferred and PMMA-transferred MoS_2. (C and D) Transfer and output characteristic for the back-gate FET based on the TRT-transferred MoS_2.

2.4 Summary

We first investigated the morphology change of MoS_2 grown by our CVD method. Optical images presented that the ratio of MoS_2 triangular flakes and continuous films was influenced by the different placement of growth substrates. The underlying reason was the created MoO_3 concentration gradient by the change the distance between source and growth substrates. With sufficient MoO_3, adequate nuclei

generated, grew into triangular and merged into thin films. We also developed a transfer process involving TRT that can transfer MoS_2 onto arbitrary substrates without compromising the properties. The optical and SEM images confirmed the absence of observable residues and wrinkles on the transferred MoS_2. The properties were measured by Raman and PL, suggesting the transferred MoS_2 maintained qualities as the as-grown one. Although this work focused on the transfer of MoS_2, this process can be extended to the transfer of other two-dimensional layered materials.

Chapter 3 *in-situ* Observation on Growth Dynamics of Two-dimensional MoS_2 and MXene Flakes

3.1 Introduction

Technical advances of TEM (i.e. transmission electron microscope) in recent years have permitted an incomparable pathway towards the understanding of real-time processes at atomic scale.[116-117] Significant progresses have been made in figuring out the mechanisms behind sophisticated physicochemical processes using dedicated TEMs, such as the $CaCO_3$ nucleation, Pt_3Fe nanoparticles attachment, and Y_2BaCuO_5 nanowire growth.[118-120] Intriguingly, TEM observation concerning the growth of 2D materials beyond graphene remains rather limited, due to the critical challenge of obtaining images at atomic-resolution while maintaining the 2D materials grow in steps. Herein, in present study, we remedied this situation by using in-situ TEM to document the crystallization behavior of MoS_2 from a solid precursor upon controlled heating. We show that an interesting two-step growth mechanism is operative for growth of 2D structures from visualizing the growth trajectory of MoS_2 nanostructures.

In this chapter, we used a transmission electron microscope fitted with an advanced *in-situ* heating stage to uncover the growth mechanism of 2D MoS_2 and MXene flakes.

3.2 Methods

3.2.1 Sample preparation

For MoS_2 growth, high purity of $(NH_4)_2MoS_4$ was dissolved in dimethylformamide (DMF) to form a 1 wt. % solution, which was then sonicated for 10 min before use. For Mo_xC growth, 0.01 mol MoO_3 powder was added in 10 ml hydrogen peroxide (H_2O_2). The mixture was heated at 60 ºC until the MoO_3 completely dissolved in the H_2O_2.

3.2.2 TEM observation

The *in-situ* growth experiment described in this work was conducted on a Protochips AduroTM double-tilted platform using heating E-chip specimen support that provides atomic resolution at thermal ramping rate of up to 10^6 ºC/s with highly accurate temperature control of specimen inside a TEM. The TEM sample was prepared by drop-casting the above solution onto a Si_3N_4 membrane (for MoS_2 growth) or carbon membrane (for Mo_xC growth) supported by a silicon E-Chip, which was then dried in air. TEM observations

was conducted on a JEM-2100F field-emission transmission electron microscope operating at 200 kV, equipped with an Oxford INCA x-sight EDS Si(Li) detector. The sample was quickly heated to 100 ºC and stayed at this temperature for 15 min to remove any possible organic residuals before subsequent experiments. During the observations, the sample was irradiated by a focused electron beam with a constant current density (ca. 65 pA/cm^2), and the image was recorded by a Gatan SC1000 ORIUSTM CCD camera with a short exposure time (~ 1 s). The electron beam was blanked whenever possible to minimize beam effects on the sample.

3.2.3 Theoretical calculations

The density functional theory (DFT) calculations have been performed by using the Vienna ab initio simulation package (VASP) code[121-122] within projector augmented-wave (PAW) method.[123-124] General gradient approximations (GGA) in the Perdew-Burke-Ernzerhof (PBE) implementation[125] were chosen for the exchange correlation function. A plane-wave basis set expanded in energy with a cutoff of 400 eV is used in the calculation. The surfaces have been modeled by a symmetric slab containing eight Mo atom layers and a large vacuum of at least 15 Å. The corresponding sulfur layers are used in the calculation according to different termination

and surface orientation. To compare the stability of surfaces with different Miller index, we calculated their surface free energy following the approach developed by Reuter and Scheffler.[126] Taking hexagonal Si_3N_4 (space group P63) as an illustrative substrate, we also calculated the interfacial energy of both surfaces. The (2×1) MoS_2 (100) /Si_3N_4 (001) and (2×2) MoS_2 (001) /Si_3N_4 (001) structures are used to model the interfaces. And the corresponding interfacial energies are defined by $(E_{(A+B)}^{interface} - E_A^{surface} - E_B^{surface})/S$, in which E and S represent the total energy and area of different systems. To determine the relative stability of the particles with different orientations, the energy of MoS_2 particles relative to bulk MoS_2 is also evaluated. The (100) ((001)) and (010) index planes are supposed to expose at the side of the particle with (001) ((100)) orientation. The relative energy density per volume thus can be calculated by

$$\rho^{100(001)} = (lw(2\sigma^{100(001)} + \gamma^{100(001)}) + 2lh\sigma^{100(001)} + 2hw\sigma^{001(100)})/v$$

in which l, w, h and v mean length, width, height and volume of the particles, $\sigma^{100(001)}$ and $\gamma^{100(001)}$ represent surface energy and interfacial energy. Note that the miller index (100) ((001)) of MoS_2 particle used here corresponds to the vertical (horizontal) growth in article.

3.3 Results and discussion

3.3.1 Growth dynamic of MoS_2

3.3.1.1 Selected-area electron diffraction evolution

The ammonium thiomolybdates $(NH_4)_2MoS_4$ was adopted as our solid precursor and was introduced into a dedicated JEM-2100F transmission electron microscope, by using a protochips Aduro heating stage with a Si_3N_4 membrane as support (shown in Figure 3.1). It has been reported that the thermolysis of $(NH_4)_2MoS_4$ in an N_2 environment resulted in the production of MoS_2 via the following equations:[103, 127]

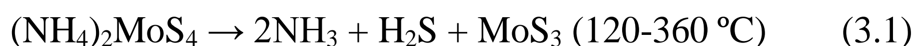
$$(NH_4)_2MoS_4 \rightarrow 2NH_3 + H_2S + MoS_3 \ (120\text{-}360\ ^{\circ}C) \qquad (3.1)$$

$$MoS_3 \rightarrow MoS_2 + S \ (> 800\ ^{\circ}C) \qquad (3.2)$$

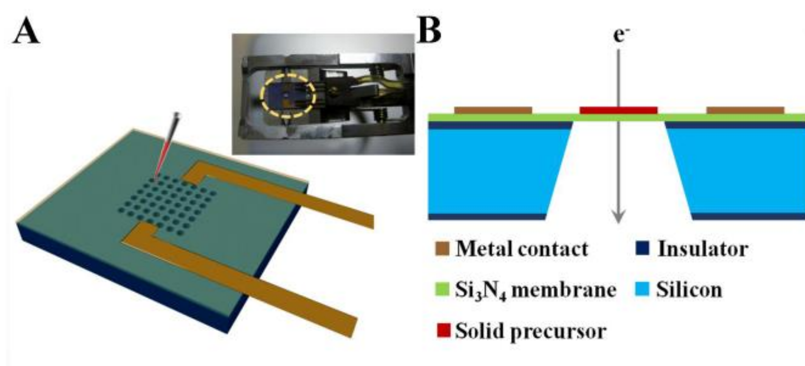

Figure 3.1 Schematic illustration of the experimental setup. (A) The preparation of heating E-chip with precursor, and the image of mounted Protochips Aduro heating stage (inset). (B) side-view of the as-prepared E-Chip.

To identify the thermolysis temperature of $(NH_4)_2MoS_4$ and crystallization process of MoS_2 in ultra-high vacuum (~ 10^{-5} Pa inside the TEM column), we first carried out the selected-area electron diffraction (SAED) survey over a wide temperature range, and the results were summarized as Figure 3.2. From room temperature to 400 ºC, the SAED pattern shown in Figure 3.2A indicates the precursor is kept at its amorphous state. When the temperature reached 400 ºC, blurred diffraction rings emerged (Figure 3.2B) and became shaper and brighter along with the rising temperature (Figure 3.2 C to E), indicating the improvement of crystallinity and the continuous size-development of crystallites. The SAED pattern in Figure 3.2E can be well indexed to hexagonal MoS_2 structure with a space group of P63/mmc. However, when the temperature continued to increase, considerable amount of impurities was observed in the SAED pattern at 900 ºC (shown in Figure 3.2G), which belongs to metallic Mo and results from the decomposition of MoS_2 at high temperature. Therefore, the crystallization of MoS_2 happened at 400 ~ 900 ºC in our experiment (in vacuum), which is of noticeable difference with above-mentioned results from inert gas environment.[127] It is also implied that MoS_2 crystals grow rapidly in size after 800 ºC while almost showed no change below 800 ºC, as the diffraction patterns

dramatically changed from uniform and continuous rings to discrete bright spots with increasing temperatures. The EDS spectra acquired at room temperature and 400 ℃ (Figure 3.3) further confirmed the complete conversion of $(NH_4)_2MoS_4$ to MoS_2 at 400 ℃, as indicated by the increased atomic ratio of Mo/S from 1/4 (in $(NH_4)_2MoS_4$) to 1/2 (in MoS_2).

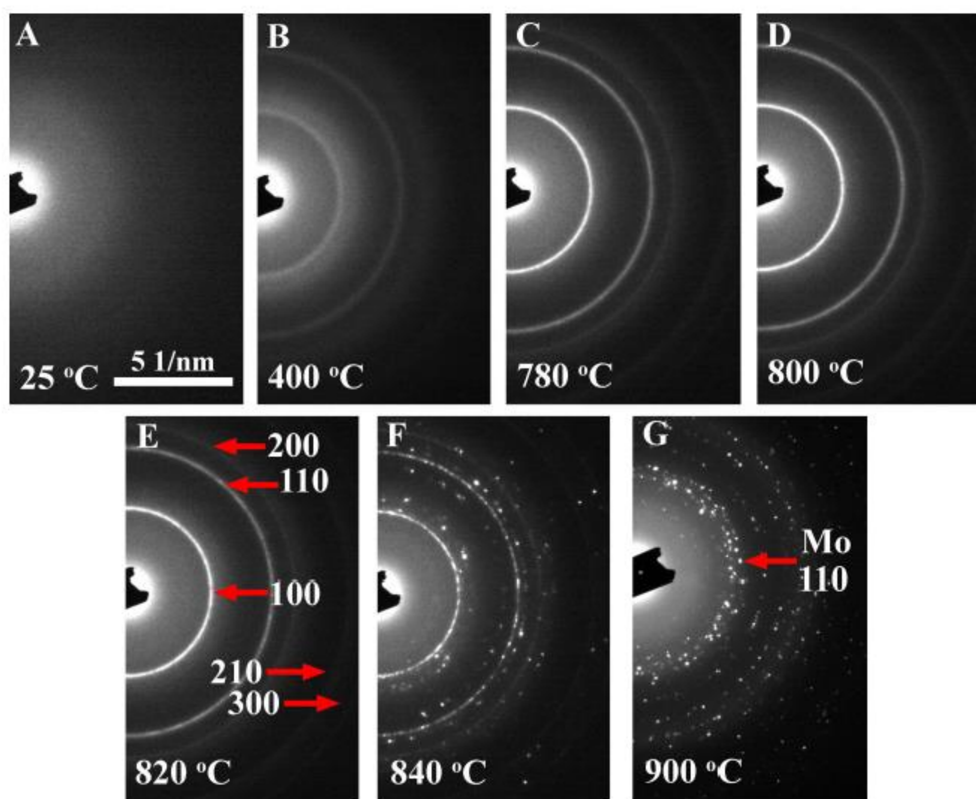

Figure 3.2 The evolution of SAED patterns across a wide temperature range. The scale bar in (A) also applies to (B - G).

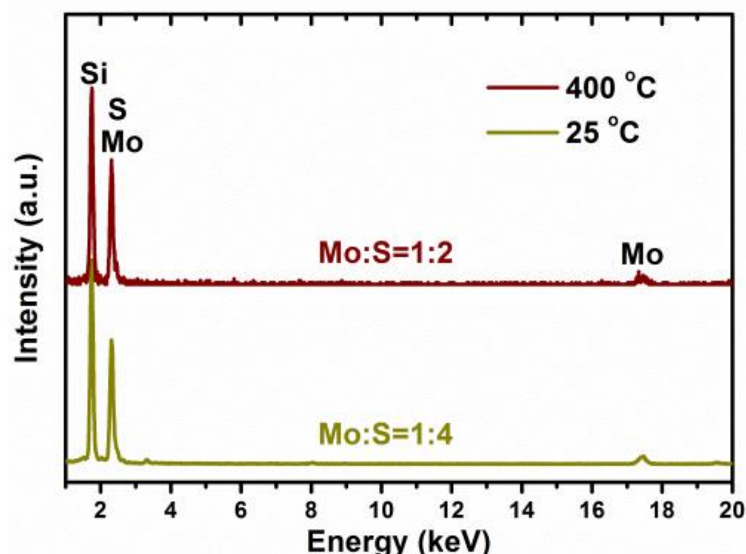

Figure 3.3 EDS spectra obtained at room temperature and 400 ºC, respectively.

3.3.1.2 Growth process of MoS_2

Systematical high-resolution TEM (HRTEM) micrographs were sequentially captured to analyze the crystallization and growth process of MoS_2 against increasing temperatures The remarkable intervals are presented in Figure 3.4. At 400 ºC, as shown on Figure 3.4A, the sample was found to be slightly crystallized into loosely packed, small clusters (1 - 3 nm) from the original amorphous precursor, with abundant 0.6 nm MoS_2 (002) planes exposed, which indicates the MoS_2 slabs adopt a vertical growth on the Si_3N_4 support at this stage. Although the surface energy of the edge sites ((002)-exposed) is reported to be larger than that of the terrace sites ((100)-exposed) by two orders of magnitude for MoS_2,[128] the vertical alignment of MoS_2 is

in accordance with the previous ex-situ observations on MoS_2 thin-film samples from sulfurization of Mo layers.[129-130] We further captured a movie to vividly describe the vertical growth dynamics of MoS_2 layers, and the snapshot frames are presented as Figure 3.5. At initial step, a new slab (forming from monomer attachment) partially covered on the existing cluster and then was developed to match the size of the underlying ones. It is clear that multi-layer MoS_2 structure forms in a layer-by-layer mode by homogeneous nucleation of additional layers onto old ones, and new layers preferably start from the step-edges of the old ones (see Figure 3.5B & D). Additionally, Figure 3.5 also suggest that formation of new layers is more energetically favorable than elongation of existed layers, as the MoS_2 cluster didn’t show obvious in-plane growth throughout Figure 3.5A – D.

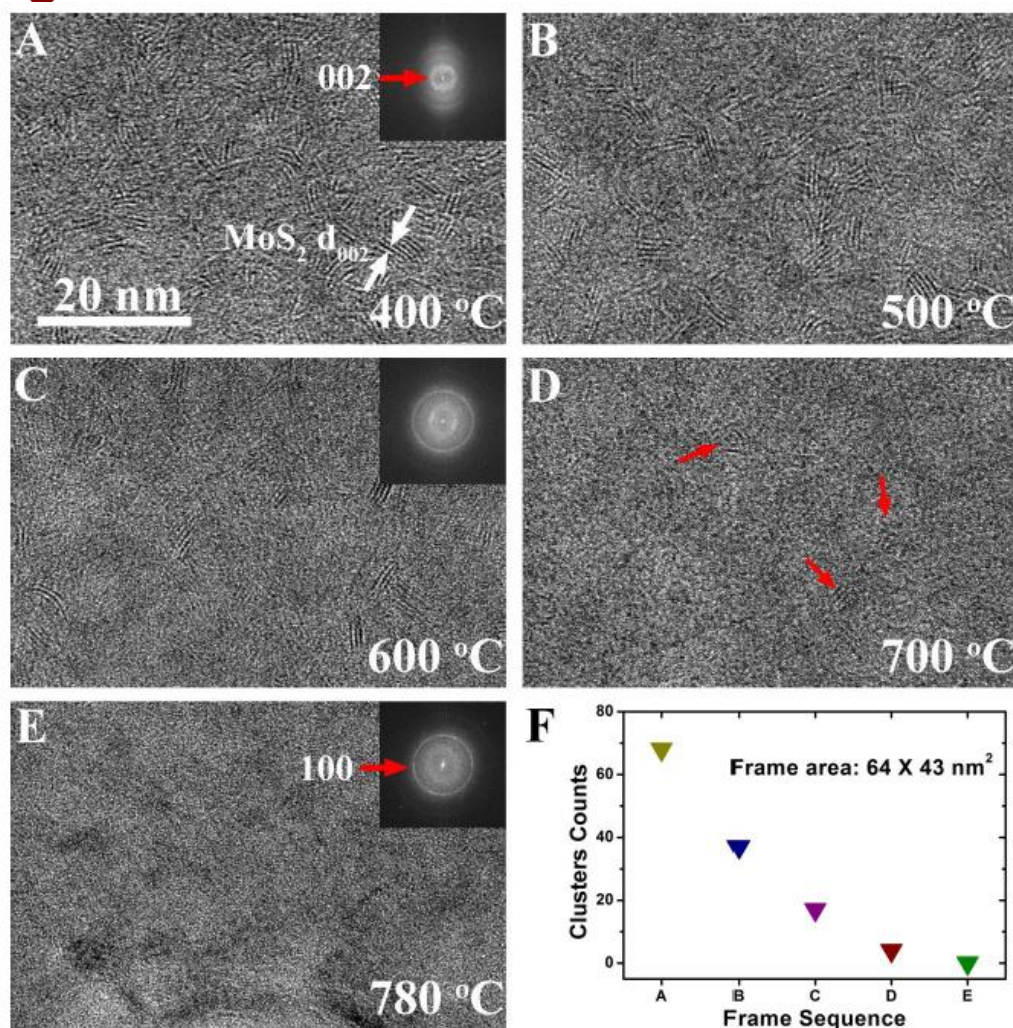

Figure 3.4 The growth dynamics of 2D MoS2 thin-film during heating to 780 ºC. (A - E) Image sequences showing the evolution from initial "(002)-exposed" structure to the later stage of "(100)-exposed" structure. The insets in (A), (C) and (E) are the corresponding FFT patterns, respectively. The red arrows in (D) denote the remaining clusters at 700 ºC. The scale bar in (A) also applies to (B - E). (F) Statistics of the clusters' counts in frames (A - E).

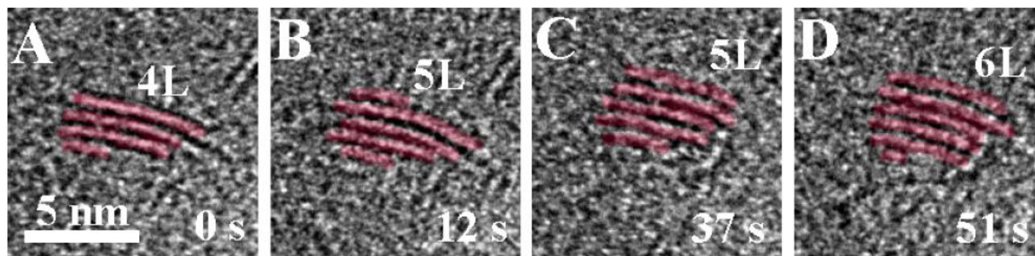

Figure 3.5 Time-resolved *in-situ* TEM micrograph series showing the layer growth trajectory at 400 ºC. 4L, 5L, and 6L stand for four-layer, five-layer, and six-layer MoS_2 structures, respectively. Colored sketches are included to identify the MoS_2 slabs. The scale bar in (A) also applies to (B - D). Time listed in all figures is relative to the beginning.

During further heating to 780 ºC, as displayed in Figure 3.4 (B – E), surprisingly, the exposed MoS_2 (002) planes gradually disappeared instead of getting larger. The insets in Figure 3.4A, C and E are their associated fast Fourier transform (FFT) patterns, showing a continuous brightness decrease of (002) halo ring while an inverse brightness increase of (100) halo ring, which implies the preferred orientation of MoS_2 on Si_3N_4 has been altered from (002)-oriented towards (100)-oriented. We need to mention here that the orientation of the MoS_2 slabs with respect to the electron beam has a determinative impact on the TEM contrast. The substantial image contrast of MoS_2 (002) basal plane can only be retained while it is ±9 degrees within the electron beam direction. Larger tilting angle will

lead to contrast weaken and the slabs become unrecognizable from the support substrates.[131-132] Therefore, it is reasonable to deduce that there is a "grain rotation" process at this stage; which is, the MoS_2 clusters have rotated from (002)-exposed to (100)-exposed during the heating between 400 °C to 780 °C. Of note, repeated observations at 780 °C have confirmed the formation of large-area polycrystalline MoS_2 (100)-exposed thin-films, matching well with previous CVD results from either gas-phase or solid-phase precursors at similar temperatures.[17]

Starting from 820 °C, MoS_2 particles began to precipitate as shown in Figure 3.6 and 3.7 (the red arrows in Figure 3.7A denote the precipitated MoS_2 crystals.). The MoS_2 crystals experienced a remarkable growth in size at higher temperatures (820 °C - 850 °C, Figure 3.6 & 3.7), which is ~ 3 nm at 820 °C, ~ 7 nm at 840 °C, and ~ 20 nm at 850 °C, respectively (presented in histograms of the change in particle size as a function of increasing temperature in Figure 3.6E), in line with the previous SAED analysis. Moreover, interesting size-growing dynamics was successfully recorded and presented in Figure 3.8. In Figure 3.8A, two isolated particles (I & II), both with exposed (103) planes but different orientations, contacted each other. After that, they both experienced obvious rotation of crystal

orientation to find a perfect lattice match and align their (103) planes (Figure 3.8B) before the disappearance of their contact interface (Figure 3.8C). Finally, as time lasted, the coalescence of particles I and II produced a new particle III with relaxed surface (Figure 3.8D). The process described above refers to typical oriented attachment (OA),[116, 133] which is an important mechanism for crystal growth in many materials, and differs a lot from classical crystal growth mechanism.[134] However, to the best of our knowledge, this is the first time that such a OA mechanism was in-situ observed in a two-dimensional MoS_2 system. Finally, when the temperature went to 850 ºC, the shape of the MoS_2 crystals experienced a dramatic change by facet development via mass redistribution. Majority of the MoS_2 crystals reshaped to closely packed, quasi-hexagonal nanoflakes with faceted outlines (see Figure 3.6D & 3.7C, the red arrows in Figure 3.6D denoted 120º angles), in good consistent with the CVD result using $(NH_4)_2MoS_4$ in dimethylformamide as gas-phase precursor.[135] The atomic-resolution HRTEM image in Figure 3.7C corresponds to highly crystalline nature of these nanoflakes, and the associated FFT pattern (inset in Figure 3.7C) displayed a typical six-fold symmetry expected for MoS_2 along its [001] direction.

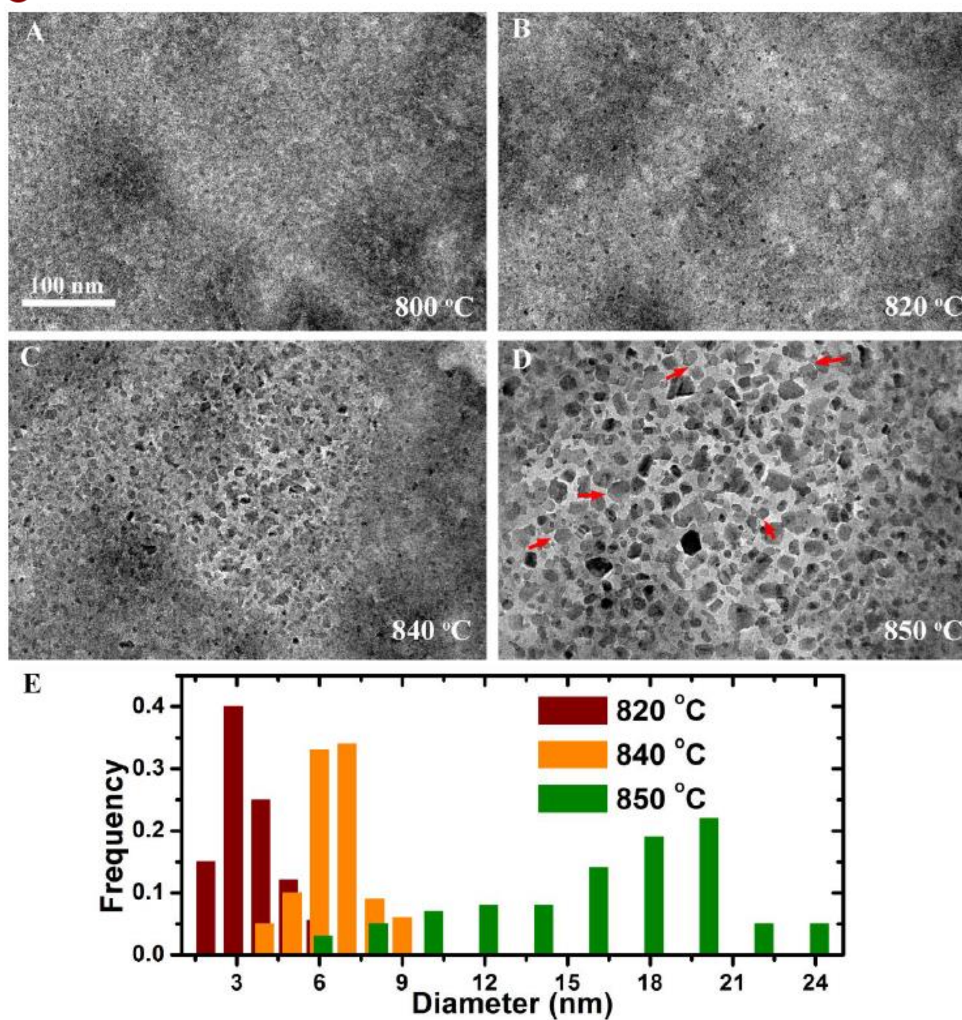

Figure 3.6 Precipitation and formation of 2D MoS_2 hexagonal nanoflakes during further heating beyond 800 ℃. (A - D) Typical image frames showing MoS_2 particle development versus rising temperature, in both size growth and reshape. The scale bar in (A) also applies to (B - D). (E) Statistics of the nanoparticle diameter as a function of heating temperature from (A - D).

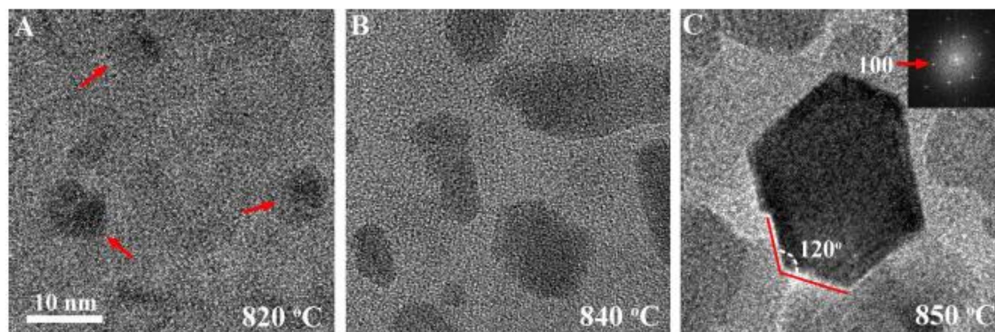

Figure 3.7 Sequential HRTEM images showing the structural transformation from irregular particles to faceted hexagonal nanoflakes. The inset in (C) is the corresponding FFT patterns. The scale bar in (A) also applies to (B - C).

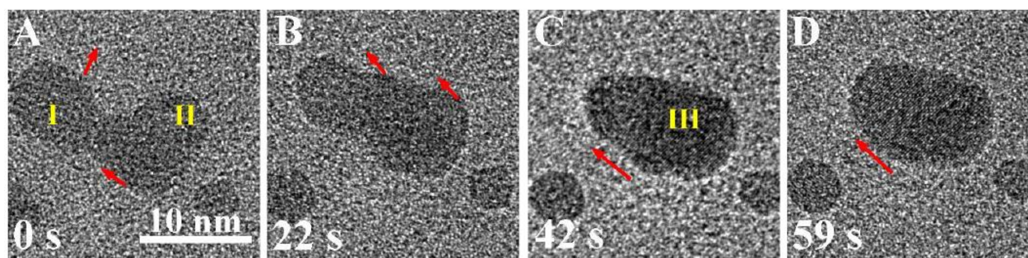

Figure 3.8 The details of the particle attachment process happened at 840 ºC (A - D) Sequences of in-situ TEM images indicating particle I and particle II merge into particle III. The red arrows denote [103] direction for the nearby particles. The scale bar in (A) also applies to (B - D). Time listed in all figures is relative to the first frame.

The complete mechanism concerning the MoS_2 growth from solid precursor at high temperature was thus extracted, and was sketched in Figure 3.9. The whole mechanism can be simply divided into two stages: the low-temperature thin-film stage (< 800 ºC, Figure 3.3) and the high-temperature nanocrystals stage (> 800 ºC, Figure

3.6). At low-temperature region, the MoS_2 growth generally includes the decomposition of solid precursor (other synthesis methods may not include this step), the formation of (002)-exposed films, and the successive grain-rotation towards large-area (100)-exposed films. Afterwards, at high-temperature region, MoS_2 nanocrystals would like to spontaneously precipitate from the thin-films, grow towards large crystals, and then develop to hexagonal nanoflakes. Although the lateral size of the final nanoflakes in our experiment is only among several tens of nanometers which is resulted from the limited transport ability of MoS_2 species in the all-solid environment, the revealed mechanism is of general applicability in other synthesis approaches (e.g. CVD method) leading to MoS_2 microsized flakes or even large-area thin-layers.

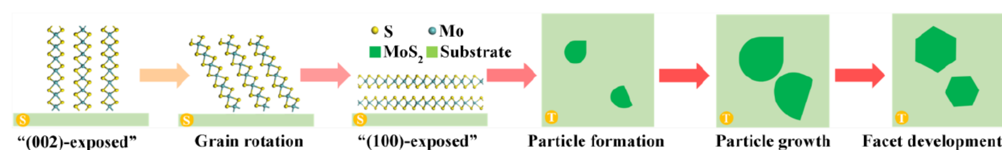

Figure 3.9 Schematic illustration of the structural evolution process during heating. "S" and "T" on orange discs stand for side-view and top-view, respectively.

3.3.1.3 Discussion

The initial formation of vertical-aligned layer structure and its

rotation to horizontal-aligned layer structure are driven by reducing total system energy and eliminating crystal defects. To demonstrate the decrease of total system energy during the transition, we performed the following calculations on the surface free energy during transition from (002)-exposed structure to (100)-exposed structure. As expected, the results indicate that the (001) surface has much lower surface energy (0.0277 eV/$Å^2$) than (100) surfaces in the rational chemical potential region. The sulfur terminated structure with surface energy of 0.1794 eV/ $Å^2$ is found to be the most stable termination in the surfaces with (100) Miller index. We also considered the interfacial energy at MoS_2/Si_3N_4 interface. Since the dangling bonds are present in (100) surface but absent in (001) surface, the distinct interfacial energies of these two surfaces are -0.1173 and -0.0046 eV/ $Å^2$. Clearly, the binding between MoS_2 (100) surface and the substrate is much stronger than MoS_2 (001).

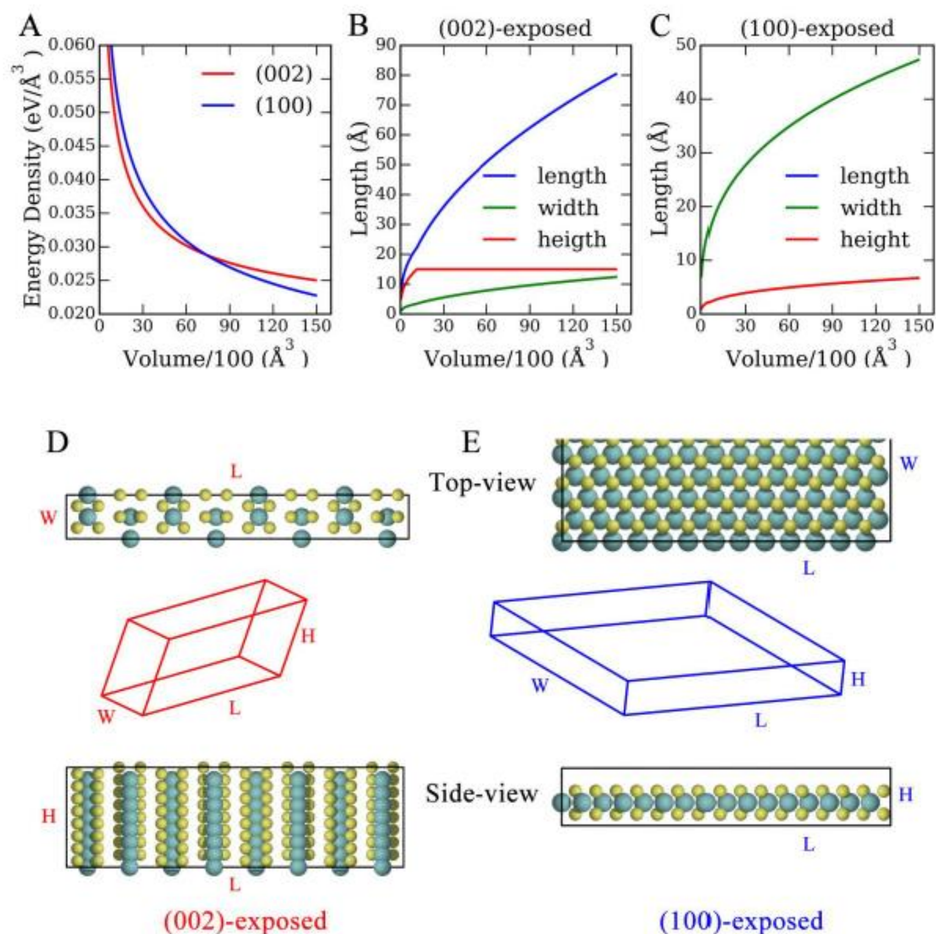

Figure 3.10 The competition of total system energy between (002)-exposed structure and (100)-exposed structure as a function of particle size during crystallization. (A) The energy density of particles along two orientations as a function of their volumes. The length, width and height of particles with minimal energy for (B) (002)-exposed and (C) (100)-exposed orientations. Note that the length is equal to width in the case of (100)-exposed orientations. (D) and (E) illustrate the shape and atomic arrangements for the particles along (002)-exposed and (100)-exposed orientations, respectively.

Generally, the interfacial energy will lower the energy of the

system while surface energy will raise it. Surface energy of (100) surface is larger than (001) but the interfacial energy is much smaller. Therefore, the competition of energy contribution from surface energy and interfacial energy in particles with different surfaces will determine the priority of growth orientation. To illustrate the idea, we evaluated the energies of particle in different orientations as a function of volumes. The corresponding energy density, the optimal length, width and height of different surface orientation as a function of volumes are summarized in Figure 3.10. We can find that the (002)-exposed particle prefers to adopt a box with large length and height but small width, whereas the (100)-exposed -MoS_2 particle trend to 2D growth mode, in which the length, equals to width, is much larger than height. As shown in Figure 3.10A, at the beginning of crystallization, the particle size is small, and hence (002)-exposed particle has lower energy than (100)-exposed one. When the volume is larger than the critical value, the (100)-exposed particle becomes more stable than (002)-exposed growth. This simplified thermodynamic mode on the basis of surface energy and interfacial energy from DFT calculation is in well consistent with the above experimental results, that a transition from (002)-exposed to (100)-exposed growth is happened during observation. It is worthy of noting that, although the

interfacial energy should be sensitive to substrates but the relative order will keep unchanged due to the dangling bonds in (100) surface.

Furthermore, defects may also play an important role in the aforementioned vertical-to-horizontal transition. At the initial stage (e.g., Figure 3.4A at 400 ºC), the twisty MoS_2 fringes in the HRTEM image imply the ample existence of in-plane defects (e.g. dislocations, localized disordering, and amorphization), resulting from a low degree of crystallization. These defects would further increase the (001) surface energy, on the basis of above computation. Upon this circumstance, the (002)-exposed structure will be more energetically stable than (100)-exposed structure. However, accompanied by the rising temperature (i.e., better crystallinity), the amount of defects would consequentially decrease (obviously, the lattice fringes are getting less twisty throughout Figure 3.3 A-D), leading to a synchronized decrease of (001) surface energy, and hence, a vertical-to-horizontal transition.

3.3.2 Growth dynamic of MXene

The MoO_3 in H_2O_2 solution was utilized as our precursor. It is reported that the MoO_3 can react with hot H_2O_2 solution and form H_2MoO_4, which will decompose to MoO_3 again at 400 ºC.[136] Different

from MoS_2 growth, the E-chip we used in the MXene growth is covered with carbon membrane, which serves as the support in TEM and the carbon source for MXene growth.

We first diluted the precursor solution and reduced the amount of MoO_3 introduced into TEM. Figure 3.11 A to D present the SAED evolution from room temperature to 1150 ºC. After excluding the diffraction ring of crystalline carbon film, we observe no diffraction pattern when the temperature was below 800 ºC, which indicates the precursor is kept at amorphous state. When the temperature continuously increased, a blurred diffraction rings emerged at 1000 ºC and became slightly sharper at 1150 ºC, which is indicated by the red arrow in Figure 3.11D. This pattern can be well indexed to the (100) surface of hcp Mo_2C. The intensity of this diffraction ring is even weaker than the adjacent diffraction ring of crystalline carbon film, which means the product Mo_2C has extremely low yield. The morphology image in Figure 3.11E confirm the low density of Mo_2C. Shown in Figure 3.11E, the domain size of Mo_2C flakes was in the range of 1 ~ 20 μm and some flakes displayed a typical six-fold symmetry. The HRTEM in Figure 3.11F provide details of a Mo_2C flake. The diffraction pattern in the inserted FFT also exhibits a six-fold symmetry and can be indexed by hcp Mo_2C phase, assuring

the final product. Figure 3.11 G and H show the beginning and the ending of the orientation attachment of two Mo_2C flakes. The exposure lattice is indicated by the red line. As presented, after the two flakes with two different orientations attached each other, the smaller flake rotated its orientation at a higher speed than that of the other flakes. Figure 3.11H shows the one flake combined with two flakes has a similar orientation with the larger one.

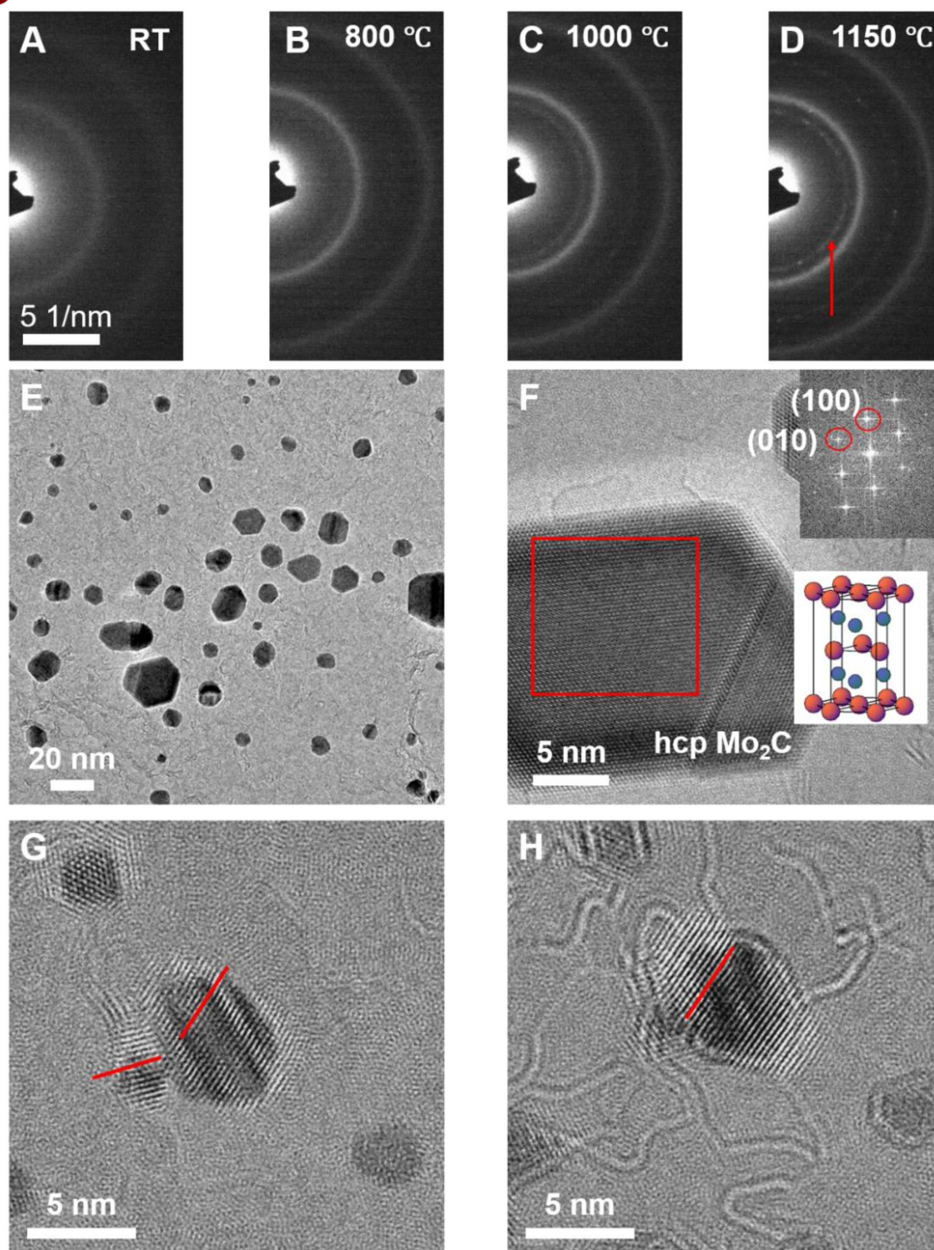

Figure 3.11 (A to D) The evolution of SAED patterns of high-concentration precursor across a wide temperature range. The scale bar in (A) also applies to (B - D). (E) Typical image showing the final product of Mo_2C flakes. (F) HRTEM showing one Mo_2C flake and the inserted is the FFT pattern. (G and H) The images showing the beginning and the ending of the Mo_2C attachment.

We attained Mo_2C with low concentration precursor. When we

increase the amount of MoO_3 introduced into TEM, the product was different. Figure 3.12 A to D present the SAED evolution from room temperature to 1150 ºC. Two significant diffraction rings emerged when the temperature was 800 ºC. These two rings can be indexed by the fcc cubic MoC (The Miller indices are indexed in Figure 3.12D). The diffraction rings were shaper and brighter along with the rising temperature, indicating the improvement of crystallinity and the continuous size-development of crystallites. From the morphology image in Figure 3.12E, the MoO_3 precursor exhausted the carbon support film. The MoC without underlying carbon film was free-standing supported by adjacent MoC. The MoC network has a size larger than 100 μm. However, large density of defects was observed in the HRTEM shown in Figure 3.12F. Figure 3.12 G and H can explain the reason for large amount of defects. When one MoC flake was attached to another one, it is expected to have an orientation match before combination. However, the large domain size and the strong interaction with the substrate hinder the rotation and require extra energy, which excess the energy for the formation of grain boundary and the followed recrystallization.

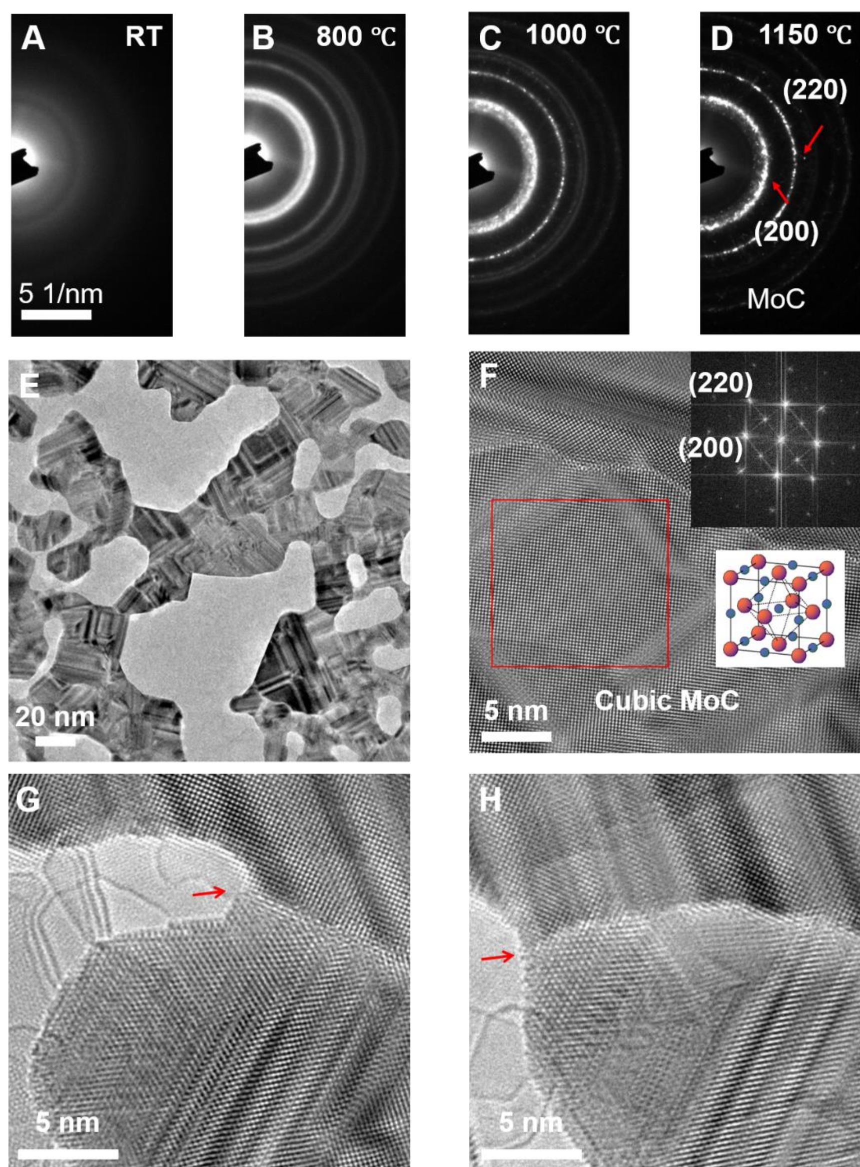

Figure 3.12 (A to D) The evolution of SAED patterns of low-concentration precursor across a wide temperature range. The scale bar in (A) also applies to (B - D). (E) Typical image showing the final product of MoC flakes. (F) HRTEM showing one MoC flake and the inserted is the FFT pattern. (G and H) The images showing the beginning and the ending of the MoC attachment.

To fully explain the different phases produced by different concentration precursor and different growth pathway, the formation

energy of Mo_xC phases and the system energy such as interfacial energy should be considered.

3.4 Summary

We have observed the dynamic growth of 2D MoS_2 structure on an amorphous substrate by using TEM upon heating a solid precursor. We have microscopically identified a novel two-step mechanism during the crystallization of MoS_2. A series of interesting phenomena, which include the initial formation of vertically aligned layers, then a grain rotation process towards a horizontally layered structure, precipitation and growth of nanocrystals, and formation of hexagonal MoS_2 nanoflakes after facet development, are recognized to present in the as-revealed mechanism. Such thorough understanding of 2D structure formation using *in-situ* TEM technique provides fundamental knowledge in synthesis of the emerging 2D materials and paves the way to rational design of nanostructures with proposed properties.

We further observed the Mo_xC growth which is highly dependent on the composite pf the precursor. We produced Mo_xC with different phases by adjusting the precursor concentration, which requires for further understanding.

Chapter 4 Two-dimensional Boron Nitride Nanosheet for Efficient Heat Dissipation of High Electron Mobility Transistors

4.1 Introduction

High electron mobility transistors(HEMTs) have been widely used for high-frequency and high-power communication applications.[90, 102, 137-138] AlGaN/GaN heterojuction device is one promising candidate of the HEMTs due to its large bandgap and high electron saturation velocity.[90] The power in the AlGaN/GaN HEMT can reach an extremely high density (approximately 19 W/mm) and lead to extensive self-heating in the device.[83-84, 88] The inefficient heat dissipation can result in elevated temperature in the devices, which simultaneously decreases the electron mobility, reduces the maximum drain current, degrades the RF performances, and adversely affects the reliability of the HEMTs.[85-86, 90] Efforts to decrease the thermal resistance between the devices and the ambient can help to spread the heat and reduce the temperature in the HEMTs. In commercial products, silicon carbide (SiC) and diamond substrates with higher thermal conductivity (K= ~350 $Wm^{-1}K^{-1}$ and ~1200 $Wm^{-1}K^{-1}$,

respectively) have replaced the conventional sapphire substrates (K= ~30 $Wm^{-1}K^{-1}$).[91] The flip-chip bonding is also utilized to reduce the thermal resistance.[139] These methods provide a solution for the thermal management of chip-level or package-level. However, the power dissipation in HEMTs is not uniform, which will induce the hotspots in the downscaled channels.[88] The chip-level and package-level thermal management fail to effectively dissipate the generated heat from non-uniform hotspots in a short time. To alleviate the problem of the hotspots, it is crucial to establish an efficient thermal management method at the micro/nanoscale.

Recently, the development of 2D materials with high thermal conductivity provides new ways to improve the thermal management of HEMTs. It has been reported that graphene has superior thermal conductivity: approximately 4000 $Wm^{-1}K^{-1}$ for single-layer and 1000-2000 $Wm^{-1}K^{-1}$ for few-layer, which suggests potential applications of graphene as thermal management materials.[75, 140-141] Zhong *et al.* demonstrated few-layer graphene (FLG) as heat spreaders and successfully reduced the temperature of hotspots in the high power transistors.[92] The superior in-plane thermal conductivity allows graphene effectively remove large heat flux from the hotspots. However, this thermal management with the FLG requires

exceptionally delicate control. The excellent electrical conductivity of FLG can give rise to short circuit, and cause the malfunction of the whole circuits with HEMTs.[94, 142] This feature requires additional photolithography steps to pattern graphene and complicates the processing for thermal management in the industry process. Therefore, the ideal materials for thermal management of integrated circuits (IC) are desired to be highly thermal-conducting but electrical-insulating. Two-dimensional h-BN, with a layered structure similar to graphene, has relatively high in-plane thermal conductivity (approximately 400 $Wm^{-1}K^{-1}$ for few-layer) but poor electrical conductance.[95, 143-145] Although the thermal conductivity of few-layer h-BN (FLBN) is relative lower than that of FLG, the electrical insulating facilitates the application of FLBN in thermal management of HEMTs or IC. Lin *et al.* demonstrated composites of h-BN platelet and polymer as encapsulates in IC for efficient heat dissipation.[146] Although large area FLBN can be grown by chemical vapor deposition (CVD) now,[147-149] limited study shows the application of FLBN for thermal management of ICs at micro-scale level.

In this chapter, we develop the local thermal management with FLBN as heat spreaders and bulk h-BN as heat sinks and investigate the effectiveness. The developed thermal management introduces an

additional heat transporting pathway from the hotspots to the ambient or the substrates.

4.2 Methods

4.2.1 Few-layer h-BN transfer.

The h-BN on the Cu foils were first spin-coated with PMMA (4% in anisole) thin films at 3000 r.p.m for 30 s and were baked at 110 °C for 10 min. The Cu substrates were then etched by ammonium persulphate solution. The attained PMMA films were transferred to the chips or other substrates and were baked at 110 °C for 30 min to improve the interaction between the h-BN and the substrates. Finally, after the removal of PMMA in acetone, the chips and other substrates with h-BN were prepared for further process and characterizations.

4.2.2 Characterizations methods.

Raman measurement was conducted using a Horiba Jobin Yvon LabRAM HR System with a laser wavelength of 488 nm. The laser spot size is ~ 1 μm with set power values (5.85 mW, 3.00 mW and 1.64 mW). The Raman spectra were collected by a 100X Olympus objective lens with acquisition time of 1000 s to distinguish weak h-BN Raman peak in the attained spectrum. The raw data were fitted

with Lorentz function. The DC performance of HEMTs were characterized using micromanipulator probe station 450PM-B with Keithley 4200-SCS semiconductor parameter analyzer while the RF performance were measured using network analyzer. The AFM images were taken by Bruker NanoScope and the SEM images were from Jeol field emission SEM.

4.2.3 Finite element simulation.

A finite-element model was used to investigate the temperature distribution of HEMTs with/without thermal management. The layers stack from bottom to top were Sapphire, GaN and AlGaN, with corresponding thickness of 300 μm, 500 nm and 30 nm and thermal conductivity of 30 $Wm^{-1}K^{-1}$, 160 $Wm^{-1}K^{-1}$, 120 $Wm^{-1}K^{-1}$. The electrodes were 240 nm thick with 317 $Wm^{-1}K^{-1}$ thermal conductivity. The heat source was placed in the middle of the channel, on the interface of GaN and AlGaN with 2 μm width. In the models with thermal management, there was a layer of FLBN film of 2 nm thick on the top surface. The thick h-BN was located at the electrodes or channels. The bottom, left and right boundaries of the model are kept at room temperature throughout the entire simulation. The top exterior of the model, is thermally isolated from its surroundings due to the fact that air has negligible thermal conductivity. The numerical

result was obtained by solving a set of linear solver using the above boundary conditions.

4.3 Results and discussion

4.3.1Thermal conductivity measurement

Raman thermometry has been widely used to characterize thermal properties of various nanomaterials, including carbon fibers,[150] graphene[5, 141, 151] and MoS_2.[152] The Raman signals of these nanomaterials are sensitive to the temperature and quantitatively respond to the temperature change. The peak information including frequency, full width at half maximum (FWHM) and intensity can indicate the temperature change of the materials.[153] The frequency-detecting method has the highest sensitivity and is most frequently employed in temperature measurement, while FWHM and intensity will be influenced by the focus level shift caused by thermal expansion effect and lost some sensitivity to temperature change. In this work, we mainly identified the temperature of FLBN through the Raman peak frequency of h-BN.

The relationship between the peak frequency and the temperature was first determined by carrying out a series of

temperature-dependent Raman spectra measurement. At room temperature, the in-plane E_{2g} phonon mode, the characteristic Raman peak of h-BN, is located at 1368.6 cm^{-1}, presented in the Figure 4.2A. Figure 4.1A shows the temperature-dependent Raman spectra of FLBN, ranging from 303 K to 393 K. The peak frequency exhibited a red-shift as the temperature increases, following similar trend as other materials (silicon, germanium and tin) reported in previous work.[154-155] The frequency shift marks the changed phonon energy affected by the temperature, which is primarily because of the thermal expansion of the lattice.[156] The shift can be described as a linear function between Raman frequency and temperature in the range near the room temperature.[5, 151-152] The function is presented in Figure 4.1B with a slope of -0.022 ± 0.003 $cm^{-1}K^{-1}$, which is referred as the first-order temperature coefficient.[157] When measuring the thermal conductivity, we first suspended the FLBN above the trenches with a depth of ~ 200 nm, which were fabricated by standard photolithography and inductively coupled plasma etching on 300 nm SiO_2/Si substrates. As shown in schematic figure in Figure 4.1C, the laser is focused on the suspended FLBN and increase the temperature in the sample. The temperature profile $T(r)$ within the suspended BN is governed by the following heat conduction equation:[158]

$$\kappa \frac{1}{r}\frac{d}{dr}[r\frac{dT(r)}{dr}] + q(r) = 0 \tag{4.1}$$

where κ is the thermal conductivity, r is radial distance from the center of laser, q(r) is the volumetric heating expressed as followed:

$$q(r) = \frac{PA}{\pi {r_0}^2 h}\exp(-\frac{r^2}{{r_0}^2}) \tag{4.2}$$

where *A* is absorbed fraction of heating power by the suspended BN, *h* is the thickness of the h-BN, r_0 and *P* are the radius and power of laser spot, respectively. After the temperature distribution *T(r)* is solved from equation (1), the average temperature within the suspended region is approximated as:[158]

$$T_m \approx \frac{\int_0^R T(r)exp\left(-\frac{r^2}{{r_0}^2}\right)rdr}{\int_0^R exp\left(-\frac{r^2}{{r_0}^2}\right)rdr} \tag{4.3}$$

where *R* is the size of the trenches. This local average temperature can be also determined from the temperature-dependent peak frequency of Raman spectra we attained in Figure 4.1B. Therefore, we can extract the thermal conductivity of FLBN using the below expression solved from above equations:[157]

$$\kappa = \frac{1}{2\pi h}\frac{\partial\omega/\partial T}{\partial\omega/\partial P}A \tag{4.4}$$

Figure 4.2B shows the absorption of FLBN at 488 nm light is about

0.03. It is noteworthy that most transmitted laser through the sample will be reflected from the bottom of the trenches. Thus, we assume that the absorbed fraction of laser power is 0.06 in the subsequent calculation. Figure 4.1D shows the function between the Raman frequency and the laser power. As expected, the frequency was red-shifted, while the laser power was increased from 1.64 mW to 5.85 mW. The relationship can be linearly fitted,[157] with a slope of -0.45 ± 0.01 $cm^{-1}mW^{-1}$. The thickness value was measured from AFM image and corresponding height profile presented in Figure 4.3A and B. According to equation (4), the thermal conductivity of FLBN is calculated to be 222.3 $Wm^{-1}K^{-1}$.

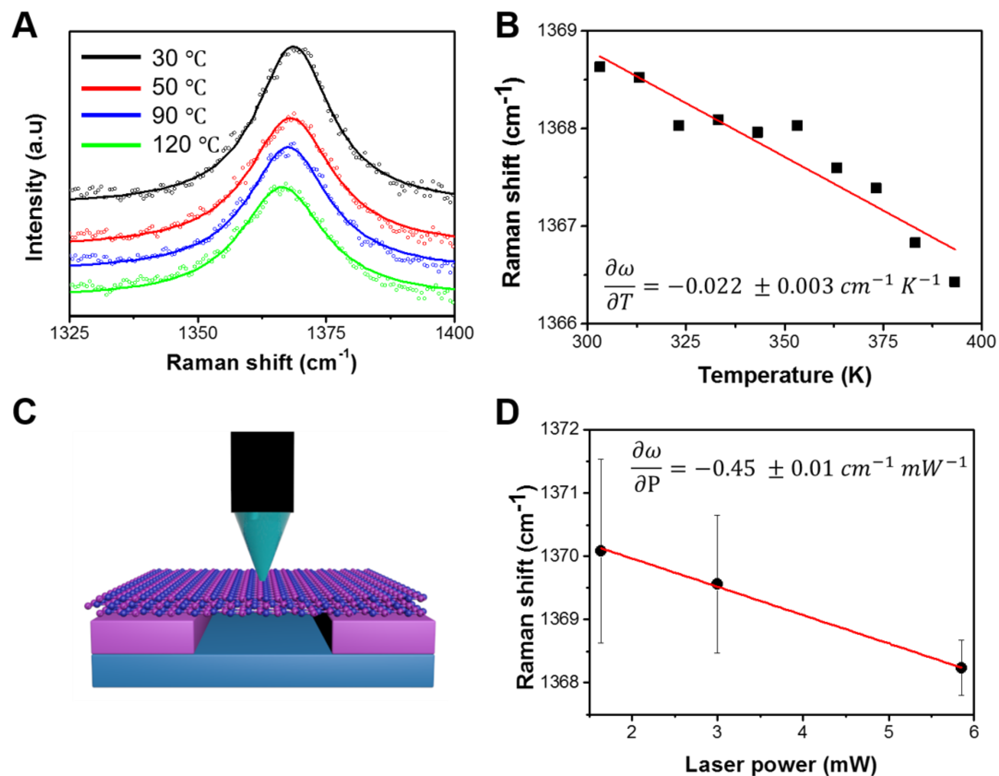

Figure 4.1 (A) Raman spectra of FLBN at different temperatures. (B) Relationship between Raman frequency of FLBN and the temperature. (C) Schematic of thermal conductivity measurement. (D) Relationship between Raman frequency of FLBN and the laser power.

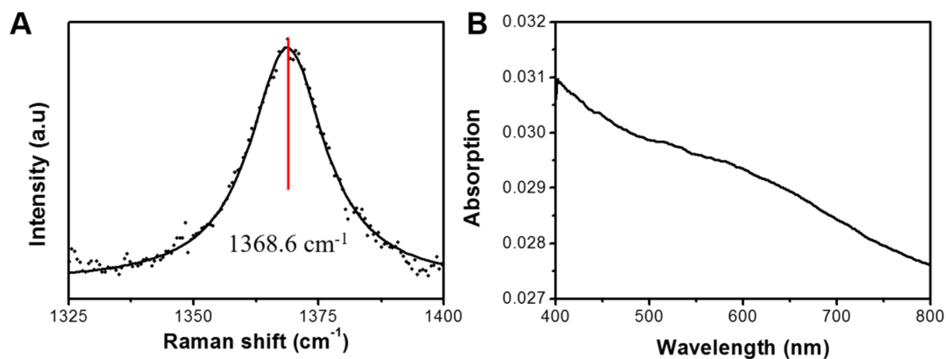

Figure 4.2 (A) Raman spectrum of FLBN at room temperature. (B) Absorption of FLBN at 400 nm to 800 nm wavelength.

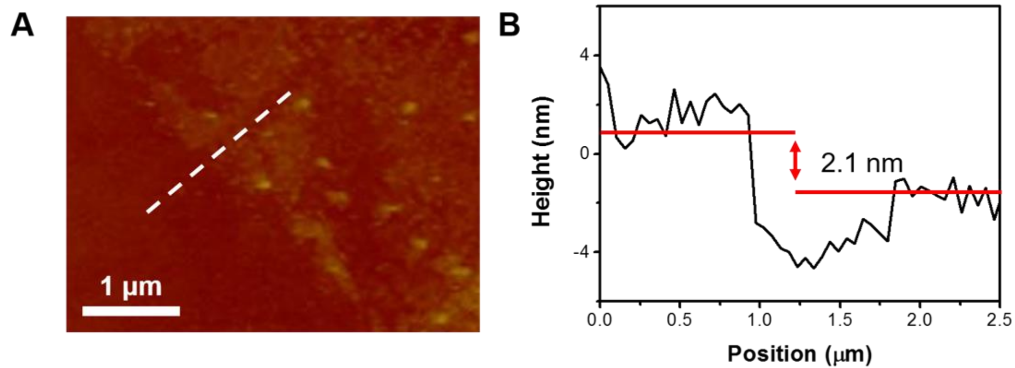

Figure 4.3 (A) and (B) AFM image of FLBN and corresponding height profile.

4.3.2 Device performances

Figure 4.4A is the optical image of the commercial HEMT showing the channel length is around 10 μm and the width is 100 μm. Previous simulation works have shown that the hotspots in the HEMT are located in the channel at the gate electrode edge near the drain side, where is indicated by the red line in Figure 4.4A.[88-89, 92] As schematically shown in Figure 4.4B, we first transferred the CVD-grown h-BN onto the power devices serving as heat spreaders. The liquid-exfoliated h-BN suspended in tripropylamine (TPA) solution was then dropped on the chip and formed thick h-BN as heat sink. The transferred FLBN with a modest thermal conductivity provide an additional pathway for thermal transport. The heat flux generated from the hotspots in the channel will be withdrawn to the thick h-BN, which can tolerate intensive heat flux from FLBN and dissipate to the ambient without affecting the devices. As h-BN is

highly electrical insulating, the h-BN can cover any part of the device without causing short circuit. Different from chip-level thermal management, our developed practice targets the heat dissipation at the microscale hotspots in the channel.

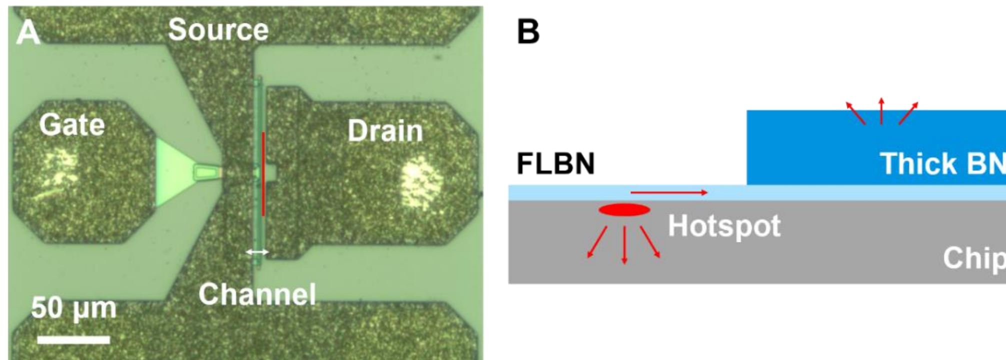

Figure 4.4 (A) Optical image of the HEMT on commercial chips. (B) Schematic of the developed thermal management.

The self-heating effect is a local temperature increase due to the high-density Joule electric power dissipated in the junction. When HEMTs are operated under high bias voltage, most of voltage drop occurs on the drain side, where large amount of heat is generated and hotspots are located.[89] The elevated temperature increases the phonon scattering, which can decrease the carrier mobility and give rise to negative differential output conductance (NDC). We first compared the DC performance of HEMTs with and without the use of h-BN. Figure 4.5A shows the transfer characteristics of the devices. As the devices were not operated at a high V_d when the transfer curves were

measured, the currents were unchanged. However, in the output curves shown in Figure 4.5B, the saturation current at different V_g all exhibited improvement with the use of h-BN for thermal management. The output curves of the HEMT with and without h-BN thermal management are also compared in Figure 4.5C. The saturation current was increased from ~ 0.077 A to ~ 0.080 A with h-BN thermal management. The onset voltage of NDC region was also advanced as the arrow indicates in the Figure 4.5C.

Without thermal management, the generated heat cannot be completely transport outside when the devices are operated at high power. The heat trapped in the channel increases the phonon scattering and degrades the DC performance. Our method provides an additional heat transporting pathway, which allows the channel dissipate the heat to the upper FLBN heat spreaders layer. The heat can be withdrawn to the thick h-BN and dissipated to the substrate or the ambient without effect to the channel. However, the heat flux dissipated by the FLBN is limited when the operation voltage is high. When measuring the output characteristic, we deliberately changed the voltage sweep rates. When the sweep rate is lower, the measure time will be increased, indicating more heat is generated from the channel. As shown in Figure 4.5D, the saturation current exhibited

3.3% to 4.5% improvement with h-BN thermal management regardless of measurement time. Although both conditions show current decrease when the measurement time was lengthened, the reduction rate of devices with thermal management was slower than that of devices without thermal management. The current improvement was increased when more heat was generated, indicating the significance of thermal management when devices are operated at high power in a long time.

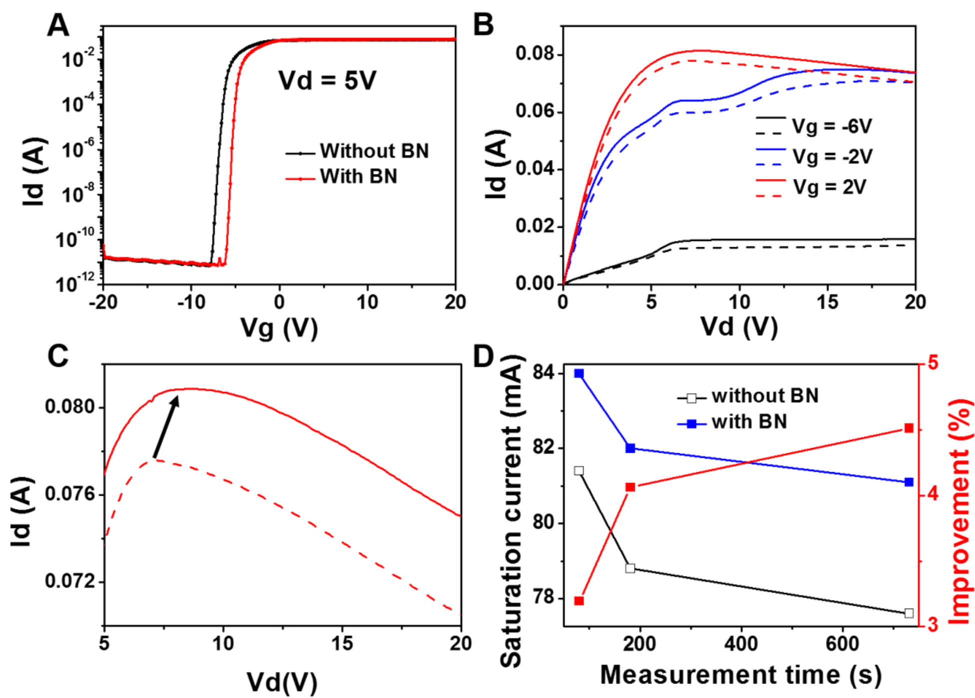

Figure 4.5 (A) Transfer characteristics of HEMTs with and without thermal management. (B) and (C) Output characteristics and detailed curve of HEMTs with (solid line) and without (dash line) thermal management. (D) Saturation current improvement of HEMTs with thermal management.

The effects of heat dissipation on the device performance can be also evaluated through the high-frequency characterization. It is reported that the elevated temperature induced by the hotspots will degrade the RF performance.[85-86] Figure 4.6 shows the Smith charts of S parameter from the device with and without h-BN heat spreader/sink. Figure 4.7A presents short circuit current gain $|h_{21}|$ of the HEMTs. The transit frequency f_T was increased by ~ 6% from 5.05 GHz to 5.86 GHz after the adoption of thermal management. Figure 4.7B shows the maximum available gain as a function of frequency. The maximum frequency of oscillation f_{max}, which can be extracted from Figure 4.7B, also increased from 13.13 GHz to 13.45 GHz. This indicates that the FLBN as thermal management helps to reduce the channel temperature and enhance the RF performance

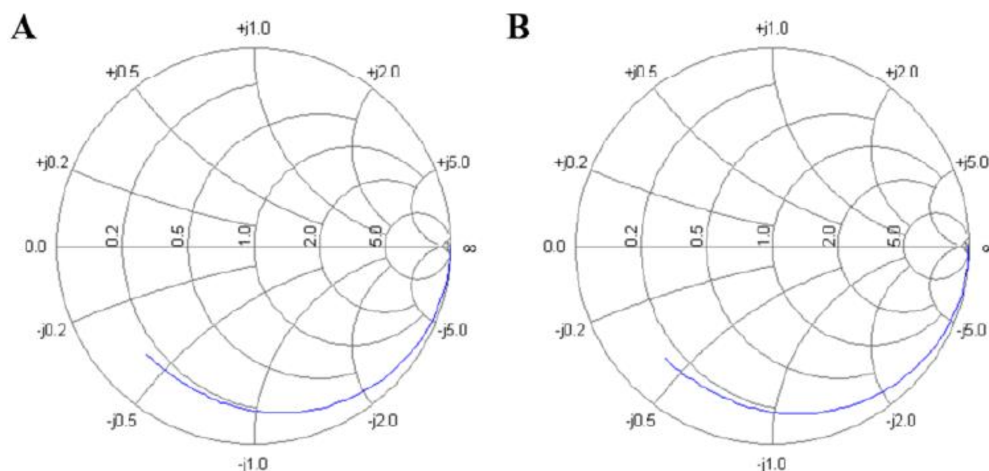

Figure 4.6 (A) and (B) Smith charts of HEMTs without and with thermal management.

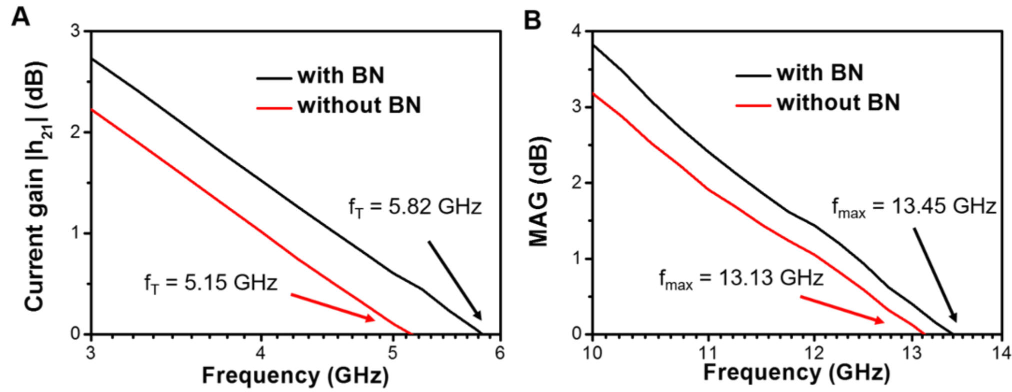

Figure 4.7 (A) and (B) Short circuit current gain and maximum available gain of HEMTs with and without thermal management.

4.3.3 Finite element simulation

The finite element simulation (see details in the Methods) was conducted to estimate the improvements in heat dissipation of HEMTs. The hotspot was assumed to be located within the channel, in agreement with previous works.[88-89, 92] Figure 4.8A shows the temperature distribution of a typical HEMT without thermal management on sapphire substrates with the power density of 4 W/mm. The maximum temperature reached ~ 185 °C at the hotspot. The heat flux generated from the hotspot is mainly dissipated to the bottom substrates. Sapphire is a conventional substrate for HEMTs, but with a low thermal conductivity (~30 $Wm^{-1}K^{-1}$). The inefficient heat dissipation is attributed to the high temperature in the channel, which consequently degrades the performance of HEMTs. Figure 4.8B and C

present the temperature profile of devices with two kinds of thermal management utilizing h-BN. In both simulations, FLBN served as the heat spreader dissipating the heat from the hotspot to other parts of the device. As FLBN is electrically insulating, it can cover the whole chip without causing short circuit and dissipate the heat in all directions. When the heat sink, thick h-BN, was located beyond the channel region and covered part of drain electrode as shown in Figure 4.8B, the maximum temperature was reduced by ~ 8 °C compared to devices without thermal management. The FLBN introduces an additional thermal transporting pathway allowing the heat at the hotspot spread to the rest part. Although FLBN can rapidly dissipate the heat form the hotspot, its heat capacity is poor considering its ultrathin thickness. Thick h-BN, serving as heat sinks, can tolerate intensive heat flux from FLBN and dissipate to the ambient without affecting the HEMTs. The h-BN heat sink can be replaced by the other commercial sinks or be connected to the bottom heat sinks in the geometry of thermal management in Figure 4.8B. Different from other heat sinks including graphite used in Zhong's work,[92] the h-BN heat sink can be even placed within the channel region without delicate fabrication. This will shorten the thermal transporting distance from FLBN to heat sinks. The maximum temperature was substantially decreased by 40 °C at the

hotspot of HEMTs with thermal management shown in Figure 4.8C.

The temperature reduction of devices operated at various power is summarized in Figure 4.8D. It is reasonable to see temperature increase when the devices were operated at higher power in all situations. The thermal management with both geometries shown in Figure 4.8B and C decreased the maximum temperature and alleviated the hotspot problems. The reduction was more significant when the thermal management has a h-BN heat sink at the channel. It benefits from the high electrical insulating h-BN which makes controlling the location of heat spreaders and sinks non-essential and facilitates the application in the industrial process.

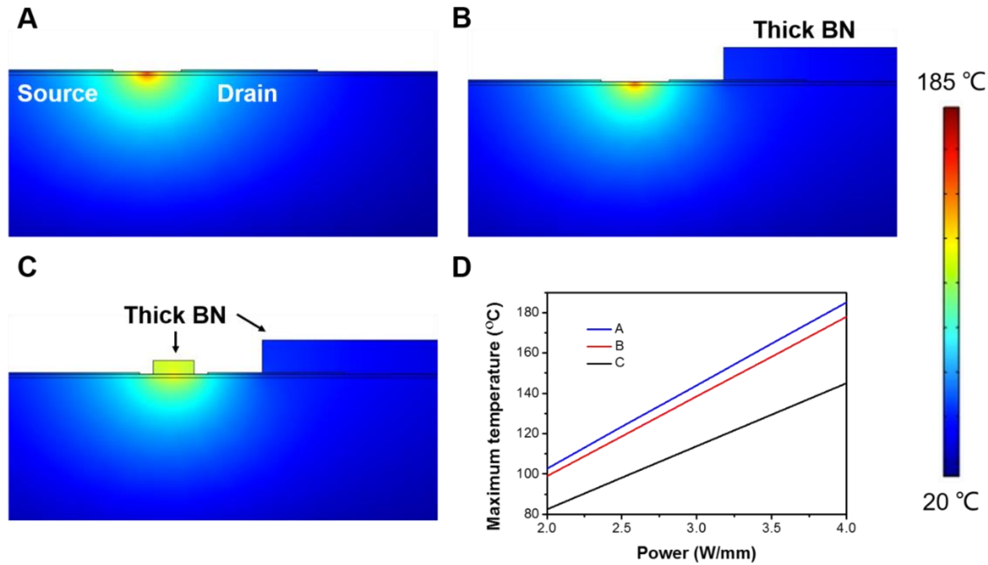

Figure 4.8 (A) Temperature distribution of HEMTs without the thermal management at the dissipated power 4 W/mm. (B) and (C) Temperature distribution of HEMTs with the thermal management (with different thick BN locations) at the dissipated power 4 W/mm. (D) Temperature reduction of HEMTs operated at different dissipated power.

4.4 Summary

In this chapter, we developed the thermal management at microscale utilizing FLBN as heat spreaders and thick h-BN as heat sinks, both of which are electrical insulating. Our Raman thermometry shows that the FLBN possesses high thermal conductivity of approximately 222.3 $Wm^{-1}K^{-1}$. The FLBN fully covered the device and rapidly dissipated the heat from the hotspot to other parts of the

device, while thick h-BN stored the intensive heat flux from FLBN and withdrew to the ambient without affecting the HEMTs. The electrical insulating h-BN simplifies the preparation process. With the developed thermal management, the performance of HEMTs in terms of DC and RF were enhanced. The finite element simulations indicates ~40 °C temperature reduction when the HEMT was assumed to be operated at 4 W/mm on sapphire substrates after the application of the thermal management. The developed heat dissipation is highly potentially applicable in thermal management of power devices and IC because of the characteristics of thermal-conducting and electrical-insulating of h-BN.

Chapter 5 Conclusions and Outlooks

5.1 Conclusions

In summary, we first grow MoS_2 using CVD method. By tuning the distance between source and growing substrate, we investigate the evolution of monolayer MoS_2 from triangle islands to continuous thin films. we then present a facile transfer process using thermal release tape (TRT) to avoid the polymeric residue and wrinkles generated in the PMMA-mediated transfer method. Our method allows us to transfer MoS_2 from the growing substrate onto arbitrary substrates without observable polymeric residues or wrinkles. We introduce a Cu thin film between monolayer MoS_2 and TRT, preventing the MoS_2 from direct exposure to the glue and giving rise to the resist-free MoS_2 surface. The tape and Cu thin film also provide mechanically robust supports for monolayer MoS_2 thin film, reducing the wrinkles generated during the transfer process. Without the resist residues and wrinkles, the transferred MoS_2 can maintain high quality compared to the as-grown samples. Although we focus on MoS_2 in this work, this technique can be extended to the transfer of other 2D layered TMD materials.

Secondly, we use *in-situ* transmission electron microscopy (TEM)

to track the crystallization trajectory of MoS_2 and MXene on an amorphous substrate. We first identify a novel two-step growth mechanism for MoS_2 growth, containing a low-temperature metastable thin-film stage and a successive high-temperature nanoflakes stage. The mechanism includes a sequence of intricate processes, which are the initial formation of vertically aligned layers, followed by a grain rotation process towards a horizontally layered structure before precipitation and growth of nanocrystals, and finally, formation of hexagonal MoS_2 nanoflakes after facet development. We then investigate the *in-situ* growth of Mo_xC. By adjusting the carbon concentration in the precursor, we attained MoC and Mo_2C in different phases. MoC with large domain size is grown in carbon-poor condition. The MoC flakes are enlarged by attachment to another flakes without orientation match. In contrast, Mo_2C is grown in carbon-rich condition. The carbon film surrounding the Mo_2C flakes hinder the diffusion of flakes. The flakes growth relies on the slow orientation attachment between flakes. The developed growth mechanisms shade light on the controllable growth of 2D materials.

Finally, we develop the local thermal management with few-layer h-BN as heat spreaders and bulk h-BN as heat sinks, which introduces an additional heat transporting pathway from the hotspots to the

ambient or the substrates. Our Raman thermometry characterizations show that the few-layer h-BN possesses high thermal conductivity, which allows to effectively spread the heat from hotspots and reduce the temperature in the channel. With the developed thermal management method, the maximum drain current of HEMTs is increased, and the transit frequency and maximum frequency of oscillation of HEMTs are improved. Our finite element simulations show that the temperature at the hotspots is reduced by ~40 °C at the power density of 4 W/mm by using h-BN heat spreader and heat sink. The improved thermal management targets the heat dissipation of non-uniform hotspots at device level, supplementing the chip-level and package-level thermal management for high-power device. The characteristics of thermal-conducting and electrical-insulating of h-BN make it more easily applicable in thermal management of power devices and IC.

5.2 Outlooks

Due to the unique structures and extraordinary properties, 2D materials have attracted intensive research interest. Even though the distinguishing properties, the feasible preparation methods and the practical applications have been extensively explored in recent years,

the research on 2D material is still on the early stage, especially for the new-emerging 2D material including MXene, BP, and silicene. Although the properties of these new-emerging 2D materials may have been studied, the preparation for these materials still remains a challenge, which subsequently limits the applications. 2D materials are a big family of unique materials. Except making the beat of the discovered materials, exploring for new 2D materials is more challenging and requires more research efforts. With many available 2D material, the fabrication of various kinds of 2D heterostructures with designed structures and desired properties also need further investigation.

This study investigated controllable growth of 2D MoS_2 and developed a microscopical understanding on the growth mechanism using *in-situ* TEM observation. The potential of *in-situ* TEM in research on growth mechanism of low-dimensional materials has been shown in this study. The mechanism developed from the nanoscale observation of growth behavior is of great importance on the controllable growth of 2D materials.

With intensive research efforts, 2D materials will be further developed and numerous promising applications will be proposed.

References

1. Novoselov, K. S.; Geim, A. K.; Morozov, S. V.; Jiang, D.; Zhang, Y.; Dubonos, S. V.; Grigorieva, I. V.; Firsov, A. A., Electric field effect in atomically thin carbon films. *Science* **2004,** *306* (5696), 666-669.

2. Allen, M. J.; Tung, V. C.; Kaner, R. B., Honeycomb carbon: a review of graphene. *Chemical Reviews* **2009,** *110* (1), 132-145.

3. Zhang, H., Ultrathin Two-Dimensional Nanomaterials. *ACS Nano* **2015,** *9* (10), 9451-9469.

4. Lee, C.; Wei, X.; Kysar, J. W.; Hone, J., Measurement of the elastic properties and intrinsic strength of monolayer graphene. *Science* **2008,** *321* (5887), 385-388.

5. Balandin, A. A.; Ghosh, S.; Bao, W.; Calizo, I.; Teweldebrhan, D.; Miao, F.; Lau, C. N., Superior thermal conductivity of single-layer graphene. *Nano Letters* **2008,** *8* (3), 902-907.

6. Bolotin, K. I.; Sikes, K.; Jiang, Z.; Klima, M.; Fudenberg, G.; Hone, J.; Kim, P.; Stormer, H., Ultrahigh electron mobility in suspended graphene. *Solid State Communications* **2008,** *146* (9), 351-355.

7. Novoselov, K.; Jiang, D.; Schedin, F.; Booth, T.; Khotkevich, V.; Morozov, S.; Geim, A., Two-dimensional atomic crystals. *Proceedings of the National Academy of Sciences of the United States of America* **2005,** *102* (30), 10451-10453.

8. Ferrari, A. C.; Bonaccorso, F.; Fal'Ko, V.; Novoselov, K. S.; Roche, S.; Bøggild, P.; Borini, S.; Koppens, F. H.; Palermo, V.; Pugno, N., Science and technology roadmap for graphene, related two-dimensional crystals, and hybrid systems. *Nanoscale* **2015,** *7* (11), 4598-4810.

9. Geim, A. K.; Novoselov, K. S., The rise of graphene. *Nature Materials* **2007,** *6* (3), 183-191.

10. Novoselov, K.; Geim, A. K.; Morozov, S.; Jiang, D.; Katsnelson, M.; Grigorieva, I.; Dubonos, S.; Firsov, A., Two-dimensional gas of massless Dirac fermions in graphene. *Nature* **2005,** *438* (7065), 197-200.

11. Schedin, F.; Geim, A.; Morozov, S.; Hill, E.; Blake, P.; Katsnelson, M.; Novoselov, K., Detection of individual gas molecules adsorbed on graphene. *Nature Materials* **2007,** *6* (9), 652-655.

12. Kim, K. S.; Zhao, Y.; Jang, H.; Lee, S. Y.; Kim, J. M.; Kim, K. S.; Ahn, J.-H.; Kim, P.; Choi, J.-Y.; Hong, B. H., Large-scale pattern growth of graphene films for stretchable transparent electrodes. *Nature* **2009,** *457* (7230), 706-710.

13. Li, X.; Cai, W.; An, J.; Kim, S.; Nah, J.; Yang, D.; Piner, R.; Velamakanni, A.; Jung, I.; Tutuc, E., Large-area synthesis of high-quality and uniform graphene films on copper foils. *Science* **2009,** *324* (5932), 1312-1314.

14. Bhaviripudi, S.; Jia, X.; Dresselhaus, M. S.; Kong, J., Role of kinetic factors in chemical vapor deposition synthesis of uniform large area graphene using copper catalyst. *Nano Letters* **2010,** *10* (10), 4128-4133.

15. Chang, J.; Zhou, G.; Christensen, E. R.; Heideman, R.; Chen, J., Graphene-based sensors for detection of heavy metals in water: a review. *Analytical and Bioanalytical Chemistry* **2014,** *406* (16), 3957-3975.

16. Lin, Y.; Williams, T. V.; Connell, J. W., Soluble, exfoliated hexagonal boron nitride nanosheets. *The Journal of Physical Chemistry Letters* **2009,** *1* (1), 277-283.

17. Chhowalla, M.; Shin, H. S.; Eda, G.; Li, L.-J.; Loh, K. P.; Zhang, H., The chemistry of two-dimensional layered transition metal dichalcogenide nanosheets. *Nature Chemistry* **2013,** *5* (4), 263-275.

18. Huang, X.; Zeng, Z.; Zhang, H., Metal dichalcogenide nanosheets: preparation, properties and applications. *Chemical Society Reviews* **2013,** *42* (5), 1934-1946.

19. Xu, M.; Liang, T.; Shi, M.; Chen, H., Graphene-like two-dimensional

materials. *Chemical Reviews* **2013,** *113* (5), 3766-3798.

20. Chhowalla, M.; Liu, Z.; Zhang, H., Two-dimensional transition metal dichalcogenide (TMD) nanosheets. *Chemical Society Reviews* **2015,** *44* (9), 2584-2586.

21. Peng, Y.; Li, Y.; Ban, Y.; Jin, H.; Jiao, W.; Liu, X.; Yang, W., Metal-organic framework nanosheets as building blocks for molecular sieving membranes. *Science* **2014,** *346* (6215), 1356-1359.

22. Colson, J. W.; Woll, A. R.; Mukherjee, A.; Levendorf, M. P.; Spitler, E. L.; Shields, V. B.; Spencer, M. G.; Park, J.; Dichtel, W. R., Oriented 2D covalent organic framework thin films on single-layer graphene. *Science* **2011,** *332* (6026), 228-231.

23. Naguib, M.; Mochalin, V. N.; Barsoum, M. W.; Gogotsi, Y., 25th Anniversary Article: MXenes: A New Family of Two-Dimensional Materials. *Advanced Materials* **2014,** *26* (7), 992-1005.

24. Wang, Q.; O'Hare, D., Recent advances in the synthesis and application of layered double hydroxide (LDH) nanosheets. *Chemical Reviews* **2012,** *112* (7), 4124-4155.

25. Osada, M.; Sasaki, T., Exfoliated oxide nanosheets: new solution to nanoelectronics. *Journal of Materials Chemistry* **2009,** *19* (17), 2503-2511.

26. Duan, H.; Yan, N.; Yu, R.; Chang, C.-R.; Zhou, G.; Hu, H.-S.; Rong, H.; Niu, Z.; Mao, J.; Asakura, H., Ultrathin rhodium nanosheets. *Nature Communications* **2014,** *5,* 3093.

27. Liu, H.; Du, Y.; Deng, Y.; Peide, D. Y., Semiconducting black phosphorus: synthesis, transport properties and electronic applications. *Chemical Society Reviews* **2015,** *44* (9), 2732-2743.

28. Radisavljevic, B.; Radenovic, A.; Brivio, J.; Giacometti, i. V.; Kis, A., Single-layer MoS_2 transistors. *Nature Nanotechnology* **2011,** *6* (3), 147-150.

29. Wang, Q. H.; Kalantar-Zadeh, K.; Kis, A.; Coleman, J. N.; Strano, M. S.,

Electronics and optoelectronics of two-dimensional transition metal dichalcogenides. *Nature Nanotechnology* **2012,** *7* (11), 699-712.

30. Sun, Y.; Gao, S.; Xie, Y., Atomically-thick two-dimensional crystals: electronic structure regulation and energy device construction. *Chemical Society Reviews* **2014,** *43* (2), 530-546.

31. Peng, X.; Peng, L.; Wu, C.; Xie, Y., Two dimensional nanomaterials for flexible supercapacitors. *Chemical Society Reviews* **2014,** *43* (10), 3303-3323.

32. Wu, S.; Zeng, Z.; He, Q.; Wang, Z.; Wang, S. J.; Du, Y.; Yin, Z.; Sun, X.; Chen, W.; Zhang, H., Electrochemically Reduced Single-Layer MoS_2 Nanosheets: Characterization, Properties, and Sensing Applications. *Small* **2012,** *8* (14), 2264-2270.

33. Ataca, C.; Sahin, H.; Ciraci, S., Stable, single-layer MX_2 transition-metal oxides and dichalcogenides in a honeycomb-like structure. *The Journal of Physical Chemistry C* **2012,** *116* (16), 8983-8999.

34. Fiori, G.; Bonaccorso, F.; Iannaccone, G.; Palacios, T.; Neumaier, D.; Seabaugh, A.; Banerjee, S. K.; Colombo, L., Electronics based on two-dimensional materials. *Nature Nanotechnology* **2014,** *9* (10), 768-79.

35. Ganatra, R.; Zhang, Q., Few-layer MoS_2: A promising layered semiconductor. *ACS nano* **2014**.

36. Yoon, Y.; Ganapathi, K.; Salahuddin, S., How good can monolayer MoS_2 transistors be. *Nano Letters* **2011,** *11* (9), 3768-3773.

37. Kaasbjerg, K.; Thygesen, K. S.; Jacobsen, K. W., Phonon-limited mobility in n-type single-layer MoS_2 from first principles. *Physical Review B* **2012,** *85* (11), 115317.

38. Ataca, C.; Şahin, H.; Ciraci, S., Stable, Single-Layer MX_2 Transition-metal oxides and dichalcogenides in a honeycomb-like structure. *The Journal of Physical Chemistry C* **2012,** *116* (16), 8983-8999.

39. Bertolazzi, S.; Brivio, J.; Kis, A., Stretching and breaking of ultrathin MoS_2.

ACS nano **2011,** *5* (12), 9703-9709.

40. Lee, H. S.; Min, S.-W.; Chang, Y.-G.; Park, M. K.; Nam, T.; Kim, H.; Kim, J. H.; Ryu, S.; Im, S., MoS_2 nanosheet phototransistors with thickness-modulated optical energy gap. *Nano Letters* **2012,** *12* (7), 3695-3700.

41. Zhang, E.; Wang, W.; Zhang, C.; Jin, Y.; Zhu, G.; Sun, Q.-Q.; Zhang, D. W.; Zhou, P.; Xiu, F., Tunable charge-trap memory based on few-layer MoS_2. *ACS nano* **2014,** *9* (1), 612-619.

42. Britnell, L.; Gorbachev, R.; Jalil, R.; Belle, B.; Schedin, F.; Mishchenko, A.; Georgiou, T.; Katsnelson, M.; Eaves, L.; Morozov, S., Field-effect tunneling transistor based on vertical graphene heterostructures. *Science* **2012,** *335* (6071), 947-950.

43. Sarkar, D.; Liu, W.; Xie, X.; Anselmo, A. C.; Mitragotri, S.; Banerjee, K., MoS_2 field-effect transistor for next-generation label-free biosensors. *ACS Nano* **2014,** *8* (4), 3992-4003.

44. Tsai, M. L.; Su, S. H.; Chang, J. K.; Tsai, D. S.; Chen, C. H.; Wu, C.I.; Li, L. J.; Chen, L. J.; He, J. H., Monolayer MoS_2 Heterojunction Solar Cells. *ACS nano* **2014,** *8* (8), 8317-8322.

45. Liu, H.; Peide, D. Y., Dual-gate MOSFET with atomic-layer-deposited as top-gate dielectric. *Electron Device Letters, IEEE* **2012,** *33* (4), 546-548.

46. Yin, Z.; Li, H.; Li, H.; Jiang, L.; Shi, Y.; Sun, Y.; Lu, G.; Zhang, Q.; Chen, X.; Zhang, H., Single-layer MoS_2 phototransistors. *ACS nano* **2011,** *6* (1), 74-80.

47. Splendiani, A.; Sun, L.; Zhang, Y.; Li, T.; Kim, J.; Chim, C. Y.; Galli, G.; Wang, F., Emerging photoluminescence in monolayer MoS_2. *Nano Letters* **2010,** *10* (4), 1271-5.

48. Mak, K. F.; Lee, C.; Hone, J.; Shan, J.; Heinz, T. F., Atomically thin MoS_2: a new direct-gap semiconductor. *Physical Review Letters* **2010,** *105* (13), 136805.

49. Shi, Y.; Li, H.; Li, L. J., Recent advances in controlled synthesis of

two-dimensional transition metal dichalcogenides via vapour deposition techniques. *Chemical Society Reviews* **2015,** *44* (9), 2744-56.

50. Zhan, Y.; Liu, Z.; Najmaei, S.; Ajayan, P. M.; Lou, J., Large-area vapor-phase growth and characterization of MoS_2 atomic layers on a SiO_2 substrate. *Small* **2012,** *8* (7), 966-71.

51. Lin, Y. C.; Zhang, W.; Huang, J. K.; Liu, K. K.; Lee, Y. H.; Liang, C. T.; Chu, C. W.; Li, L. J., Wafer-scale MoS_2 thin layers prepared by MoO_3 sulfurization. *Nanoscale* **2012,** *4* (20), 6637-41.

52. Lee, Y. H.; Zhang, X. Q.; Zhang, W.; Chang, M. T.; Lin, C. T.; Chang, K. D.; Yu, Y. C.; Wang, J. T.; Chang, C. S.; Li, L. J.; Lin, T. W., Synthesis of large-area MoS_2 atomic layers with chemical vapor deposition. *Advanced Materials* **2012,** *24* (17), 2320-5.

53. Najmaei, S.; Liu, Z.; Zhou, W.; Zou, X.; Shi, G.; Lei, S.; Yakobson, B. I.; Idrobo, J. C.; Ajayan, P. M.; Lou, J., Vapour phase growth and grain boundary structure of molybdenum disulphide atomic layers. *Nature Materials* **2013,** *12* (8), 754-9.

54. van der Zande, A. M.; Huang, P. Y.; Chenet, D. A.; Berkelbach, T. C.; You, Y.; Lee, G. H.; Heinz, T. F.; Reichman, D. R.; Muller, D. A.; Hone, J. C., Grains and grain boundaries in highly crystalline monolayer molybdenum disulphide. *Nature Materials* **2013,** *12* (6), 554-61.

55. Yu, Y.; Li, C.; Liu, Y.; Su, L.; Zhang, Y.; Cao, L., Controlled scalable synthesis of uniform, high-quality monolayer and few-layer MoS_2 films. *Scientific Reports* **2013,** *3*, 1866.

56. Ji, Q.; Zhang, Y.; Zhang, Y.; Liu, Z., Chemical vapour deposition of group-VIB metal dichalcogenide monolayers: engineered substrates from amorphous to single crystalline. *Chemical Society Reviews* **2015,** *44* (9), 2587-602.

57. Wu, S.; Huang, C.; Aivazian, G.; Ross, J. S.; Cobden, D. H.; Xu, X.,

Vapor–solid growth of high optical quality MoS_2 monolayers with near-unity valley polarization. *ACS Nano* **2013,** *7* (3), 2768-2772.

58. Deokar, G.; Avila, J.; Razado-Colambo, I.; Codron, J.-L.; Boyaval, C.; Galopin, E.; Asensio, M.-C.; Vignaud, D., Towards high quality CVD graphene growth and transfer. *Carbon* **2015,** *89*, 82-92.

59. Liang, X.; Sperling, B. A.; Calizo, I.; Cheng, G.; Hacker, C. A.; Zhang, Q.; Obeng, Y.; Yan, K.; Peng, H.; Li, Q., Toward clean and crackless transfer of graphene. *ACS nano* **2011,** *5* (11), 9144-9153.

60. Caldwell, J. D.; Anderson, T. J.; Culbertson, J. C.; Jernigan, G. G.; Hobart, K. D.; Kub, F. J.; Tadjer, M. J.; Tedesco, J. L.; Hite, J. K.; Mastro, M. A., Technique for the dry transfer of epitaxial graphene onto arbitrary substrates. *ACS nano* **2010,** *4* (2), 1108-1114.

61. Lin, Y. C.; Lu, C. C.; Yeh, C. H.; Jin, C.; Suenaga, K.; Chiu, P. W., Graphene annealing: how clean can it be. *Nano Letters* **2012,** *12* (1), 414-9.

62. Gong, C.; Floresca, H. C.; Hinojos, D.; McDonnell, S.; Qin, X.; Hao, Y.; Jandhyala, S.; Mordi, G.; Kim, J.; Colombo, L.; Ruoff, R. S.; Kim, M. J.; Cho, K.; Wallace, R. M.; Chabal, Y. J., Rapid selective etching of PMMA residues from transferred graphene by carbon dioxide. *The Journal of Physical Chemistry C* **2013,** *117* (44), 23000-23008.

63. Gurarslan, A.; Yu, Y.; Su, L.; Yu, Y.; Suarez, F.; Yao, S.; Zhu, Y.; Ozturk, M.; Zhang, Y.; Cao, L., Surface-energy-assisted perfect transfer of centimeter-scale monolayer and few-layer MoS_2 films onto arbitrary substrates. *ACS nano* **2014,** *8* (11), 11522-11528.

64. Li, H.; Wu, J.; Huang, X.; Yin, Z.; Liu, J.; Zhang, H., A universal, rapid method for clean transfer of nanostructures onto various substrates. *ACS nano* **2014,** *8* (7), 6563-6570.

65. Kumar, K.; Kim, Y.-S.; Yang, E.-H., The influence of thermal annealing to remove polymeric residue on the electronic doping and morphological

characteristics of graphene. *Carbon* **2013,** *65*, 35-45.

66. Suk, J. W.; Lee, W. H.; Lee, J.; Chou, H.; Piner, R. D.; Hao, Y.; Akinwande, D.; Ruoff, R. S., Enhancement of the electrical properties of graphene grown by chemical vapor deposition via controlling the effects of polymer residue. *Nano Letters* **2013,** *13* (4), 1462-1467.

67. Park, J.-H.; Jung, W.; Cho, D.; Seo, J.-T.; Moon, Y.; Woo, S.; Lee, C.; Park, C.-Y.; Ahn, J., Simple, green, and clean removal of a poly (methyl methacrylate) film on chemical vapor deposited graphene. *Applied Physics Letters* **2013,** *103* (17), 171609.

68. Peltekis, N.; Kumar, S.; McEvoy, N.; Lee, K.; Weidlich, A.; Duesberg, G. S., The effect of downstream plasma treatments on graphene surfaces. *Carbon* **2012,** *50* (2), 395-403.

69. Lim, Y.-D.; Lee, D.-Y.; Shen, T.-Z.; Ra, C.-H.; Choi, J.-Y.; Yoo, W. J., Si-compatible cleaning process for graphene using low-density inductively coupled plasma. *ACS nano* **2012,** *6* (5), 4410-4417.

70. Cheng, Z.; Zhou, Q.; Wang, C.; Li, Q.; Wang, C.; Fang, Y., Toward intrinsic graphene surfaces: a systematic study on thermal annealing and wet-chemical treatment of SiO2-supported graphene devices. *Nano Letters* **2011,** *11* (2), 767-771.

71. Xu, M.; Liang, T.; Shi, M.; Chen, H., Graphene-like two-dimensional materials. *Chemical Reviews* **2013,** *113* (5), 3766-98.

72. Kubota, Y.; Watanabe, K.; Tsuda, O.; Taniguchi, T., Deep ultraviolet light-emitting hexagonal boron nitride synthesized at atmospheric pressure. *Science* **2007,** *317* (5840), 932-934.

73. Dean, C. R.; Young, A. F.; Meric, I.; Lee, C.; Wang, L.; Sorgenfrei, S.; Watanabe, K.; Taniguchi, T.; Kim, P.; Shepard, K., Boron nitride substrates for high-quality graphene electronics. *Nature Nanotechnology* **2010,** *5* (10), 722-726.

74. Bao, J.; Jeppson, K.; Edwards, M.; Fu, Y.; Ye, L.; Lu, X.; Liu, J., Synthesis and applications of two-dimensional hexagonal boron nitride in electronics manufacturing. *Electronic Materials Letters* **2016,** *12* (1), 1-16.

75. Butler, S. Z.; Hollen, S. M.; Cao, L.; Cui, Y.; Gupta, J. A.; Gutiérrez, H. R.; Heinz, T. F.; Hong, S. S.; Huang, J.; Ismach, A. F., Progress, challenges, and opportunities in two-dimensional materials beyond graphene. *ACS nano* **2013,** *7* (4), 2898-2926.

76. Pacile, D.; Meyer, J.; Girit, C. O.; Zettl, A., The two-dimensional phase of boron nitride: few-atomic-layer sheets and suspended membranes. *Applied Physics Letters* **2008,** *92* (13), 133107.

77. Coleman, J. N.; Lotya, M.; O'Neill, A.; Bergin, S. D.; King, P. J.; Khan, U.; Young, K.; Gaucher, A.; De, S.; Smith, R. J., Two-dimensional nanosheets produced by liquid exfoliation of layered materials. *Science* **2011,** *331* (6017), 568-571.

78. Wen, Y.; Shang, X.; Dong, J.; Xu, K.; He, J.; Jiang, C., Ultraclean and large-area monolayer hexagonal boron nitride on Cu foil using chemical vapor deposition. *Nanotechnology* **2015,** *26* (27), 275601.

79. Ismach, A.; Chou, H.; Ferrer, D. A.; Wu, Y.; McDonnell, S.; Floresca, H. C.; Covacevich, A.; Pope, C.; Piner, R.; Kim, M. J., Toward the controlled synthesis of hexagonal boron nitride films. *ACS nano* **2012,** *6* (7), 6378-6385.

80. Lee, K. H.; Shin, H.-J.; Lee, J.; Lee, I.-y.; Kim, G.-H.; Choi, J.-Y.; Kim, S.-W., Large-scale synthesis of high-quality hexagonal boron nitride nanosheets for large-area graphene electronics. *Nano Letters* **2012,** *12* (2), 714-718.

81. Sutter, P.; Lahiri, J.; Albrecht, P.; Sutter, E., Chemical vapor deposition and etching of high-quality monolayer hexagonal boron nitride films. *ACS nano* **2011,** *5* (9), 7303-7309.

82. Moore, A. L.; Shi, L., Emerging challenges and materials for thermal management of electronics. *Materials Today* **2014,** *17* (4), 163-174.

83. Adivarahan, V.; Yang, J.; Koudymov, A.; Simin, G.; Khan, M. A., Stable CW operation of field-plated GaN-AlGaN MOSHFETs at 19 W/mm. *Electron Device Letters, IEEE* **2005,** *26* (8), 535-537.

84. Chini, A.; Buttari, D.; Coffie, R.; Heikman, S.; Keller, S.; Mishra, U., 12W/mm power density AlGaN/GaN HEMTs on sapphire substrate. *Electronics Letters* **2004,** *40* (1), 1.

85. Shin, M.; Trew, R., GaN MESFETs for high-power and high-temperature microwave applications. *Electronics Letters* **1995,** *31* (6), 498-500.

86. Daumiller, I.; Kirchner, C.; Kamp, M.; Ebeling, K.; Kohn, E., Evaluation of the temperature stability of AlGaN/GaN heterostructure FETs. *Electron Device Letters, IEEE* **1999,** *20* (9), 448-450.

87. Hamann, H. F.; Weger, A.; Lacey, J. A.; Hu, Z.; Bose, P.; Cohen, E.; Wakil, J., Hotspot-limited microprocessors: Direct temperature and power distribution measurements. *IEEE Journal of Solid-State Circuits* **2007,** *42* (1), 56-65.

88. Turin, V. O.; Balandin, A. A., Electrothermal simulation of the self-heating effects in GaN-based field-effect transistors. *Journal of Applied Physics* **2006,** *100* (5), 054501.

89. Wang, X.-D.; Hu, W.-D.; Chen, X.-S.; Lu, W., The Study of Self-Heating and Hot-Electron Effects for AlGaN/GaN Double-Channel HEMTs. *IEEE Transactions on Electron Devices* **2012,** *59* (5), 1393-1401.

90. Trew, R. J.; Green, D. S.; Shealy, J. B., AlGaN/GaN HFET reliability. *Microwave Magazine, IEEE* **2009,** *10* (4), 116-127.

91. Won, Y.; Cho, J.; Agonafer, D.; Asheghi, M.; Goodson, K. E., Fundamental cooling limits for high power density gallium nitride electronics. *Components, Packaging and Manufacturing Technology, IEEE Transactions on* **2015,** *5* (6), 737-744.

92. Yan, Z.; Liu, G.; Khan, J. M.; Balandin, A. A., Graphene quilts for thermal management of high-power GaN transistors. *Nature Communications* **2012,** *3*,

827.

93. Gao, Z.; Zhang, Y.; Fu, Y.; Yuen, M. M.; Liu, J., Thermal chemical vapor deposition grown graphene heat spreader for thermal management of hot spots. *Carbon* **2013,** *61*, 342-348.

94. Hwang, E.; Adam, S.; Sarma, S. D., Carrier transport in two-dimensional graphene layers. *Physical Review Letters* **2007,** *98* (18), 186806.

95. Lindsay, L.; Broido, D. A., Enhanced thermal conductivity and isotope effect in single-layer hexagonal boron nitride. *Physical Review B* **2011,** *84* (15).

96. Hugosson, H. W.; Eriksson, O.; Nordström, L.; Jansson, U.; Fast, L.; Delin, A.; Wills, J. M.; Johansson, B., Theory of phase stabilities and bonding mechanisms in stoichiometric and substoichiometric molybdenum carbide. *Journal of Applied Physics* **1999,** *86* (7), 3758-3767.

97. Xu, C.; Wang, L.; Liu, Z.; Chen, L.; Guo, J.; Kang, N.; Ma, X. L.; Cheng, H. M.; Ren, W., Large-area high-quality 2D ultrathin Mo_2C superconducting crystals. *Nature Materials* **2015,** *14* (11), 1135-1141.

98. Hugosson, H. W.; Eriksson, O.; Jansson, U.; Johansson, B., Phase stabilities and homogeneity ranges in4d-transition-metal carbides: A theoretical study. *Physical Review B* **2001,** *63* (13).

99. Kavitha, M.; Priyanga, G. S.; Rajeswarapalanichamy, R.; Iyakutti, K., Structural stability, electronic, mechanical and superconducting properties of CrC and MoC. *Materials Chemistry and Physics* **2016,** *169*, 71-81.

100. Barsoum, M. W.; El-Raghy, T., The MAX Phases: Unique New Carbide and Nitride Materials Ternary ceramics turn out to be surprisingly soft and machinable, yet also heat-tolerant, strong and lightweight. *American Scientist* **2001,** *89* (4), 334-343.

101. Wang, X.; Feng, H.; Wu, Y.; Jiao, L., Controlled synthesis of highly crystalline MoS2 flakes by chemical vapor deposition. *Journal of the American Chemical Society* **2013,** *135* (14), 5304-7.

102. Kikkawa, T.; Makiyama, K.; Ohki, T.; Kanamura, M.; Imanishi, K.; Hara, N.; Joshin, K., High performance and high reliability AlGaN/GaN HEMTs. *Physica Status Solidi (a)* **2009,** *206* (6), 1135-1144.

103. Liu, K. K.; Zhang, W.; Lee, Y. H.; Lin, Y. C.; Chang, M. T.; Su, C. Y.; Chang, C. S.; Li, H.; Shi, Y.; Zhang, H.; Lai, C. S.; Li, L. J., Growth of large-area and highly crystalline MoS_2 thin layers on insulating substrates. *Nano Letters* **2012,** *12* (3), 1538-44.

104. Li, X.-L.; Liu, J.-F.; Li, Y.-D., Low-temperature synthesis of large-scale single-crystal molybdenum trioxide (MoO_3) nanobelts. *Applied Physics Letters* **2002,** *81* (25), 4832-4834.

105. Wang, S.; Rong, Y.; Fan, Y.; Pacios, M.; Bhaskaran, H.; He, K.; Warner, J. H., Shape Evolution of Monolayer MoS_2 Crystals Grown by Chemical Vapor Deposition. *Chemistry of Materials* **2014,** *26* (22), 6371-6379.

106. Shi, J.; Ma, D.; Han, G.-F.; Zhang, Y.; Ji, Q.; Gao, T.; Sun, J.; Song, X.; Li, C.; Zhang, Y., Controllable Growth and Transfer of Monolayer MoS_2 on Au Foils and Its Potential Application in Hydrogen Evolution Reaction. *ACS nano* **2014,** *8* (10), 10196-10204.

107. Zhang, J.; Yu, H.; Chen, W.; Tian, X.; Liu, D.; Cheng, M.; Xie, G.; Yang, W.; Yang, R.; Bai, X., Scalable growth of high-quality polycrystalline MoS_2 monolayers on SiO_2 with tunable grain sizes. *ACS nano* **2014,** *8* (6), 6024-6030.

108. Pierson, H. O., *Handbook of chemical vapor deposition: principles, technology and applications*. William Andrew: 1999.

109. Gao, L.; Ren, W.; Xu, H.; Jin, L.; Wang, Z.; Ma, T.; Ma, L. P.; Zhang, Z.; Fu, Q.; Peng, L. M.; Bao, X.; Cheng, H. M., Repeated growth and bubbling transfer of graphene with millimetre-size single-crystal grains using platinum. *Nature Communications* **2012,** *3*, 699.

110. Dobkin, D. M.; Zuraw, M. K., *Principles of chemical vapor deposition*.

Springer Science & Business Media: Netherlands, 2003; p 34-38.

111. Lee, C.; Yan, H.; Brus, L. E.; Heinz, T. F.; Hone, J.; Ryu, S., Anomalous lattice vibrations of single-and few-layer MoS_2. *ACS nano* **2010,** *4* (5), 2695-2700.

112. Hu, W.; Antoine, D.; Yu, X., Optically transparent poly(methyl methacrylate) composite reinforced by polyacylonitrile hollow nanofibers. *Journal of Composite Materials* **2013,** *48* (24), 3019-3024.

113. Rice, C.; Young, R.; Zan, R.; Bangert, U.; Wolverson, D.; Georgiou, T.; Jalil, R.; Novoselov, K., Raman-scattering measurements and first-principles calculations of strain-induced phonon shifts in monolayer MoS_2. *Physical Review B* **2013,** *87* (8).

114. Castellanos-Gomez, A.; Roldan, R.; Cappelluti, E.; Buscema, M.; Guinea, F.; van der Zant, H. S.; Steele, G. A., Local strain engineering in atomically thin MoS_2. *Nano Letters* **2013,** *13* (11), 5361-6.

115. Jiang, H.; Khang, D. Y.; Song, J.; Sun, Y.; Huang, Y.; Rogers, J. A., Finite deformation mechanics in buckled thin films on compliant supports. *Proceedings of the National Academy of Sciences of the United States of America* **2007,** *104* (40), 15607-12.

116. Fei, L.-f.; Sun, T.-y.; Lu, W.; An, X.-q.; Hu, Z.-f.; Jimmy, C. Y.; Zheng, R.-k.; Li, X.-m.; Chan, H. L.; Wang, Y., Direct observation of carbon nanostructure growth at liquid–solid interfaces. *Chemical Communications* **2014,** *50* (7), 826-828.

117. Ramachandramoorthy, R.; Bernal, R.; Espinosa, H. D., Pushing the envelope of in situ transmission electron microscopy. *ACS nano* **2015,** *9* (5), 4675-4685.

118. Nielsen, M. H.; Aloni, S.; De Yoreo, J. J., In situ TEM imaging of $CaCO_3$ nucleation reveals coexistence of direct and indirect pathways. *Science* **2014,** *345* (6201), 1158-1162.

119. Liao, H.-G.; Cui, L.; Whitelam, S.; Zheng, H., Real-time imaging of Pt_3Fe nanorod growth in solution. *Science* **2012,** *336* (6084), 1011-1014.

120. Boston, R.; Schnepp, Z.; Nemoto, Y.; Sakka, Y.; Hall, S. R., In situ TEM observation of a microcrucible mechanism of nanowire growth. *Science* **2014,** *344* (6184), 623-626.

121. Kresse, G.; Furthmüller, J., Efficiency of ab-initio total energy calculations for metals and semiconductors using a plane-wave basis set. *Computational Materials Science* **1996,** *6* (1), 15-50.

122. Kresse, G.; Furthmüller, J., Efficient iterative schemes for ab initio total-energy calculations using a plane-wave basis set. *Physical Review B* **1996,** *54* (16), 11169.

123. Blöchl, P. E., Projector augmented-wave method. *Physical Review B* **1994,** *50* (24), 17953.

124. Kresse, G.; Joubert, D., From ultrasoft pseudopotentials to the projector augmented-wave method. *Physical Review B* **1999,** *59* (3), 1758.

125. Perdew, J. P.; Burke, K.; Ernzerhof, M., Generalized gradient approximation made simple. *Physical Review Letters* **1996,** *77* (18), 3865.

126. Reuter, K.; Scheffler, M., Composition, structure, and stability of RuO_2 (110) as a function of oxygen pressure. *Physical Review B* **2001,** *65* (3), 035406.

127. Brito, J. L.; Ilija, M.; Hernández, P., Thermal and reductive decomposition of ammonium thiomolybdates. *Thermochimica Acta* **1995,** *256* (2), 325-338.

128. Verble, J.; Wietling, T.; Reed, P., Rigid-layer lattice vibrations and van der waals bonding in hexagonal MoS_2. *Solid State Communications* **1972,** *11* (8), 941-944.

129. Kong, D.; Wang, H.; Cha, J. J.; Pasta, M.; Koski, K. J.; Yao, J.; Cui, Y., Synthesis of MoS_2 and $MoSe_2$ films with vertically aligned layers. *Nano Letters* **2013,** *13* (3), 1341-1347.

130. Jung, Y.; Shen, J.; Liu, Y.; Woods, J. M.; Sun, Y.; Cha, J. J., Metal seed layer thickness-induced transition from vertical to horizontal growth of MoS_2 and WS_2. *Nano Letters* **2014,** *14* (12), 6842-6849.

131. Hansen, L. P.; Johnson, E.; Brorson, M.; Helveg, S., Growth mechanism for single-and multi-layer MoS_2 nanocrystals. *The Journal of Physical Chemistry C* **2014,** *118* (39), 22768-22773.

132. Stockmann, R.; Zandbergen, H.; Van Langeveld, A.; Moulijn, J., Investigation of MoS_2 on γ-Al_2O_3 by HREM with atomic resolution. *Journal of Molecular Catalysis A: Chemical* **1995,** *102* (3), 147-161.

133. Li, D.; Nielsen, M. H.; Lee, J. R.; Frandsen, C.; Banfield, J. F.; De Yoreo, J. J., Direction-specific interactions control crystal growth by oriented attachment. *Science* **2012,** *336* (6084), 1014-1018.

134. Yin, Y.; Alivisatos, A. P., Colloidal nanocrystal synthesis and the organic–inorganic interface. *Nature* **2005,** *437* (7059), 664-670.

135. Shi, Y.; Zhou, W.; Lu, A.-Y.; Fang, W.; Lee, Y.-H.; Hsu, A. L.; Kim, S. M.; Kim, K. K.; Yang, H. Y.; Li, L.-J., van der Waals epitaxy of MoS_2 layers using graphene as growth templates. *Nano Letters* **2012,** *12* (6), 2784-2791.

136. Preiss, H.; Meyer, B.; Olschewski, C., Preparation of molybdenum and tungsten carbides from solution derived precursors. *Journal of Materials Science* **1998,** *33* (3), 713-722.

137. Mishra, U. K.; Parikh, P.; Wu, Y.-F., AlGaN/GaN HEMTs-an overview of device operation and applications. *Proceedings-IEEE* **2002,** *90* (6), 1022-1031.

138. Maekawa, A.; Yamamoto, T.; Mitani, E.; Sano, S., A 500W push-pull AlGaN/GaN HEMT amplifier for L-band high power application, *2006 IEEE MTT-S International Microwave Symposium Digest*, pp 722-725.

139. Sun, J.; Fatima, H.; Koudymov, A.; Chitnis, A.; Hu, X.; Wang, H.; Zhang, J.; Simin, G.; Yang, J.; Khan, M. A., Thermal management of

AlGaN-GaN HFETs on sapphire using flip-chip bonding with epoxy underfill. *Electron Device Letters, IEEE* **2003,** *24* (6), 375-377.

140. Ghosh, S.; Calizo, I.; Teweldebrhan, D.; Pokatilov, E.; Nika, D.; Balandin, A.; Bao, W.; Miao, F.; Lau, C. N., Extremely high thermal conductivity of graphene: Prospects for thermal management applications in nanoelectronic circuits. *Applied Physics Letters* **2008,** *92* (15), 151911.

141. Ghosh, S.; Bao, W.; Nika, D. L.; Subrina, S.; Pokatilov, E. P.; Lau, C. N.; Balandin, A. A., Dimensional crossover of thermal transport in few-layer graphene. *Nature Materials* **2010,** *9* (7), 555-558.

142. Tan, Y.-W.; Zhang, Y.; Bolotin, K.; Zhao, Y.; Adam, S.; Hwang, E.; Sarma, S. D.; Stormer, H.; Kim, P., Measurement of scattering rate and minimum conductivity in graphene. *Physical Review Letters* **2007,** *99* (24), 246803.

143. Lin, Y.; Connell, J. W., Advances in 2D boron nitride nanostructures: nanosheets, nanoribbons, nanomeshes, and hybrids with graphene. *Nanoscale* **2012,** *4* (22), 6908-6939.

144. Pakdel, A.; Zhi, C.; Bando, Y.; Golberg, D., Low-dimensional boron nitride nanomaterials. *Materials Today* **2012,** *15* (6), 256-265.

145. Jo, I.; Pettes, M. T.; Kim, J.; Watanabe, K.; Taniguchi, T.; Yao, Z.; Shi, L., Thermal conductivity and phonon transport in suspended few-layer hexagonal boron nitride. *Nano Letters* **2013,** *13* (2), 550-554.

146. Lin, Z.; Liu, Y.; Raghavan, S.; Moon, K.-s.; Sitaraman, S. K.; Wong, C.-p., Magnetic alignment of hexagonal boron nitride platelets in polymer matrix: toward high performance anisotropic polymer composites for electronic encapsulation. *ACS Applied Materials & Interfaces* **2013,** *5* (15), 7633-7640.

147. Shi, Y.; Hamsen, C.; Jia, X.; Kim, K. K.; Reina, A.; Hofmann, M.; Hsu, A. L.; Zhang, K.; Li, H.; Juang, Z.-Y., Synthesis of few-layer hexagonal boron nitride thin film by chemical vapor deposition. *Nano Letters* **2010,** *10* (10),

4134-4139.

148. Song, L.; Ci, L.; Lu, H.; Sorokin, P. B.; Jin, C.; Ni, J.; Kvashnin, A. G.; Kvashnin, D. G.; Lou, J.; Yakobson, B. I., Large scale growth and characterization of atomic hexagonal boron nitride layers. *Nano Letters* **2010,** *10* (8), 3209-3215.

149. Chatterjee, S.; Luo, Z.; Acerce, M.; Yates, D. M.; Johnson, A. C.; Sneddon, L. G., Chemical vapor deposition of boron nitride nanosheets on metallic substrates via decaborane/ammonia reactions. *Chemistry of Materials* **2011,** *23* (20), 4414-4416.

150. Liu, J.; Wang, H.; Ma, W.; Zhang, X.; Song, Y., Simultaneous measurement of thermal conductivity and thermal contact resistance of individual carbon fibers using Raman spectroscopy. *Review of Scientific Instruments* **2013,** *84* (4), 044901.

151. Chen, S.; Wu, Q.; Mishra, C.; Kang, J.; Zhang, H.; Cho, K.; Cai, W.; Balandin, A. A.; Ruoff, R. S., Thermal conductivity of isotopically modified graphene. *Nature Materials* **2012,** *11* (3), 203-207.

152. Sahoo, S.; Gaur, A. P.; Ahmadi, M.; Guinel, M. J.-F.; Katiyar, R. S., Temperature-dependent Raman studies and thermal conductivity of few-layer MoS2. *The Journal of Physical Chemistry C* **2013,** *117* (17), 9042-9047.

153. Yue, Y.; Zhang, J.; Wang, X., Micro/nanoscale spatial resolution temperature probing for the interfacial thermal characterization of epitaxial graphene on 4H-SiC. *Small* **2011,** *7* (23), 3324-3333.

154. Hart, T.; Aggarwal, R.; Lax, B., Temperature dependence of Raman scattering in silicon. *Physical Review B* **1970,** *1* (2), 638.

155. Menéndez, J.; Cardona, M., Temperature dependence of the first-order Raman scattering by phonons in Si, Ge, and α−Sn: Anharmonic effects. *Physical Review B* **1984,** *29* (4), 2051.

156. Liu, M. S.; Bursill, L. A.; Prawer, S.; Nugent, K.; Tong, Y.; Zhang, G.,

Temperature dependence of Raman scattering in single crystal GaN films. *Applied Physics Letters* **1999,** *74* (21), 3125.

157. Zhou, H.; Zhu, J.; Liu, Z.; Yan, Z.; Fan, X.; Lin, J.; Wang, G.; Yan, Q.; Yu, T.; Ajayan, P. M.; Tour, J. M., High thermal conductivity of suspended few-layer hexagonal boron nitride sheets. *Nano Research* **2014,** *7* (8), 1232-1240.

158. Cai, W.; Moore, A. L.; Zhu, Y.; Li, X.; Chen, S.; Shi, L.; Ruoff, R. S., Thermal transport in suspended and supported monolayer graphene grown by chemical vapor deposition. *Nano Letters* **2010,** *10* (5), 1645-51.